INVESTIGATION OF THE EFFECTS OF EXTREME STRESS GRADIENTS ON FATIGUE BEHAVIOR OF NICKEL MICROBEAMS

A Dissertation
Presented to
The Academic Faculty

by

Farzad Sadeghi-Tohidi

In Partial Fulfillment
of the Requirements for the Degree
Doctor of Philosophy in the
George W. Woodruff School of Mechanical Engineering

Georgia Institute of Technology

May 2016

INVESTIGATION OF THE EFFECTS OF EXTREME STRESS GRADIENTS ON FATIGUE BEHAVIOR OF NICKEL MICROBEAMS

Approved by:

Dr. Olivier N. Pierron, Advisor
George W. Woodruff School of Mechanical Engineering
Georgia Institute of Technology

Dr. Samuel Graham
George W. Woodruff School of Mechanical Engineering
Georgia Institute of Technology

Dr. Hamid Garmestani
School of Material Science and Engineering
Georgia Institute of Technology

Dr. Richard W. Neu
George W. Woodruff School of Mechanical Engineering
Georgia Institute of Technology

Dr. Antonia Antoniou
George W. Woodruff School of Mechanical Engineering
Georgia Institute of Technology

Date Approved: December 14th, 2015

ACKNOWLEDGEMENTS

The acknowledgement is the most difficult thing to write considering the number of people helped me throughout the course of my doctoral study at Georgia Institute of Technology. I would like to take the opportunity to thank them here and I want to apologize to everyone whom I might have forgotten to mention by name. First of all, I would to thank my advisors, Dr. Olivier Pierron for his guidance and support during the past four years. Without his expertise and knowledge this work could not have been started, continued, and finished successfully. My deepest gratitude goes to graduate committee members: Dr. Hamid Garmestani, Dr. Samuel Graham, Dr. Richard W. Neu, and Dr. Antonia Antoniou for their invaluable help, recommendations, and feedback throughout my PhD proposal and defense process.

Furthermore I would like to ta thank the friendly support of all the George W. Woodruff School's faculty/Staff since August 2010 when I joined Georgia Tech. Among them are Dr. G. Paul Neitzel, Dr. Jeffrey Donnell, Dr. Wayne Whiteman, Ms. Glenda Johnson, Mr. Eric Woods, Mr. Todd Walters, and Ms. Dana Foster who were always friendly and helpful, no matter when or for what I approached them about. Also I would like to thank my former and current group mates, Dr. Eva Baumert, Ehsan Hosseinian, Saurabh Gupta, Kyungjin Kim. Special thanks are extended to Eva for her help to train me with fatigue test routines.

Last but not the least, my special thanks goes to my family and friends for the moral support and understanding without which this work would not have been possible. Their unwavering support always helped me through challenging situations. I am

wholeheartedly thankful to my father, Freidoun, my mother, Shahnaz, my brother, Khosro, and my sister Shiva for their unconditional love and kindly support. I have no doubt that I would not be in this position without their encouragement all through of my life.

Table of contents

LIST OF TABLES

LIST OF FIGURES

LIST OF SYMBOLS AND ABBREVIATIONS

EDX	Energy-Dispersive X-ray spectroscopy.
FEM	Finite Element Modeling.
FIB	Focused Ion Beam tool.
HCF	High Cycle Fatigue.
LCF	Low Cycle Fatigue.
LIGA	Acronym for German *Lithographie, Galvanoformung, Abformung;* in English lithography, electroplating, molding.
MEMS	MicroElectroMechanical Systems.
RH	Relative Humidity.
SEM	Scanning Electron Microscopy.
TEM	Transmission Electron Microscopy.
VHCF	Very High Cycle Fatigue.
W_{max}	Maximum with of beam.
W_{min}	Minimum with of beam.
Δf_0	Decrease in resonance frequency.
$\Delta f_{0;max}$	Maximum decrease in resonance frequency.
ΔK	Stress intensity range.
ΔK_{th}	Threshold stress intensity factor range.
ε_a	Strain amplitude at the notch root.
σ_a	Stress amplitude.
σ_{UTS}	Ultimate tensile stress.
θ_0	In-plane angle of rotation of the resonator at resonance.

θ	In-plane angle of rotation of the resonator.
ε	Electric permittivity of air, 8.855×10^{-12} Fm^{-1}.
η	Normalized stress gradient.
E	Elastic modulus of nickel.
k_f	Fatigue notch factor.
k_t	Elastic concentration factor.
J_θ	In-plane mass moment of inertia of the resonator.
M_o	Amplitude of applied moment.
N_f	Life or number of cycles to failure.
Q	Quality factor.
q	The notch sensitivity index.
R	Stress ratio: $R = \sigma_{min}/\sigma_{max}$
S	The nominal stress.
V_{in}	Amplitude of the input electric signal.
V_{out}	Amplitude of the output electrical signal at resonance.
b	Damping coefficient, also Basquin coefficient.
c	Coffin-Manson coefficient.
f_0	Frequency at resonance, short resonance frequency.
$f_{0;initial}$	Initial resonance frequency (f_0 at the beginning of test).
h	Film thickness.
k_θ	Resonator torsional stiffness.
$r_{i,j}$	Radius of the inner finger of the j^{th} capacitor.
$r_{o,j}$	Radius of the outer finger of the j^{th} capacitor.

SUMMARY

Thin films technologies continue to play a key role in the development of stretchable electronics, flexible displays, and a wide range of microelectromechanical systems (MEMS) applications. Movable components can be exposed to cyclic loading in these applications, which can result in fatigue failure. Hence the investigation of fatigue degradation mechanisms of thin films is required to address some of these reliability concerns. Particularly, extreme stress gradients can occur for notched or unnotched micro-components in bending mode. In this research, a microresonator-based technique is presented to investigate the effect of extreme stress gradient (normalized stress gradients of 17 and 36%.μm^{-1}) on the fatigue properties of 20-μm-thick electroplated Ni microbeams in both mild (30°C, 50% RH) and harsh (80°C, 90% RH) environments. The technique relies on the measured evolution of the resonance frequency throughout the fatigue test and finite element models to calculate a fatigue life corresponding to the nucleation and growth of a ~2-micrometer-long crack. In addition, the growth rates of these microstructurally small cracks were estimated also based on the measured resonance frequency evolution. The results of this dissertation highlight that the fatigue life of nickel microbeams under extreme stress gradients is dominated by the ultraslow growth of microstructurally small cracks, which is a strong function of the applied stress gradient. The calculated initial crack propagation rates are ~10 times larger for η = 17%.μm^{-1} compared to η = 36%.μm^{-1} for σ_a between 400 and 450 MPa. The discrepancy is even larger with increasing crack size from 0 to 2 μm. For η = 36%.μm^{-1}, the initial rates decrease with

increasing *a*, whereas for η = 17%.μm^{-1}, the crack propagation rates do not decrease with increasing *a*. These effects result in significant difference in fatigue lives by orders of magnitude: at σ_a ~ 450 MPa, the fatigue life is 1000 times larger for η = 17%.μm^{-1} ($N_f = 10^5$ cycles) than for η = 36%.μm^{-1} ($N_f = 10^8$ cycles). The stress-life fatigue curves exhibit low Basquin exponents, *b*, varying from -0.039 to -0.023 for stress gradients increasing from 17% to 36%.μm^{-1}. Consequently, larger endurance limits (50% of the tensile strength) are associated with the steeper stress gradients. Little differences were observed in the fatigue response (stress-life fatigue curves, crack propagation rates) between the two investigated environments (30°C, 50% RH vs 80°C, 90% RH) with only slightly shorter fatigue lives in the harsher environment. However, scanning electron microscope images of the fatigued specimens and energy dispersive spectroscopy results from the sidewalls and fracture surfaces of the fatigued microbeams highlight an environmental component in the fatigue process, in the form of oxide formation at the location of the extrusions and along the crack flanks of these microstructurally small cracks. The results of this research bring significant insight regarding the reliability concerns of metallic microbeams.

CHAPTER 1: BACKGROUND AND MOTIVATION

In this research, we will address the effect of extreme stress gradients on fatigue behavior of nickel microbeams. Extreme stress gradients cannot be obtained at the bulk scale. However, the presence of extreme stress gradients in micro-scale components could result in significantly different fatigue behavior. The background review in this chapter begins by introducing the notch effect and microstructurally small cracks behavior in the absence of stress gradient and discussing necessity of further investigations to predict the corresponding behavior for micro-components under extreme stress gradients. Then, we will continue by introducing the fatigue behavior of Ni microbeam in the absence of an applied stress gradient in terms of S-N curve and microstructurally small cracks (MSC) propagation rates. Following that, the significant importance of stress gradient effect on fatigue life of micro-components especially under bending loading conditions has been highlighted. At the end of this chapter, the motivation of this research is discussed.

1.1 Notch Effects on Fatigue Behavior

For macro scale specimens, microcracks form at stress concentration sites and lead to fatigue damage and failure. This fatigue mechanism is facilitated by the presence of any geometric discontinuities, such as holes or grooves. These geometric discontinuities are termed ‘notches’ for brevity, and they act to raise stress. The fatigue limit, in term of notch root stress, of a notched structure is typically larger than that of a smooth specimen [7, 11-16]. The physical explanation is related to the stress gradients that are present ahead of a notch and the fact that fatigue occurs within a process zone

of a finite volume that is subjected to a lower average stress than the maximum stress at the notch root [17]. The sharper the notch, the larger the notch root stress fatigue limit due to the larger stress gradients.

Abrupt decreases in fatigue resistance due to the notch effect highlight the need to understand the fatigue mechanisms of notched components [10-12]. It is well-known that the stress amplitude in the vicinity of stress concentration sites has a key role in fatigue cracks' nucleation and propagation [5, 13-18]. The elastic concentration factor k_t has been employed to define the ratio of σ_{max}, the maximum local stress ahead of the notch tip, to *S*, the nominal stress. However, experimental fatigue results show that notches produce less effect on fatigue life than is predicted by k_t. To address this issue, the fatigue notch factor, k_f , has been employed to define the factor by which fatigue life is reduced as a result of notch presence and stress concentration sites. The degree of discrepancy between k_t and k_f has been measured by the notch sensitivity index (q) as follow:

$$q = \frac{k_f - 1}{k_t - 1} \tag{1}$$

Which varies from zero to unity, corresponding to no notch effect and full notch effect, respectively. In other words for the maximum notch effect, $k_f = k_t$; consequently q = 1. From the experimental point of view, this maximum notch effect for the bulk-scale fatigue tests happens for highly ductile material and sharp notches. Experimental measurements illustrate that a stress concentration with k_t above a certain value could result in a nonpropagating fatigue crack [1, 2, 10]. Indeed, one additional reason for the increased fatigue limit is the formation of non-propagating cracks – cracks nucleating at

the notch root but unable to propagate due to the decreasing stress intensity factor range with increasing crack size which occurs for sharp enough notches (for example, less than 2.5 mm for circular notches) [14, 18]. Non-propagating, small cracks (~1 mm at most) may develop ahead of sharp notches (large stress gradients at most ~1-2%.μm^{-1}, i.e. significantly smaller than the extreme stress gradients in our study) [17] as a result of decreasing driving force for crack propagation due to the stress gradient [14, 16, 18]. As presented in Figure 1.1, nonpropagating fatigue cracks could increase the fatigue limit for the bulk-scale fatigue tests to a level beyond that predicted by k_t and k_f effects. It is expected that effect of nonpropagating cracks will be further exacerbated for the fatigue life of micro-components. This is because micro-notched components under MEMS-relevant loading conditions, or even unnotched micro-component under bending loading, experience extremely large stress gradients that cannot be obtained at the bulk scale for the similar values of k_t. In other words, a given value of k_t, applied for bulk and for micro-scale components, could result in significantly different stress gradients. The normalized stress gradient is related to geometry by the stress concentration factor (η) as:

$$\eta = \frac{1}{\sigma_{max}}\left(\frac{d\sigma}{dx}\right) \tag{2}$$

where, σ_{max} is the maximum stress at the notch root and $\frac{d\sigma}{dx}$ is the stress variation within distance x from the notch root [19].

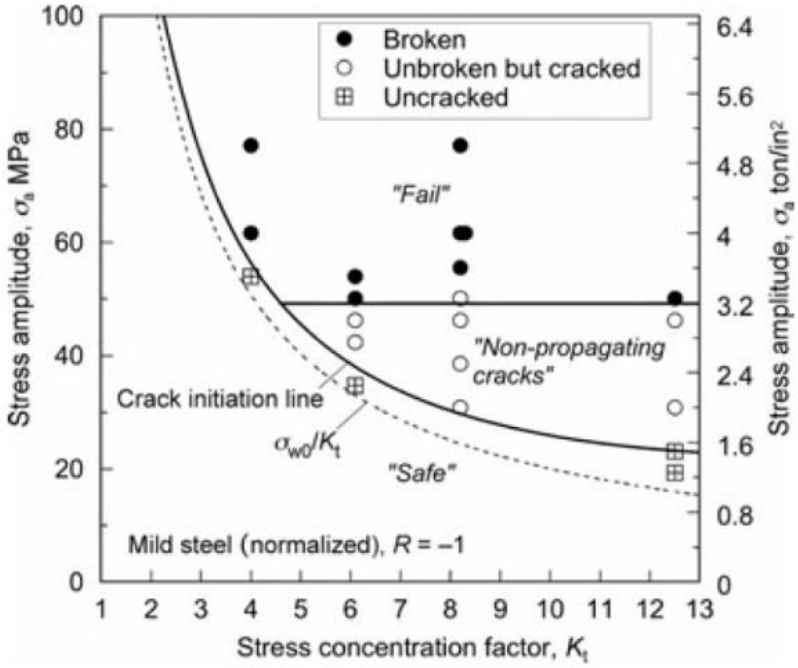

Figure 1.1: Effect of nonpropagating cracks on increasing the fatigue limit for tests performed at bulk scale [1, 2].

The notch effect has been reasonably understood for macro scale. For an example in a comprehensive study, Lukas and Klesnil developed a model to predict fatigue limits in notched bodies that relies on the stress intensity factor formulas ahead of notches (in that case, assuming that linear elastic fracture mechanics is valid) and on the fact that fatigue failure occurs if a crack can grow large enough to reach a critical size that corresponds to the threshold stress intensity factor range, ΔK_{th} (for long cracks) [5]. The results showed that the predicted fatigue limit is a strong function of the critical crack size (ranging from 10 to 200 μm) and of the normalized stress gradients, η (up to 1% decrease in stress per micrometer, i.e. $\eta = 1\%.\mu m^{-1}$); see Figure 1.2. Other models rely on elastic-plastic fracture mechanics to account for the notch plasticity [18].

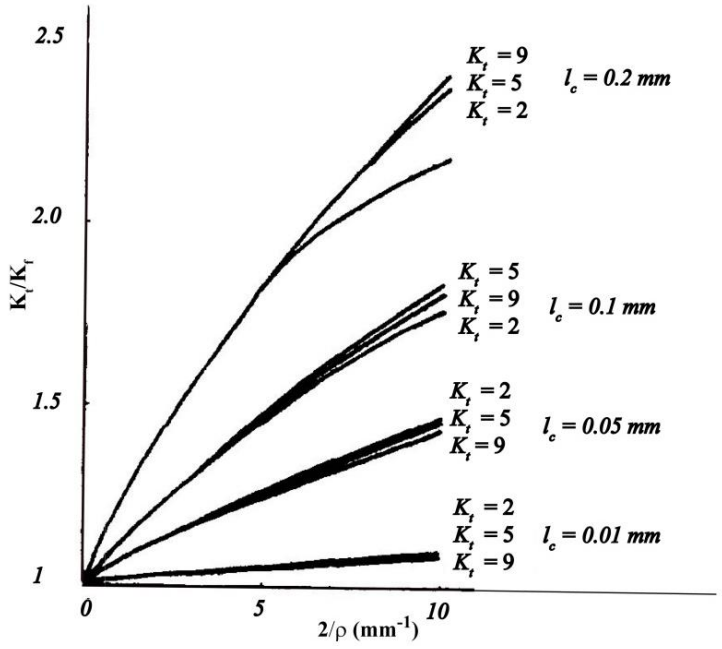

Figure 1.2: Influence of stress gradients on the k_t/k_f ratio [5].

It is important to realize that these concepts cannot be applied in the case of microbeams (whether or not they are notched) subjected to cyclic bending for two main reasons. First, the normalized stress gradients η are at least one order of magnitude larger (in our case, 36% decrease in stress per micrometer over the first two micrometers, i.e. $\eta = 36\%.\mu m^{-1}$) while the maximum values in notched bulk components do not exceed 1-2%.μm^{-1} [17]. Therefore this range of stress gradients has not been yet explored. Second, the fatigue cracks propagating from the edges of the microbeams toward the neutral axis are microstructurally small (their size is commensurate with the grain size). Therefore the concepts associated with linear elastic as well as elastic-plastic fracture mechanics are not valid, and the mechanical threshold associated with fatigue of long cracks (ΔK_{th}) must be replaced with microstructural thresholds (physical barriers such as grain boundaries).

1.2 Fatigue Growth of Small Cracks

A crack's size determines its classification as a microstructurally, mechanically, physically, or chemically small crack [18]. Here, a small crack is comparable in size to the grain size of the material, and it is called a microstructurally small crack. Such cracks present anomalous fatigue behavior that cannot be interpreted by linear elastic fracture mechanism (LEFM). Figure 1.3 shows the growth rate behavior of microstructurally and mechanically small cracks [8]. Small cracks exhibit an anomalous behavior in the crack propagation rate curve even in the absence of applied stress gradient [20, 21]. This behavior is characterized by much faster crack propagation rates (compared to long (several mm) cracks) that decrease with increasing crack size [22-27]. This discrepancy between the microstructurally and the mechanically small crack growth rates could arise as a result of differences in the crack growth characteristics, crack closure, and crack path tortuosity of short and long cracks [1, 10, 20, 28-31]. The difference between the intrinsic threshold of short and long crack has been investigated [32-34]. As presented in this figure by increasing crack length, the growth rate of microstructurally small cracks initially decreases to a certain level; at which point it increases until it merges with mechanically small crack growth rates. The retardation in crack growth occurs when the corresponding crack tip reaches a grain boundary. This figure illustrates that the LEFM approach dangerously overestimates the fatigue life of components with initial short cracks, and demonstrates that experiments developed for long cracks could not be used to predict the fatigue life of components with short cracks. It is also important that Figure 1.3 presents the fatigue behavior of a short crack for a specimen which is not under a stress gradient.

Recently, promising approaches have been developed to model the propagation of microstructurally small cracks in bulk materials [35-37]. However, the aforementioned issue of microstructurally small cracks propagating under extreme stress gradients, highly relevant for micro-components, has yet to be addressed, largely due to the lack of suitable experimental characterization techniques. The presence of an extreme stress gradient could result in a different short crack propagation pattern, which is the main topic of this thesis. In this dissertation, we present a micro-scale technique dedicated to the fatigue characterization of metallic micro-beams, including the microstructurally small crack propagation behavior.

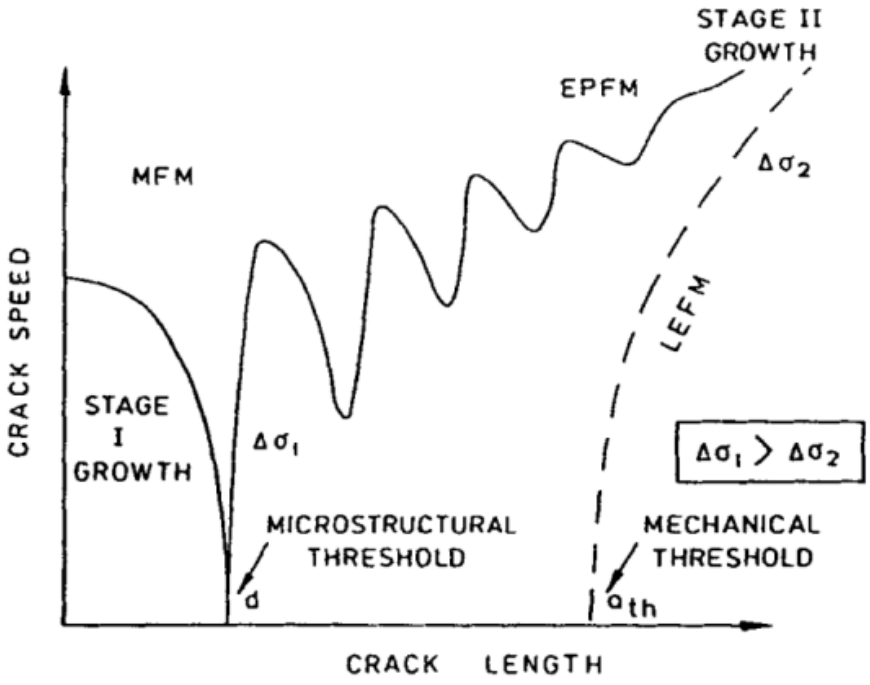

Figure 1.3: Fatigue crack growth behavior of short cracks for tests performed at bulk scale [8].

1.3 Fatigue Properties of Electrodeposited Nickel Thin Films

There is an increasing need to use more damage-robust structural materials, such as in MEMS applications, considering the ongoing miniaturization of structural components in MEMS devices. LIGA nickel thin film is one of the most common components currently used in the MEMS industry. LIGA is an acronym from the German words for 'lithography,' 'electroplating,' and 'molding,' and these processes could implement electrodeposited nickel thin films to fabricate high aspect ratio Ni structures, which are widely used as a variety of micro-sensors and actuators [6, 10, 40-43]. For a large number of MEMS applications, LIGA Ni parts are experiencing the cyclic mechanical loading, and consequently the investigation of fatigue behavior of nickel thin films is a crucial step in developing a reliable MEMS design [44, 45]. In that regard, thickness and grain size effects on fatigue life of metallic films have been extensively studied over the last 20 years [46-53]. Most of these studies are performed with tensile tests, which do not take into account the effects of extreme stress/strain gradients that may exist in actual micro-components (such as in the cyclic bending of micro-beams [54-58]). Among this researches, Yang *et al.* [5] have studied the earliest stages of fatigue crack growth in LIGA Ni MEMS thin films by implementing notched focused ion beam (FIB) microbeam. Their developed technique was used to study submicron and nanoscale fatigue in LIGA Ni thin films with columnar microstructures (average grain size of 25 ± 5 nm). They reported that fatigue crack growth in LIGA Ni MEMS thin films occurs by the unzipping of cracks into intersecting slip bands. This study also highlights the significant importance of grain size on fatigue behavior of nickel thin films. Figure 1.4 (a) shows the predicted fatigue endurance limit (see

equation 11 in [3]) as a function of grain size which is in a reasonable agreement with corresponding experimental data presented in Figure 1.4 (b). Results suggest that thinner thin films which have finer grain size tends to have a larger fatigue endurance limits.

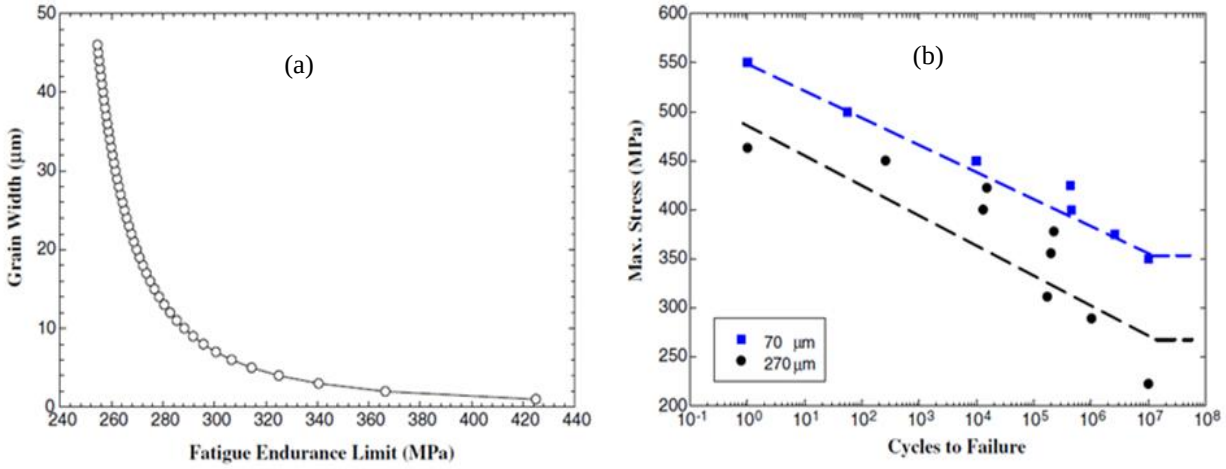

Figure 1.4: (a) Predicted endurance limit as a function of grain size. (b) Experimentally Measured S-N curve for 70 and 270 μm thick LIGA Ni film [3, 4].

Hanlon *et al.* [6, 9] also report beneficial effects of grain size reduction on fatigue resistance of pure Ni under stress-controlled loading condition (see Figure 1.5). As shown in this figure, *nc* (nanocrystalline) structure has a slightly higher fatigue limit compared to *ufc* (ultrafine crystalline). This trend is valid for both endurance limit and the stress range associated to number of cycles to failure. Accordingly, the fatigue limit of *mc* (microcrystalline) Ni is significantly lower than those of *nc* and *ufc* pure Ni. Figure 1.5 highlights the dominant effect of grain size on fatigue behavior of pure Ni.

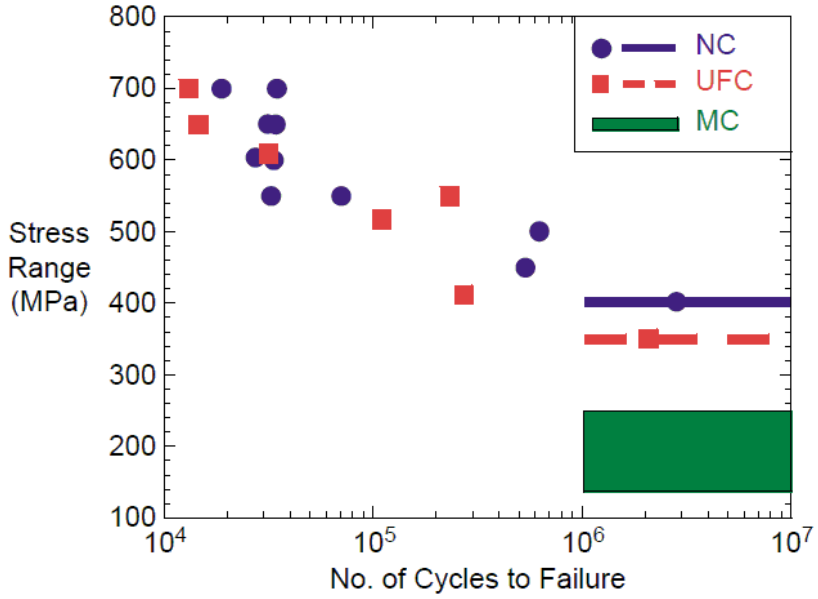

Figure 1.5: The effect of grain size, from micro to nano-regime, on endurance limit [6].

In another effort to study the fatigue behavior of LIGA nickel films, Boyce *et al.* [4] presented a new method to characterize the high-cycle fatigue behavior of nickel micro specimens. In this research, they used cantilever microbeams with a cross-section of 26×250 μm under 20 Hz fully reversed bending load. Although, the used specimens were un-notched, implementing the bending mode of loading results in 6%.μm^{-1} stress gradient. The reported *S-N* curve appears to be consistent with typical ductile metal behavior (Figure 1.6). This figure shows that for applied stresses at the order of the yield strength, the corresponding lifetimes is at the order of several tens of thousands of cycles. The arrows show two specimens with no failure after 3.5×10^6 cycles (exhibited ‘‘run-out’’). These ‘‘runouts’’ occurred at a maximum stress about 208 MPa which is 37% of the ultimate tensile strength and consistent with typical values reported for bulk

nickel [38]. In this research, larger stress gradients (0.17 and 0.36 μm^{-1}) and will be investigated.

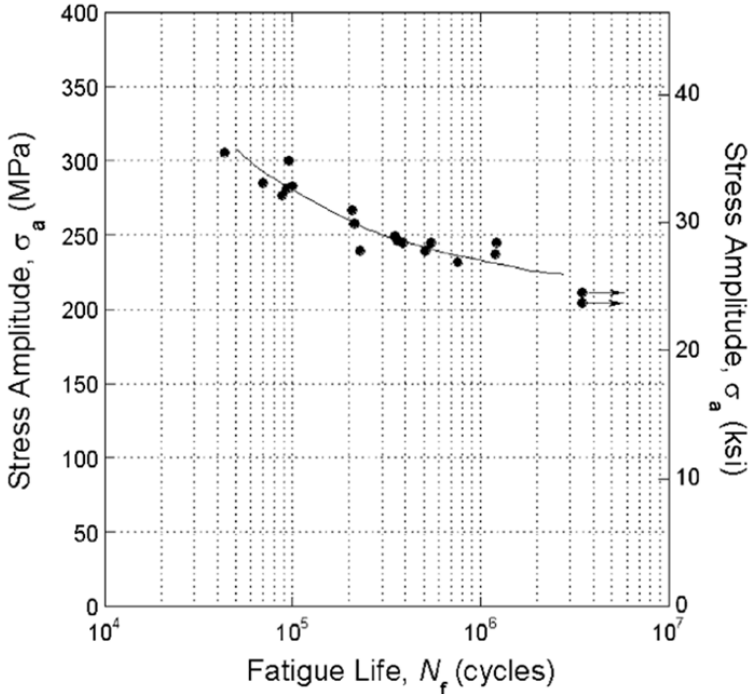

Figure 1.6: S-N curve for 26 μm wide beam under fully reversed bending (*R*=-1). Arrows in this figure representing run-out specimens.

In a similar research, Son *et al.* [7] reported that when the characteristic dimensions of materials become small the corresponding mechanical properties can deviate from those of bulk material. They conducted the tensile and fatigue tests to investigate the effects of stress concentration and surface roughness of LIGA Ni microbeams by performing the same fatigue tests on center-notched (with k_t =1.4) and unnotched specimens to obtain the associated notch sensitivity (see Figure 1.8). The notch-sensitivity factor was computed to be q= 0.65 which is higher than the value

reported for bulk metals [7] and highlights the fatigue strength sensitivity of LIGA nickel to stress concentration (see Figure 1.7).

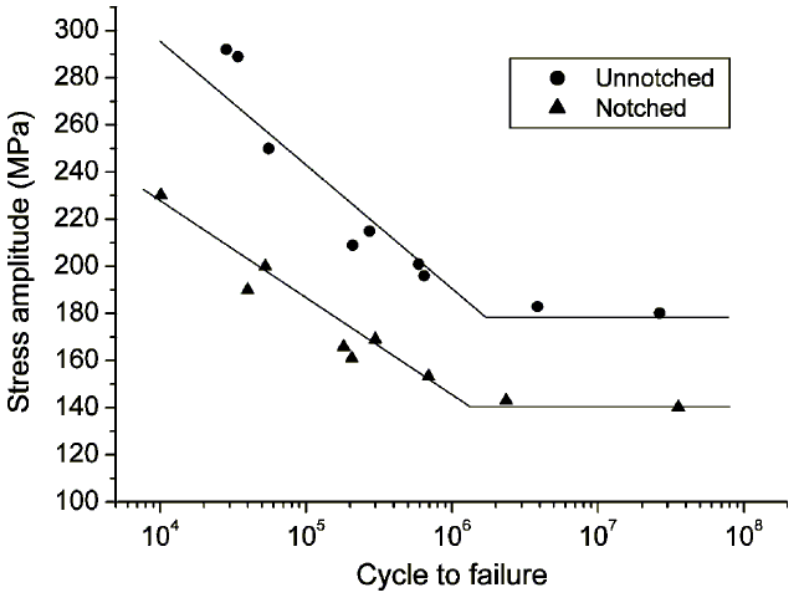

Figure 1.7: Notch effect on S-N curve of LIGA Ni [7].

The fatigue crack growth rates associated with microstructurally small cracks also have been extensively studied in bulk metals [22-27], with computational models starting to capture the main trends [35-37]. However, none of these studies focused on the growth of microstructurally small cracks under extreme stress gradients, which is the topic of this study. Among these researches, Hanlon *et al.* [6, 9] characterized the crack growth behavior of pure Ni as a function of grain size for a wide range (tens of nanometer to tens of micrometer). They compared the fatigue response of electrodeposited nanocrystalline pure Ni (with average range of grain sizes well below 100 nm) with corresponding ultrafine crystalline pure Ni (with an average grain size of

about 300 nm) and conventional microcrystalline (Ni with an average grain size more than 10 μm). In this research, they compared the crack growth rate for different grain size and showed that grain refinement from microcrystalline to the nanocrystalline size could significantly increase the corresponding crack growth rate for the fatigue tests performed under stress-controlled condition. Figure 1.8 (a) shows the crack growth rates as a function of ΔK at load ratio $R = 0.3$. As shown in this figure, rates are about four times faster for *nc* Ni compared to *ufc* Ni and lowest crack growth rates belong to *mc* Ni. Considering the ΔK range, the crack growth rates are in the Paris regime. According the LEFM assumption, only the data points correspond to an uncracked ligament with length of 20 times or more of the plastic zone sizes have been considered [6, 9]. The predicted and experimentally measured fatigue threshold for long crack is reported to be ~1 and 2 MPa$\sqrt{\text{m}}$ respectively [3, 39, 40]. The long and short crack growth rates and associated ΔK range are compared in Figure 1.8 (b), reported by Yang *et al.*[3]. It is important to mention that the majority of researches for investigating the crack growth trend of Ni microbeams have studied the long cracks fatigue behavior and any subcritical growth within the scale of microstructural length is ignored [3, 6, 9]. However, none of these studies focused on the growth of microstructurally small cracks under extreme stress gradients, which is the topic of this study. The geometry and the presence of extreme stress gradient for MEMS devices dictates the necessity of characterizing of the effect of extreme stress gradient on microstructurally small crack growth behavior to address some of the major reliability concern for MEMS application.

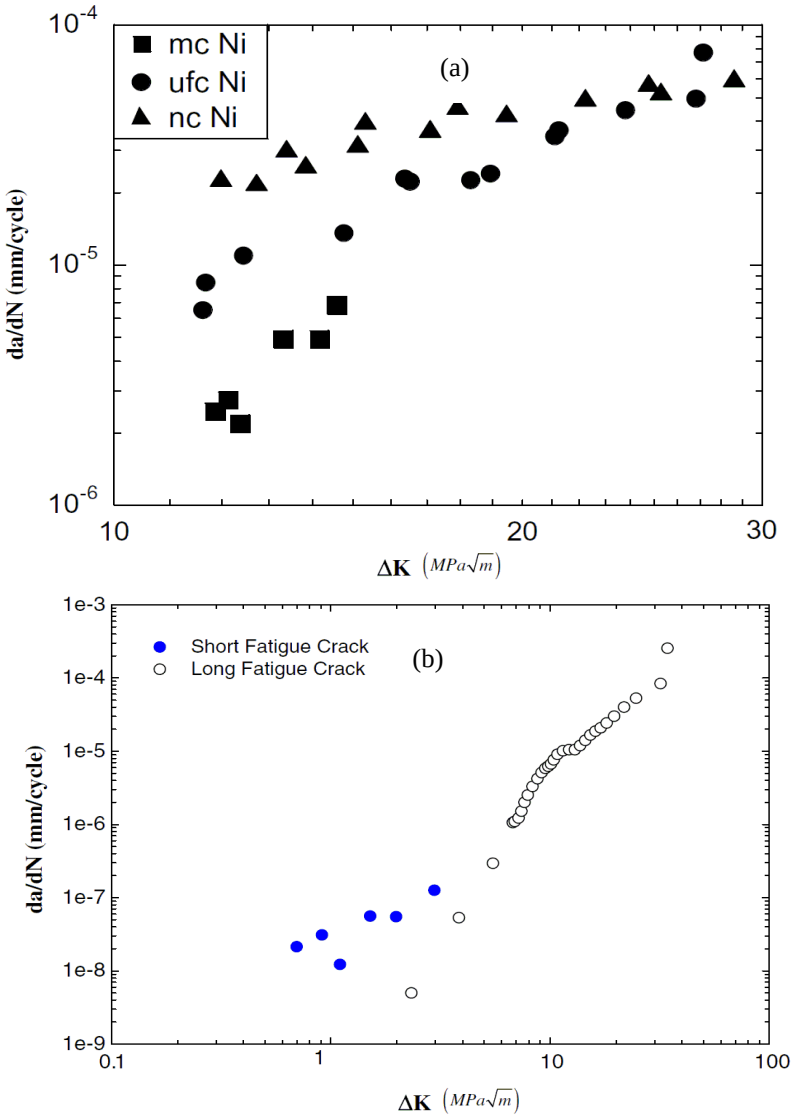

Figure 1.8: (a) Crack growth rates as a function of ΔK, for different grain sizes reported by Hanlon *et al.*[9]. (b) Comparison of long and short fatigue crack growth rates.

1.4 Fatigue Behavior of Ni Microbeams with Extreme Stress Gradients

Fatigue tests for micro-scale components under extreme stress gradients could introduce a new fatigue mechanism that is not applicable for bulk material. For fatigue of non-propagating short crack under an extreme stress gradient, external factors such environmental effects could play a dominant role in the fatigue mechanism. Baumert *et al.* investigated the fatigue crack initiation mechanism in 20-μm-thick electroplated Ni films by using a microresonator, consisting of two comb drives and a notched cantilever beam / mass assembly (see Figure 1.9) [41]. The comb drives are designed for electrostatic actuation (to drive the beam/mass assembly at resonance (f_0 ~ 8 kHz)) and capacitive sensing of the motion (to measure f_0 by performing frequency sweeps throughout a fatigue test).

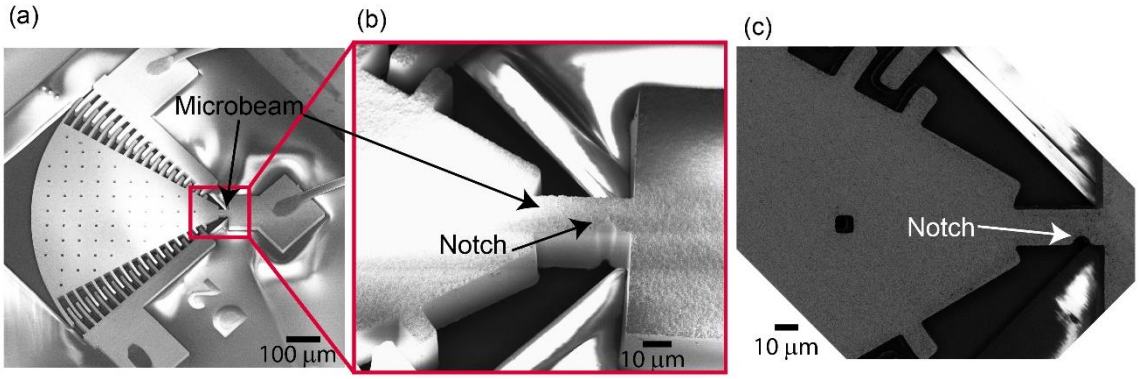

Figure 1.9: Inclined SEM images of (a) entire microresonator, and (b) notched microbeam. Top-down SEM image of the notched microbeam.

In this study, in-plane fatigue bending tests were performed in both mild and harsh environments leading to nonpropagating fatigue micro-cracks. Figure 1.10 illustrates the frequency evolution, SEM and TEM images of two specimens in mild

and harsh environment as presented by Baumert *et al*. [41]. Figure 1.10 (a) presents the frequency evolution in mild and harsh environments. As shown in this figure, the blue line represents the frequency evolution for the fatigue test performed in a mild environment. The figure shows that the blue line reaches a plateau region after about 5×10^8 cycles and that the corresponding specimen had not failed after 2×10^9 cycles. At the notch root of this resonator, the stress σ_a= 389 MPa, which is ~44% of the corresponding ultimate stress (σ_{UTS}) [42].. The increase in resonance frequency for the test performed in a harsh environment (red line) is interpreted as a result of very thick local oxides at the location of extrusions at notch root. Figs. 3 (b, c) show that for sufficiently large stress amplitudes, non-propagating micro-cracks form in both environments. The extrusions associated with these slip bands oxidize during the cyclic loading. The localized thick oxides (~1µm) were reported after several billions of cycles [42]. Figure 1.10 (d) presents the TEM images of highly localized surface oxide at notch root for the test performed in mild environment [41]. This figure shows that after about one billion cycles the fatigue micro-cracks form within previously formed thick oxides.

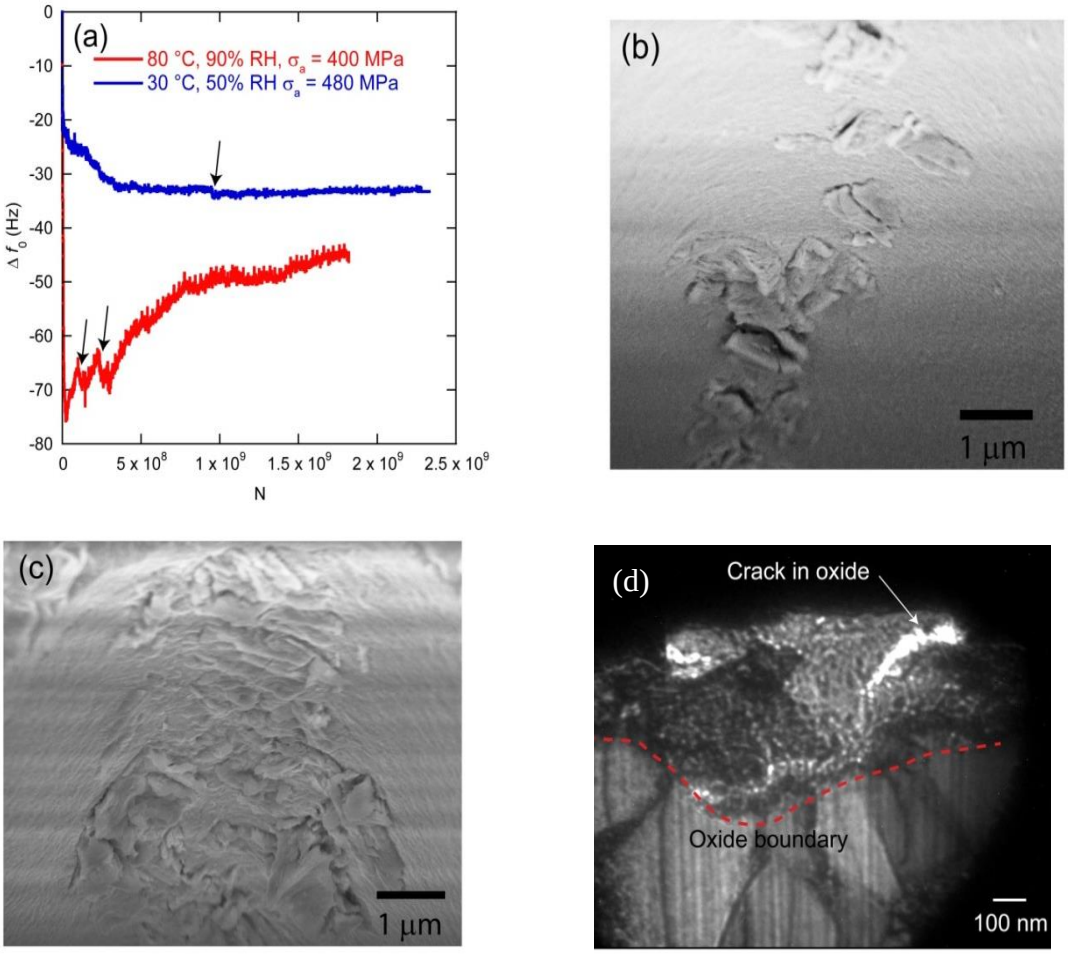

Figure 1.10: (a) Frequency evolution during performed fatigue tests in mild (30 °C, 50% RH at σ_a = 390 MPa) and harsh (80 °C, 90% RH at σ_a = 335 MPa) environments. Arrows indicate sudden drops in f_0. (b, c) resulting fatigue damage at the notch in mild and harsh environments, respectively. (d) TEM images showing highly localized surface oxides, corresponding to the extrusions in (b).

1.5 Motivation

Small-scale fatigue is an active research area due to the widespread application of metallic films and micrometer-scale structures in flexible/stretchable electronics, micro/nano electromechanical systems (MEMS/NEMS), and microelectronics [4, 43-61]. The majority of previous studies have employed the micro-tensile fatigue testing

technique (or similar techniques) on freestanding or polymer-supported thin films. These investigations have not considered the effect of the stress gradient on fatigue behavior which could be significant for notched components under MEMS-relevant loading conditions even in the case of unnotched micro-components under bending loading. Recently, several techniques have been developed to study the bending fatigue properties of microbeams, in an effort to study more complex loading configurations that are pertinent to a growing number of applications (such as metallic micromachines and metallic layers on stretchable/flexible electronics) [4, 43-48, 52, 53, 55, 56]. Notably, Pierron and co-workers developed a microresonator technique to measure the high / very high cycle fatigue properties (HCF/VHCF) of electroplated Ni notched microbeams under fully-reversed bending mode [43-45, 52]. They investigated fatigue crack initiation mechanism in the VHCF regime (see section 1.4) [45]. In this research, we demonstrate that the propagation of microstructurally small cracks under extreme stress gradients is the dominant factor which mainly determines the number of cycles required for fatigue failure. Therefore, the necessity of prediction of N_f for micro-components in order to compute their corresponding fatigue life highlights the importance of developing a technique to accurately characterize the small crack growth rates. The unique technique presented in this dissertation, for the first time enables us to quantify the extreme stress gradient effects on the fatigue behavior of LIGA Ni microbeams in different environments, specifically propagation of microstructurally small cracks. To do this, fatigue tests were performed on microresonators with stress gradients of 0.17 and 0.36 μm^{-1} to investigate the stress gradient and environmental effects on the fatigue life. Specifically, larger electrostatic moments (up to 4 times in

magnitude) were applied onto the micro-resonators, allowing the fatigue cracks to propagate (unlike the previous investigations in which only non-propagating cracks were observed). As such, these experiments allowed the investigation of the combination of the following size effects on small-scale fatigue: physical (with the presence of extreme stress gradients ahead of the microbeam's notch) and microstructural (for which the critical cracks are commensurate with the grain size).

CHAPTER 2: EXPERIMENTAL AND NUMERICAL PROCEDURES

2.1 Microresonators

A free standing 20-μm-thick LIGA nickel microresonator is shown in Figure 2.1. This microresonator is used to characterize the fatigue properties of nickel microbeams in the High / Very High Cycle Fatigue (VHCF) regime. As illustrated in Figure 2.1, design #1, consists of two comb drives, a cantilever beam, and a mass. The comb drives are designed for electrostatic actuation and capacitance sensing. In this particular design, the small holes on the fan-shaped mass are used to facilitate the etching process of the trench under the mass to provide a fully free standing fan attached to the base with a free standing microbeam as shown in Figure 2.1 (b). Due to the small dimension of the combs' fingers, the electrostatic moment cannot provide sufficient force and motion to the resonator mass under monotonic loading; consequently the resonator is driven at its natural frequency, which is dictated by the dimensions of the device.

This microresonator can be used to investigate fatigue damage at the notch root (see Figure 2.1 (b)) of the nickel beam under cyclic in-plane bending [10]. As a stress raiser, the notch is designed to increase the local stress at the notch root to a desired level. The large stress gradients are induced by the 4-micron-root-radius sharp notch and the small width of the beam as shown in Figure 2.1 (b). The objective is to characterize the fatigue properties of 20-μm-thick LIGA nickel microbeams under extreme stress gradients. To study the specific effects of stress gradients, different notch shapes are designed, fabricated and tested. In the next section, the fabrication process

and technical limitations which have been considered for microresonator final design are discussed.

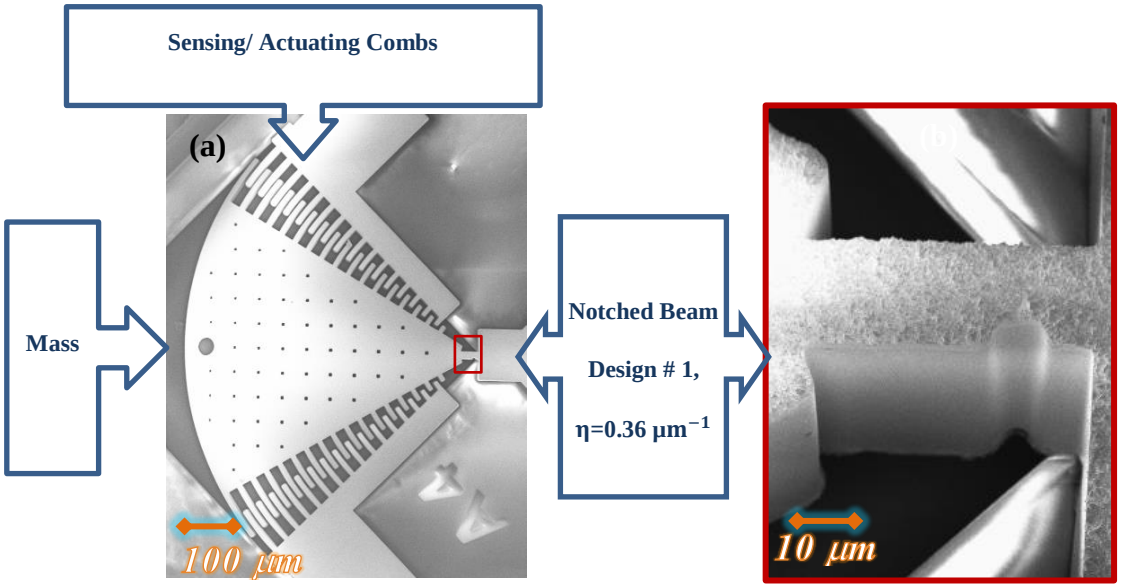

Figure 2.1: (a) Resonator with the highest normalized stress gradient (η = 0.36 μm^{-1}). (b) Zoomed view of the beam notch.

2.2 Fabrication Process

The metal multi-user MEMS process (MetalMUMPs) is a commercially developed process, in which 20-μm-thick electroplated nickel is used as the structural layer with 0.5 μm thick Cu base layer at the bottom and 0.5 μm thick Au layer at the top [62]. Several lithography levels are needed to create the above mentioned physical layers. More details about the fabrication process are available in user guide, MetalMUMPs Design Handbook, which is designed for general purpose electroplated nickel micromachining of MEMS [63]. For MEMS devices fabricated with this process,

the nickel layer has columnar grains which are typically 5–10 μm in height and roughly 1-2 μm in width along directions orthogonal to the deposition direction [4, 43].

The experimental data of monotonic tensile loading of MetalMUMPs nickel beam has been reported by Baumert *et al.* [64]. In this study, dogbone-shaped specimens (20 μm thick, 8 μm wide, and 320 μm long) were used for monotonic tensile tests; the extracted experimental data are summarized in Table 1.

Table 1: Material properties of 20-μm-thick electroplated nickel fabricated with MetalMUMPs process [64].

Material Properties	**Young's Modulus [GPa]**	**0.2% Yield Strength [MPa]**	**Tensile Strength σ_{UTS} [MPa]**	**Elongation[%]**
20-μm-thick Nickel film	166±19	656±70	873±26	7±3

These material properties have been implemented in a finite element model to optimize the microresonators design and to reach a desired range of parameters for fatigue test. The resolution provided by this process is about 8 μm which dictates the minimum possible clearance of fingers at the sensing and actuating combs [63]. The upper limit to the size of the microresonator is largely determined by resulted residual stress during the fabrication process [63].The residual stress in the electroplated nickel film has an average of -4.72 MPa/μm [65]. For very large MEMS devices, process-induced residual stresses bend the free standing mass downward, decrease the overlapped area between the sensing and actuation fingers, and cause the malfunction of device. These process

parameters and their direct and indirect effect on fabricated device have been precisely considered and implemented, and details at next sections.

2.3 Governing Equations

The dynamic behavior of resonators has been modeled as a one-degree-of-freedom, harmonic oscillator with rotational motion [64]. The governing second-order equation is:

$$J_\theta \ddot{\theta} + b\dot{\theta} + k_\theta \theta = M_0 \sin(2\pi f t), \quad (3)$$

where θ is the angle of rotation, J_θ is the mass moment of inertia, b is the constant damping coefficient, k_θ is the torsional stiffness. The maximum amplitude of applied moment, M_0, is presented below [64]:

$$M_0 = \frac{1}{4}\varepsilon h \sum_{j=1}^{2(n-1)} \frac{1}{ln(\frac{r_{o,j}}{r_{i,j}})} V_{in}^2, \quad (4)$$

where V_{in} is the amplitude of actuation voltage, ε is the electrical permittivity (here for air) h is the film thickness (20 μm), $r_{i,j}$ are the outer and inner radius of jth capacitor (for two adjacent fingers), n is number of microresonator's sensing comb fingers (17 and 14 for 0.36 and 0.17 μm^{-1} respectively). This formula considers the area of two adjacent fingers which see each other (overlapped) to calculate the corresponding capacity. And finally f is the frequency of applied moment. Accordingly f_0 is defined as:

$$f_0 = \frac{1}{2\pi}\sqrt{\frac{k_\theta}{J_\theta}}, \quad (5)$$

At resonance, the notched beam is cycled under fully-reversed sinusoidal in-plane bending, with an amplitude of rotation at resonance, θ_0, given by the following equation [64]:

$$\theta_0 = \frac{M_0 Q}{k_\theta}, \tag{6}$$

with M_0, the amplitude of the applied moment, k_0 the torsional stiffness of the specimen, and Q the quality factor. This formulation and FEM analysis will be used to interpret the frequency evolution as a result of crack initiation and propagation at the notch root.

2.4 Design Criteria

The MEMS resonators are designed to study the short fatigue crack initiation and propagation under a wide range of stress gradients. A fully parameterized APDL (ANSYS Parametric Design Language) code was developed to finalize the microresonator design (section 2.6). As illustrated in Figure 2.2 (a), an elastic finite element model was used to calculate the stress distribution throughout the notch root thickness (designated as Thickness Path), the ligament of the beam (Surface Path), and along the notch length (Arc1 and 2 Paths). The latter was used to compute the size of the fatigue-exposed zone. Figure 2.2 (b) shows a schematic of stress distribution along the ligament of the beam (solid blue line). To investigate the crack initiation and propagation under constant stress gradient, stress distribution along the beam ligament must be linear, i.e. the dashed red line instead of the solid blue one. By assuming linear stress distribution along the beam ligament, the normalized stress gradient is rewritten as:

$$\eta = \frac{1}{\sigma}\frac{d\sigma}{dx} \tag{7}$$

where, η is normalized stress gradient, σ_a is the maximum stress at the notch root and σ_b is the minimum stress (here zero) at the middle of the beam, Figure 2.2 (b). To study short fatigue crack initiation and propagation, initially values of η were selected as 0.06, 0.13, 0.17, and 0.36 μm^{-1}.

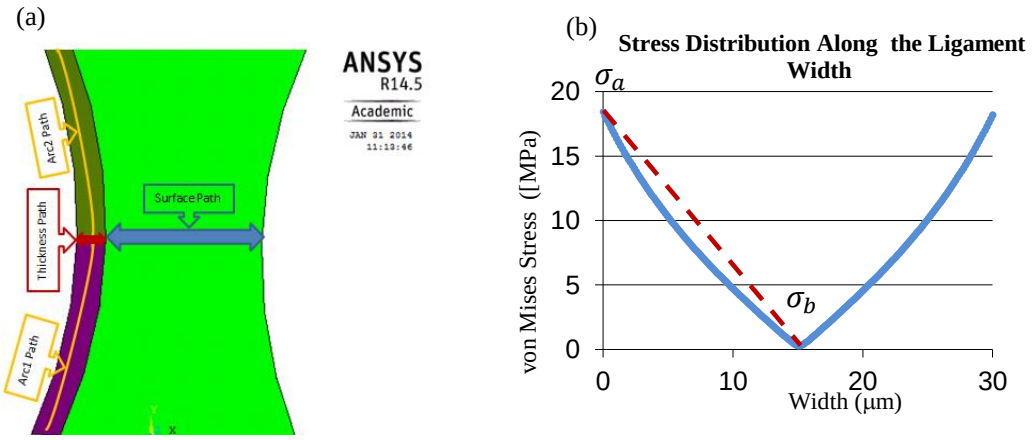

Figure 2.2: (a) FEM Model and different paths for stress distribution at the beam section. (b) A schematic of stress distribution along the ligament (solid blue line).

Figure 2.3 presents the shape for the notched beam, which consists of three parameters (W_{min}, W_{max}, and Length). Using equation (7) and the defined range for stress gradient, corresponding first parameter of beam geometry (W_{min}) was computed and listed in Table 2. Based on the FEM model results, to have the same size of fatigue-exposed zone, the W_{max} / W_{min} ratio must be constant for all different designs. This ratio is set to 1.28, as a higher ratio could result in nonlinear stress distribution along the ligament. The final level of the beam design section is to define the length of beam. Again considering the FEM model results, beam length was set to 60 μm; a shorter

length could result in nonlinear stress distribution and a longer one could result in more out-of-plane bending of the resonator mass and the device malfunction.

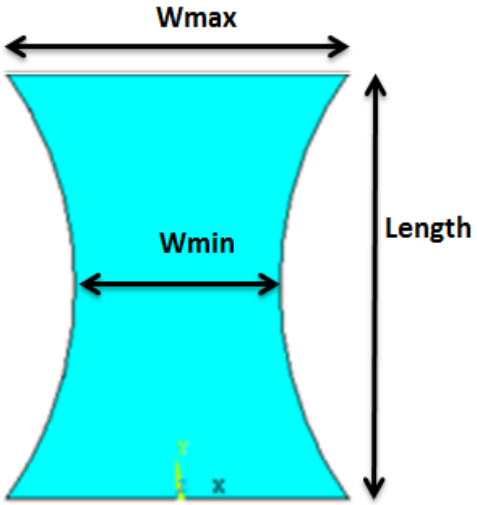

Figure 2.3: Design parameters for the beam section.

Table 2 shows the different parameters corresponding to different designs of the microresonator. In this table k_θ and $\frac{\sigma}{\theta}$, respectively are the stiffness of beam and ratio of stress level at notch root over corresponding angle of rotation which is constant for each individual microresonator. Using the 3D FEM model and assuming linear elastic behavior model, $\frac{\sigma}{\theta}$ and k_θ were computed for different designs, along with corresponding stress gradients and are presented in *Table 2*. Figure 2.4 shows the newly designed microresonators (designs # 2, 3, and 4 from *Table 2*) with different stress gradients. All designed microresonators have been characterized (see chapter 3 for more details) and design# 1, 2 have been selected to perform the fatigue test and study the effects of stress gradient on short fatigue crack initiation and propagation. Design # 1 is presented in Figure 2.1.

Table 2: Different designs of microresonator and their corresponding parameters.

Design #	W_{max} ***[μm]***	W_{min} ***[μm]***	**σ/θ** ***[MPa/mrad]***	k_θ ***[N.m/rad]***	η $[\mu m^{-1}]$
1	-	-	62.64	1.730E-05	0.36
2	10.66	8.33	21.29	9.443E-06	0.17
3	16	12.5	25.55	2.030E-05	0.13
4	32	25	42.87	1.274E-04	0.064

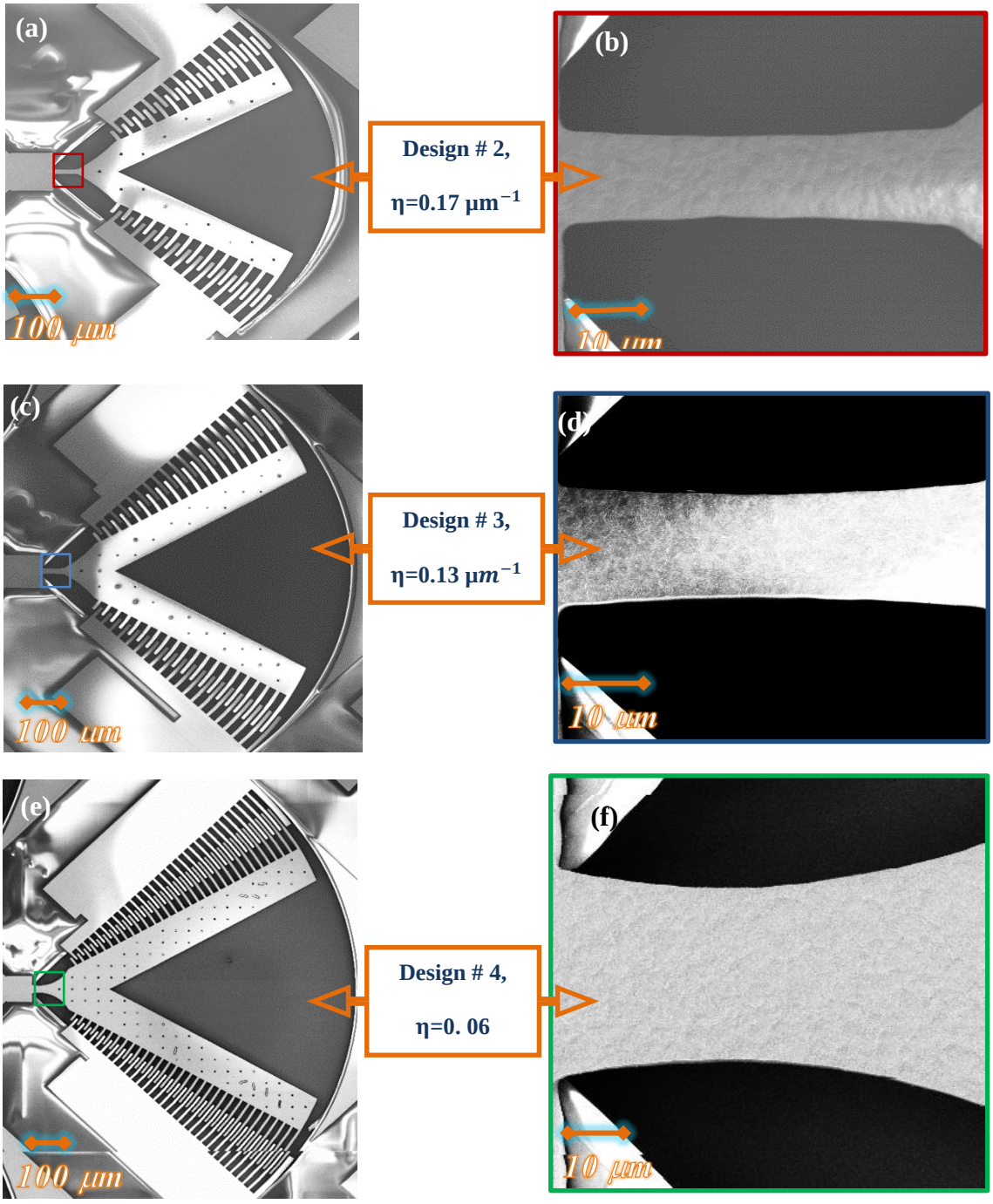

Figure 2.4: Designed microresonators to characterize the fatigue properties of LIGA nickel thin film under different stress gradient. (a, b) $\eta = 0.17\ \mu m^{-1}$, design#2. (c, d) $\eta = 0.13\ \mu m^{-1}$, design#3. (e, f) $\eta = 0.06\ \mu m^{-1}$, design #4.

2.5 Experimental Setup

2.5.1 Fatigue Test Setup in Controlled Environment

The quality factor for designed resonators is of the order of several hundred and makes it possible to rotate the resonator mass by keeping it running at resonance ~ 8 kHz. Figure 2.5 illustrates the different features of the setup for performing HCF/VHCF tests. The resonator behaves as a rotational oscillator excited by applying sinusoidal voltage using a waveform generator (voltage is generated with Agilent33220A 20MHz and then amplified by 100x with AVTECH-100G). The periodic rotational motion under resonance results in periodic changes in the capacitance of the sensing combs. An Agilent E3612A applies DC bias to the sensing combs to measure their capacitance changes. The capacitance changes create a current (~nA) that is proportional to the mechanical response of device (angle of rotation of the resonator). The induced current is converted to voltage using a custom made current-voltage amplifier. Then the amplified voltage is measured with a lock-in amplifier (SR830-100kHz DSP). The output signal at resonance depends on angle of rotation and approximated as:

$$V_{\text{out}} = \alpha\theta, \tag{8}$$

where α is a constant and function of the gain of the current-to-voltage amplifier circuit and the geometry of the sensing comb structure [64, 66] .

By tracking the resonant frequency changes, the development of fatigue damage is followed and interpreted as crack initiation and propagation at the notch root. Fatigue tests are performed in both mild and harsh environments using a temperature and humidity chamber (ESPEC SH-241 Bench-top Type). This chamber controls the environment by resolution of 0.1 ºC, 1 % relative humidity (RH).

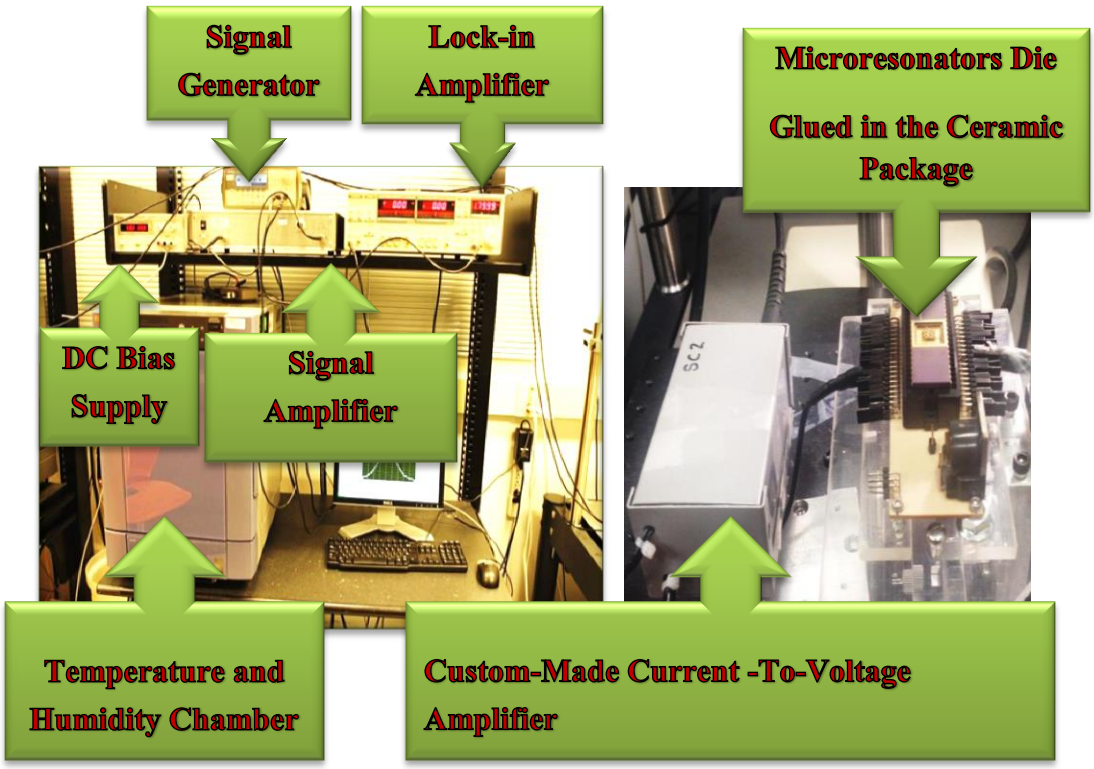

Figure 2.5: HCF Fatigue test setup used for tracking the changes in resonant frequency during the test.

2.5.2 Optical Calibration/ Stress and Strain Calculations

As mentioned earlier, during the fabrication process, a device's geometry can vary slightly; such small changes can create variations in the device's response amplitude and its resonant frequency. To address this concern, the stress and strain were computed at the notch roots of the resonators using a combination of FEM analysis and optical calibration for each individual device. This approach helps to produce consistent results and, consequently, a correct interpretation of fatigue damage behavior. For optical calibration, a digital camera (JAI-PULNiX RM-1402CL) was used. Because of the significant differences in the dimensions of the designed resonators, objective lenses

with different magnification (20X, 50X Mitutoyo Plan Apo SL Series) were used to compute the angle of rotation of each resonator. We have computed the angle of rotation of each resonator to characterize the response amplitude of that individual resonator.

Figure 2.6 is an image of the last few fingers of the resonator combs during the fatigue test. By measuring the blur area and knowing the geometry of the device, the angle of rotation can be computed. In the previously developed method to measure the resonator's angle of rotation, the motion of the comb was calculated by measuring the motion blur of the root of combs between the last two fingers of the resonator mass (designated as red arrow Figure 2.6 (a)) [67]. In this method rest- and motion-images of the device are obtained and matched to capture the pixel intensity distribution in motion-blur. This approach results in reasonably precise measurement of the angle of rotation for Si microresonators [62, 68].This technique does not appear to yield accurate results for large θ_0 values of the Ni microresonators, probably due to poor contrast between the fingers and the background (see Figure 2.6(a)) [67]. Hence, a new calibration scheme was used, relying on measuring the distance between a finger at rest and the edge of the adjacent blurred area.

In this new method, instead of measuring blur motion, which is the direct motion of the comb root, the motion of the moving comb root is measured with respect to the fixed comb. In other words, the distance between the fixed comb and the moving comb root is computed and subtracted to obtain the angle of rotation (difference in the size of designated red arrows in Figure 2.6 (b, c)).

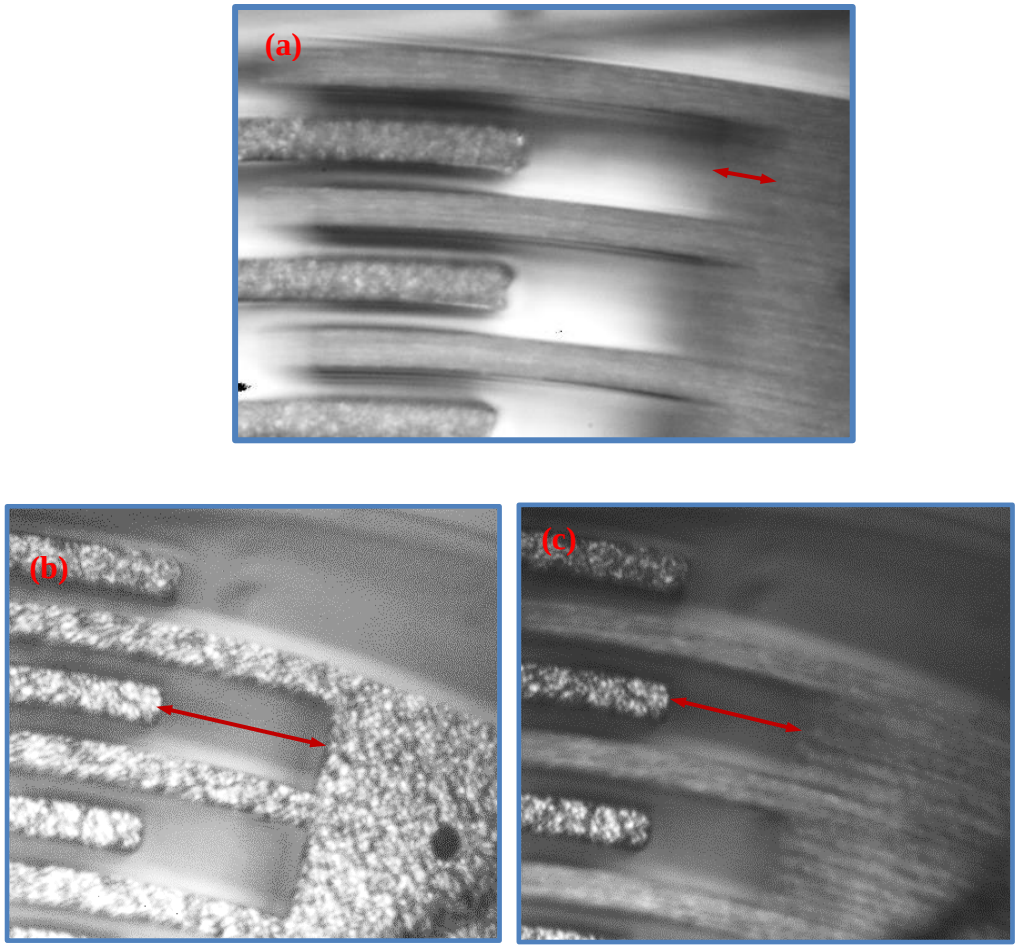

Figure 2.6: Resonator images during the fatigue test used to measure the motion blur area and compute the angle of rotation of microresonator.

To characterize the resonator's response amplitude, a matlab code was written to compute the designated length and consequently the comb motion. Since one extent of this length is fixed (see Figure 2.6 (c), the blur is only seen at one extent (the moving comb root). Therefore, computing this length instead of the blur motion results in smaller error and thus higher precision. This characteristic of the new approach enables the specified length to be measured even at higher stresses. This is a significant improvement over the previous method, which was unable to capture the blur length

due to the aforementioned difficulty. To fully obtain the precision offered by this method, the resonator's angle of rotation was calculated using the new method for three devices and for each of five intervals (amplitudes). The precision values from the different devices were calculated and averaged to compute the overall precision. The new method's overall precision is calculated as 0.26 mrad.

In the following paragraph we discuss the step by step procedure to calculate the strain and stress at the notch root of the resonator, which corresponds to its measured angle of rotation by optical calibration. It is worth mentioning that the fatigue damage that occurs during the HCF test could change the amplitude response of the resonator and its corresponding angle of rotation; consequently, optical calibration was performed prior to the test. Given the dimensions of the resonator and its measured blur-motion area, a simple mathematical calculation was used to compute the device's corresponding angle of rotation. Subsequently, a FEM model was implemented to calculate the strain amplitude at the notch root [64].

For the stress calculation, the computed angle of rotation that corresponds to the maximum strain amplitude was used to estimate the stress level at the notch root. Because of plasticity effects, the response amplitude of the nickel resonators is not linear, especially for higher levels of stress. Therefore, it is not realistic to use a linear relation between the stress amplitude and the resonator's angle of rotation. Instead a Linear-elastic plastic model was used to compute the stress at the notch root. Considering Table 1, the Ramberg-Osgood fit was used to obtain the material nonlinearity for the FEM model according to the following equation:

$$\sigma = (1451\ MPa)\varepsilon_P{}^{0.136} \quad (9)$$

By implementing the above mentioned linear-elastic plastic behavior in the model, the FEM model was used to extract the stresses at the notch root σ_a, as a function of angle of rotation θ_0 (in rad), for different levels of applied static loading for the microresonator with 0.36 μm^{-1} stress gradient. Finally, a second-order polynomial was fitted to present the stress (in MPa) versus angle of rotation (in rad) as follows:

$$\sigma_a(MPa) = 74.3 \times 10^3\theta_0 - 1.98 \times 10^6{\theta_0}^2, \quad \text{for T} = 30°\text{C} \quad (10)$$

$$\sigma_a(MPa) = 71.9 \times 10^3\theta_0 - 1.91 \times 10^6{\theta_0}^2, \quad \text{for T} = 80°\text{C} \quad (11)$$

Young's modulus values range from 172 GPa to 166 GPa, corresponding to 30°C and 80°C respectively. The formula for T = 80°C (eq.(10)) has been extracted by replacing the corresponding Young module in the FEM model.

For each individual resonator, the stress at the notch root was calculated by substituting the corresponding angle of rotation in equations (10, 11). It is worth noting that the above mentioned formula is obtained for the resonator with a 0.36 μm^{-1} stress gradient. For other designs (corresponding to a different stress gradient) a different formula should be used instead of equations (10, 11). These formulas have been extracted by implementing the material properties in the corresponding FEM model, and they have been used to compute the stress amplitude at the notch root. For a microresonator with $\eta = 0.17\ \mu m^{-1}$ stress gradient, a second-order polynomial was fitted to present the stress (in MPa) versus angle of rotation (in rad) as follows:

$$\sigma_a(MPa) = 24.54 \times 10^3\theta_0 - 2.23 \times 10^5{\theta_0}^2, \quad \text{for T} = 30°\text{C} \quad (12)$$

$$\sigma_a(MPa) = 23.73 \times 10^3\theta_0 - 2.09 \times 10^5{\theta_0}^2, \quad \text{for T} = 80°\text{C} \quad (13)$$

The above mention fitted polynomial (equations 10-13) has been used to estimate the stress level at notch root during the fatigue test. Figure 2.7 shows the predicted stress (σ_a from equations (10-13)) versus angle of rotation, θ_0, for the microresonators with $\eta = 0.36$ and $0.17\ \mu m^{-1}$ stress gradient at both environments.

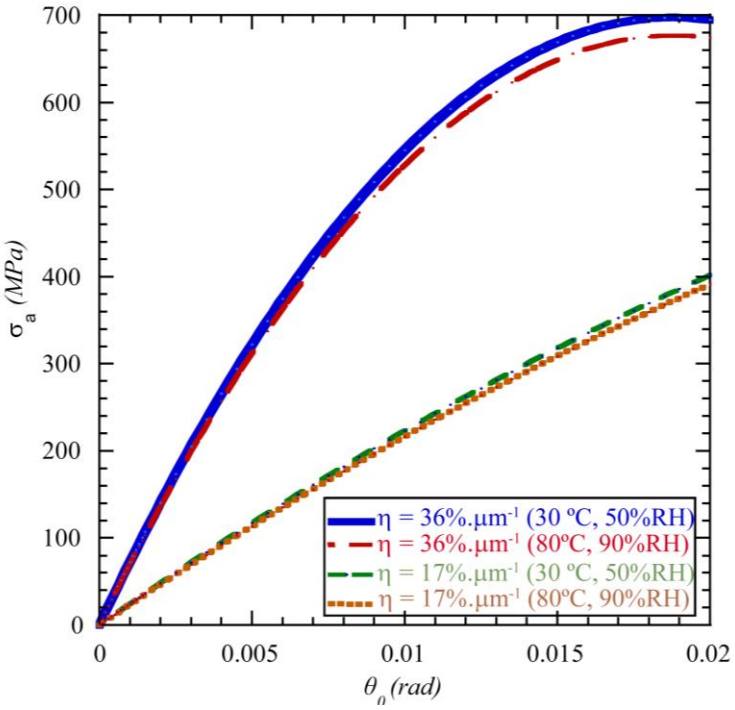

Figure 2.7: Predicted stress (in MPa) versus angle of rotation (in rad).

2.6 FEM Analysis

FEM models have been developed for designing the micro-resonator (see section 2.4) as well as for further understanding thermal and micro- mechanical behavior of these devices during the fatigue tests. Because many parameters were involved in the resonator design, a fully parameterized Ansys model (APDL code) was developed to model the different resonators corresponding to different stress gradients. To model a particular resonator, the APDL code asks for the resonator design

parameters, including the number of comb fingers, the beam and its notch dimensions, the resonator shape and dimension, material properties, etc. Some of these parameters are illustrated in Figure 2.8 (a). The material properties were implemented using data from Table 1 and the Ramberg-Osgood fit (equation (9)). After implementing the above mentioned parameters for each individual design, the APDL code uses PLANE82 and SOLID186 elements to generate 2D and 3D models respectively. Figure 2.8 (b) shows the 3D model of the designed resonator with 14-finger combs and with η equal to 0.17 μm^{-1}. All the models were constrained by setting the displacements to zero at the base of the beam. Figure 2.8 (c) gives an example of the stress distribution through the beam ligament and notch root thickness; this was used to compute the size of the fatigue-exposed zone. For modal analysis the resonant frequency is computed using a block Lanczos method. Mesh convergence was studied for both static and modal analysis, Figure 2.8 (d).

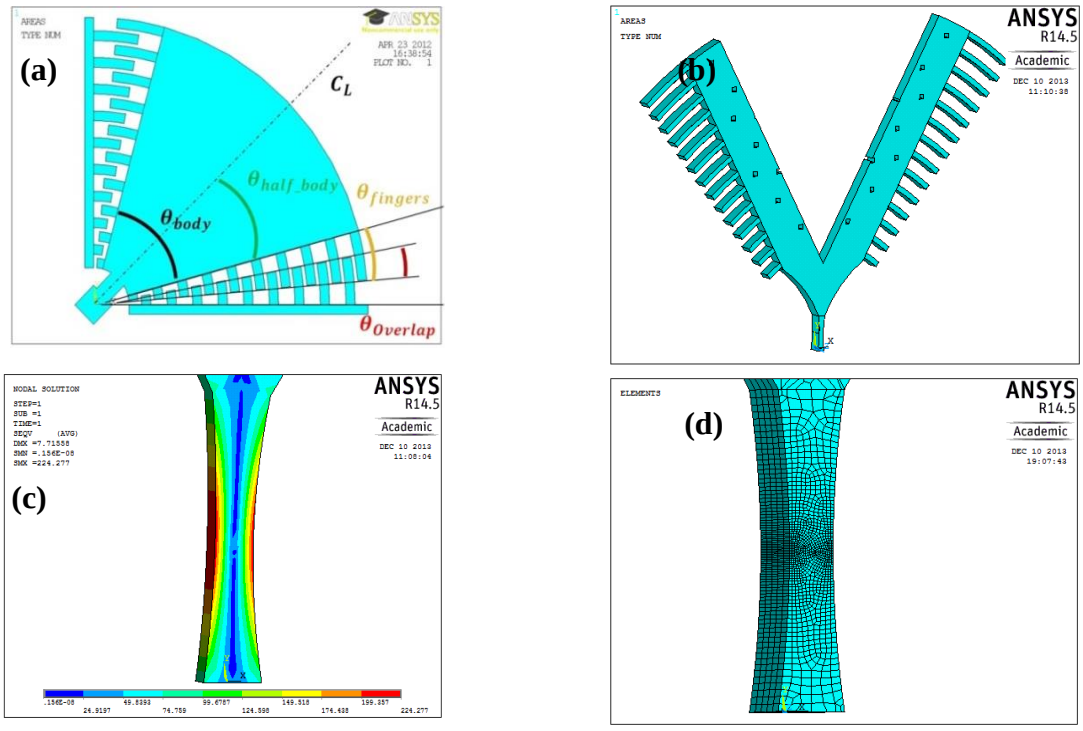

Figure 2.8: (a) Schematic of designed microresonator with fully parameterized APDL code. (b) 3D model for the designed resonator with η equals to 0.17 μm^{-1}. (c) Stress distribution through the beam ligament. (d) Image of notched beam and its meshing.

2.6.1 Crack Propagation Model

From the performed fatigue test, the resonant frequency decrease versus the number of cycles was extracted. In this section, a FEM model to correlate crack growth at the notch root to frequency decrease at the micro resonator is presented. The crack growth relation with frequency changes from the FEM model, was used to calculate crack growth rate in section 2.9. To model the crack propagation for the micro resonator with $\eta = 0.36\ \mu m^{-1}$ stress gradient, it has been assumed that a 2D thickness crack throughout the beam initiates at the notch root and propagates towards the neutral axis of the beam (as seen in Figure 2.9).

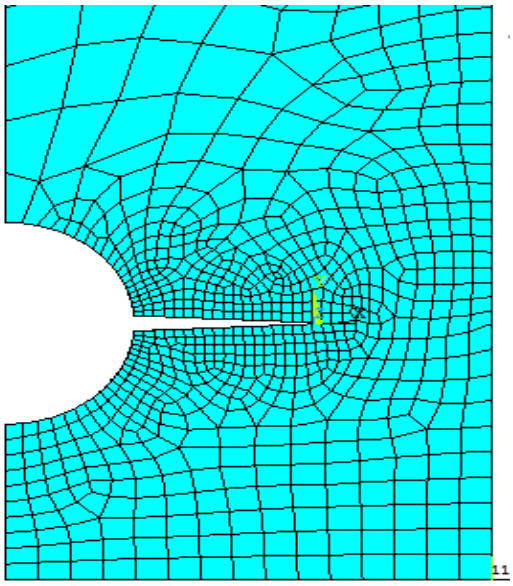

Figure 2.9: Finite-Element model for crack propagation at notch root of the micro resonator with $\eta = 0.36\ \mu m^{-1}$.

Another FEM model has been developed to study the crack propagation for micro resonator with $\eta = 0.17\ \mu m^{-1}$. Similarly, the results from FEM model of micro resonator with $\eta = 0.17\ \mu m^{-1}$ were used to calculate crack propagation rates in section 2.9, to be compared with the $0.36\ \mu m^{-1}$ stress gradient. As seen in Figure 2.10 , for micro resonator with $\eta = 0.17\ \mu m^{-1}$, it is assumed that two throughout (2D) cracks initiate and propagate simultaneously on both sides of beam towards the neutral axis. Based on the observed cracks for micro resonators with 0.36 and 0.17 μm^{-1} stress gradients, the crack opening displacement is assumed to be 300 nm for FEM modeling(see SEM images at chapter 4 and 5).

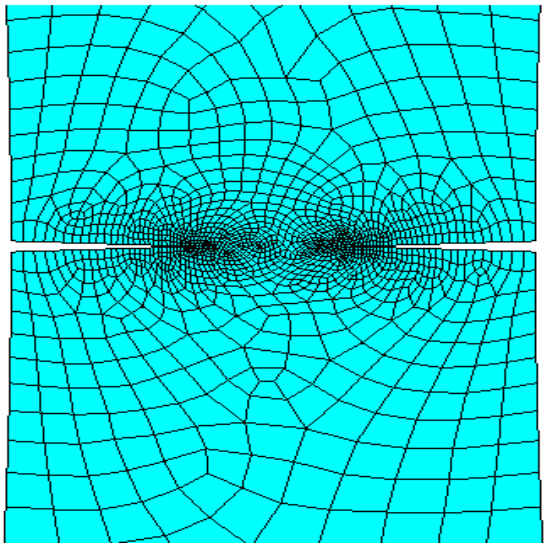

Figure 2.10: Finite-Element model for crack propagation at notch root of the micro resonator with 0.17 μm^{-1} stress gradient.

2.6.2 Temperature Evaluation Model

The microresonators, are sensitive to temperature variations, affecting their resonant frequency [64]. On the other hand, in this study the frequency response of the microresonator is used as a basis for fatigue analysis of the microresonator. That means to investigate the fatigue behavior of these resonators, it is necessary to distinguish a frequency-decrease induced by fatigue damage from one induced by a temperature increase (and resulting in a decrease in elastic modulus) possibly due to dislocation damping. To exclude temperature effects from frequency evolution, we first need to further study the temperature distribution along the ligament during the fatigue test.To do so, we implemented a FEM model to study the steady state temperature distribution across the micro-resonators for a given localized increase in temperature (at the notch root). In this model, experimentally-measured stress-strain data (Ramberg-Osgood fit, equation (9)) has been used as the structural properties of the micro-resonator. Also

Young's modulus values ranging from 142 GPa to 172 GPa, corresponding to 300°C and 30°C respectively. Table 3 represents the other material properties that have been used in the FEM Model. For micro-electromechanical systems (MEMS), it is best to set up problems in more convenient units (μMKSV or μMSVfA) considering the micron size of the devices. For convenience, the following table list the conversion factors from standard MKS units to μMKSV units (micrometer, kilogram, second, volt, pico-ampere).

Table 3: Material properties used in the FEM Model.

Material	***Ni***		***Air(20 °C)***	
Systems of Unit	**MKS**	**μMKSV**	**MKS**	**μMKSV**
Thermal Conductivity	***W/(m)(°C)***	***pW/(μm)(°C)***	***W/(m)(°C)***	***pW/(μm)(°C)***
	90.9	9.09E+7	0.0257	2.57E+4
Density	kg/m^3	$kg/(\mu m)^3$	kg/m^3	$kg/(\mu m)^3$
	8910	8.91E-15	1.21	1.21E-18
Specific Heat Capacity	***J/(kg)(°C)***	***pJ/(kg)(°C)***	***J/(kg)(°C)***	***pJ/(kg)(°C)***
	440	4.40E+14	1.005	1005
Thermal Expansion	$m \cdot m^{-1} \cdot K^{-1}$	$\mu m \cdot \mu m^{-1} \cdot K^{-1}$	$w/(m^2)(°C)$	$pW/(\mu m)^2(°C)$
	1.34E-5	1.34E-5	50	50
Convective Heat Transfer coefficient	-	-	$m \cdot m^{-1} \cdot K^{-1}$	$\mu m \cdot \mu m^{-1} \cdot K^{-1}$
			3.43E-3	3.43E-3

As shown in Figure 2.11, the micro resonator is anchored at a silicon substrate and stands 20 microns above the substrate; see the trench below the micro-resonator's mass. To model the heat exchange boundary condition, it was assumed that the micro resonator is thermally isolated at the base where it is anchored to the substrate. Also the bottom surface of the fan is only exposed to heat conduction through air, which is rationalized by the large dominance of heat conduction over convection through the thin air layer (see the trench at Figure 2.11). The substrate under the trench is assumed to be at room temperature. All other surfaces were exposed to heat convection through free air at room temperature. It was determined that changes of heat convection coefficient in a very large range, 50-200 pw/ μm^2.C (air's maximum convection coefficient), do not lead to noticeable changes in the temperature distribution of the micro-resonator, meaning the effect of the resonator's motion on heat convection is negligible. To sufficiently simplify the thermal modeling of the micro-resonator, a constant, local, high temperature has been considered at notch root as the initial condition to model heat generation due to dislocation damping.

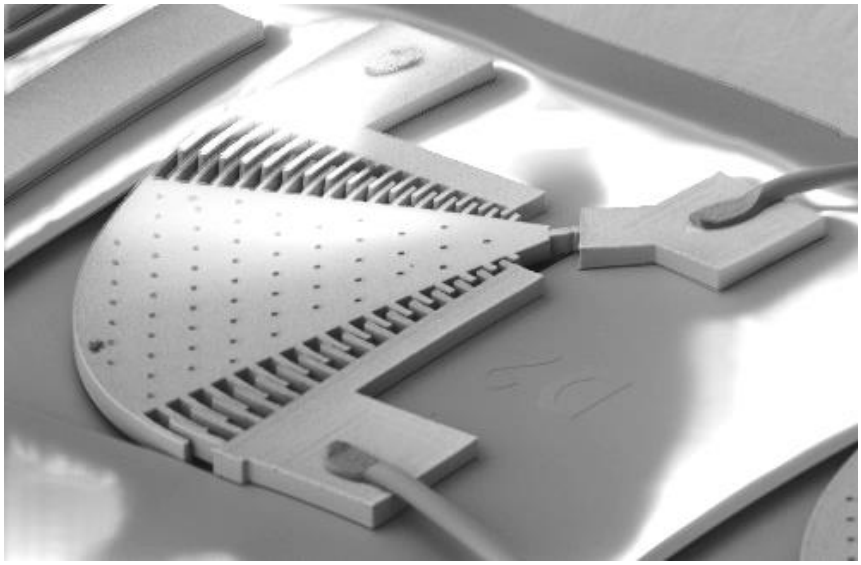

Figure 2.11: SEM image of tilted microresonator.

High order 2D and 3D thermal elements (PLANE77 and SOLID70 respectively) have been used to run a linear steady-state thermal analysis with constant material properties (see Table 3) to determine steady-state temperature contours along the beam ligament. A mesh convergence study has been performed for the developed FEM model. Based on IR camera observations presented in next section, we know that local temperature at the notch root of the micro-resonator will not exceed 200℃ during the fatigue test. To simulate the temperature increase due to dislocation damping, the temperature at the locally heated zone has been set to 200℃.

2.7 Local Temperature Measurements

An IR camera was used to evaluate the temperature increase at the notch root during the fatigue test. The Quantum Focus Infrascope II implements resistance thermometry to take IR thermal images from the micro- resonator before and during the fatigue test. Figure 2.12 presents a picture of the Quantum Focus Infrascope II infrared

microscope (QFI). Liquid nitrogen is used to keep the temperature of the detector as low as -196 °C to decrease the effect of thermal noise. The maximum spatial resolution provided by this microscope is approximately 2.8 μm, using the 15x objective lens, which is not precise enough to estimate the size of the locally heated zoned due to dislocation damping; still it can be used to validate and track the heat generation at notch root and its resulting temperature gradient along the micro-resonator. The microscope has a temperature sensitivity of 0.1 °C. Higher temperature in the sample could result in more precise measurement of temperature by IR microscope, because its sensitivity is proportional to the number of photons received by the detector. Generally the emissivities of metals are low, and to compensate that, their surfaces are coated with graphite foam to increase the emissivity. This approach is not applicable for our microresonator because of the possibility of malfunction. Instead, to improve the sensitivity of the IR measurements, the microresonator temperature was set to 80°C before the test was run. To evaluate the temperature by IR camera, the setup needs to be calibrated; to do this, an independent temperature sensor (T-type thermocouple) was used on the top of the ceramic package, very close to the microresonator, to confirm the pre-set temperature.

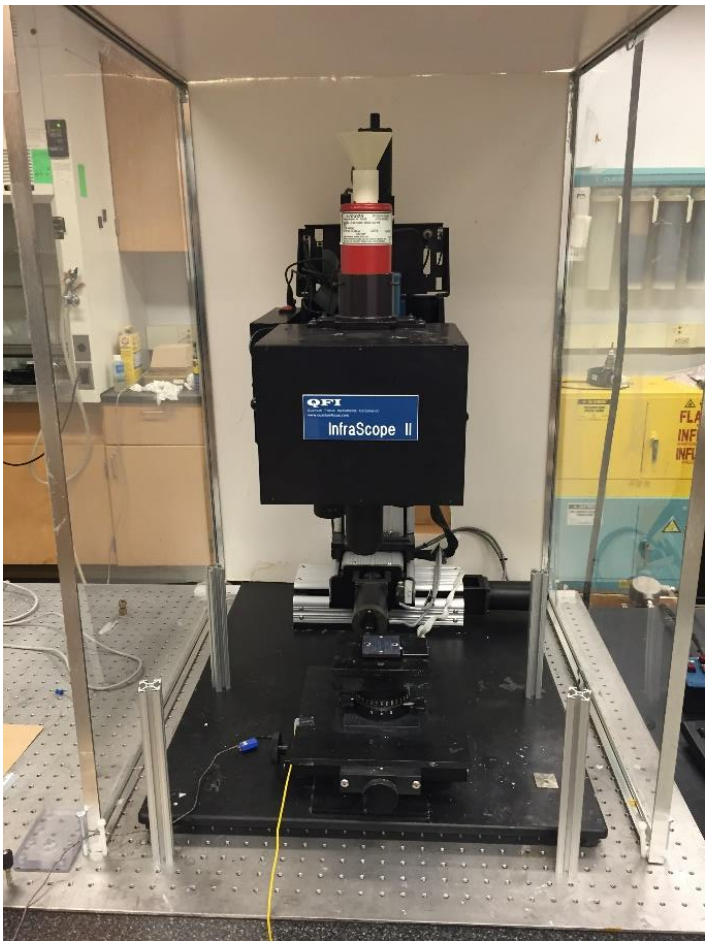

Figure 2.12: Quantum Focus Instruments' Infrascope II infrared microscope with quantum InSb detector which could detect radiation in the 1-5 μm wavelength range.

Figure 2.13 (a, b) shows the initial thermal map from the micro-resonators with stress gradient of 0.36 and 0.17 μm^{-1}, respectively. The fatigue test was then run for two separate series of experiments (0.36 and 0.17 μm^{-1}stress gradients), and thermal maps were captured continuously during the tests (seven measurements were made for each device). Figure 2.13 (c, d) show the thermal maps at the end of the fatigue test for micro-resonators with 0.36 and 0.17 μm^{-1} stress gradients respectively.

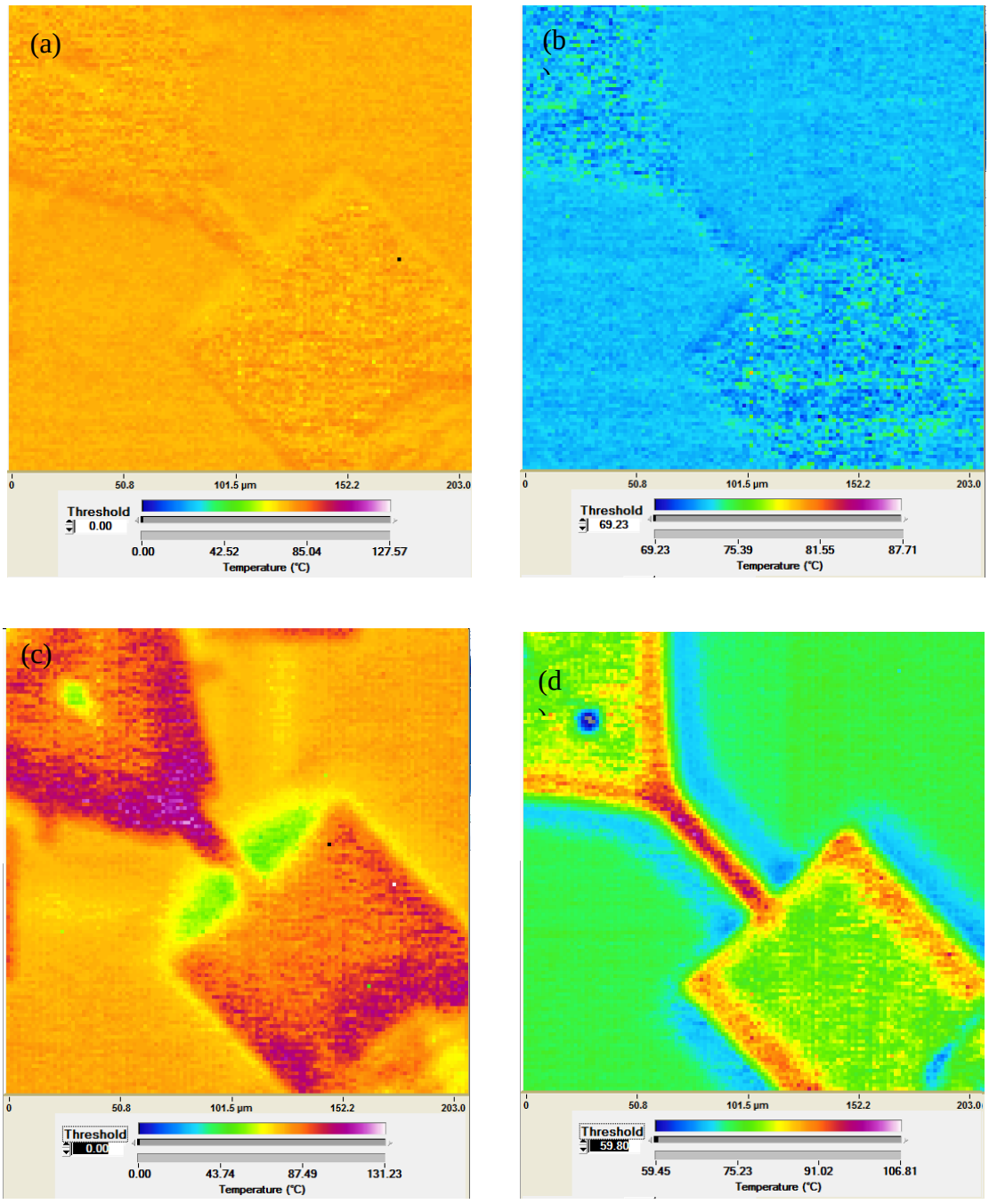

Figure 2.13: Quantum Focus Instruments' Infrascope II infrared microscope temperature mapping. (a, b) Thermal map of the device before the test; for microresonators with 0.36 and 0.17 μm^{-1} stress gradient respectively and (c, d) during the fatigue test; for microresonators with 0.36 and 0.17 μm^{-1} stress gradient respectively.

2.8 Fatigue Damage Observations

2.8.1 SEM Images

In scanning electron microscopy (SEM), when an electron beam strikes the sample, the secondary electrons are emitted from the surface atoms. Emitted secondary electrons detected and post processed to generate interpretable image of the surface. High resolution images obtained by Zeiss Ultra60 FE-SEM used to study and track the changes on notch root's surface morphology during the fatigue test. To do this, fatigue test has been interrupted to take sequential SEM images of the notch root and to investigate the fatigue damage evolution. These images (see Figure 2.14) provide valuable information regarding the location of crack initiation also their propagation trends which will be discussed at chapters 4 and 5.

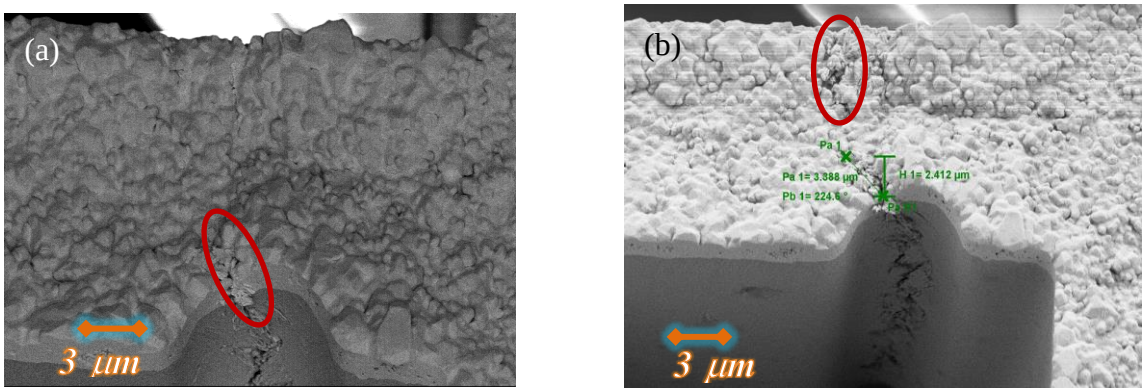

Figure 2.14: (a) The SEM image of top side of beam with highlighted propagated crack (Δf_0=563 Hz). (b) The SEM image of the side wall of notch root with measured crack at notch side and highlighted propagated crack at back side of beam (Δf_0=2034 Hz).

2.8.2 Crack Growth Measurement and FIB Sample Preparation

In an effort to validate the accuracy of the 2D crack propagation assumption in section 2.6.1, the focused ion beam (FIB) milling (Nova Nanolab 200 FIB/SEM) was used to track and measure the formed cracks along the beam ligament during the fatigue test. The Nova Nanolab 200 FIB system uses focused electrons beam and ion beam to take images of the objective. FIB uses a liquid ion metal source (LIMS) to produce a focused beam of gallium (Ga) ions as the emission gun. Due to the high energy and destructive nature of the Ga ions, the FIB is also used for milling processes. When the high energy Ga ions strike the surface of an object, they will sputter atoms off the surface. By adjusting the beam current and voltage we can control the milling parameters. To avoid FIB milling artifacts on the morphology of the formed cracks, this procedure was performed in two steps (rough and fine). We used 30nA and 50Kv for the rough milling process and 5nA and 30Kv for the fine milling process.

2.8.3 EDS Measurements

Energy dispersive X-ray spectroscopy (EDS) measurements were performed on micro-resonators using an EDS analyzer attached to the Zeiss Ulra60 FE-SEM. The interaction of the SEM primary electron beam with surface atoms of the specimen results in shell transitions and consequently leads to an X-ray emission. The emitted X-ray carries the characteristic energy of the surface elements and is used for structural and chemical characterization. The size of the interaction volume increases with accelerating voltage. For this case, 5keV accelerating voltage is used. Energy Dispersive X-ray Spectroscopy or EDS provided qualitative (oxygen/nickel ratio) and

quantitative (oxygen map) analysis of the elemental composition of the first 1-2 microns of the sample's surface. To perform a qualitative analysis, the elemental composition have been normalized by implementing the adequate standards predefined by the EDS analyzer.

2.9 Microstructural Short Crack (MSC) Growth Rate Calculation

The procedure for calculation the crack growth rate for microresonator with 0.36 and 0.17 μm^{-1} is presented in this section. Figure 2.15 (a) shows three representative f_0 evolution curves for η = 0.17 μm^{-1} at σ_a = 305, 355, and 400 MPa. Using the FEM, these curves were transformed into corresponding crack size a vs N plots (see Figure 2.15 (b)). The crack size a should be understood as an equivalent 2D crack size that leads to the same decrease in f_0 as in the actual fatigued micro-beam in which several cracks across the thickness may nucleate separately in adjacent grains.

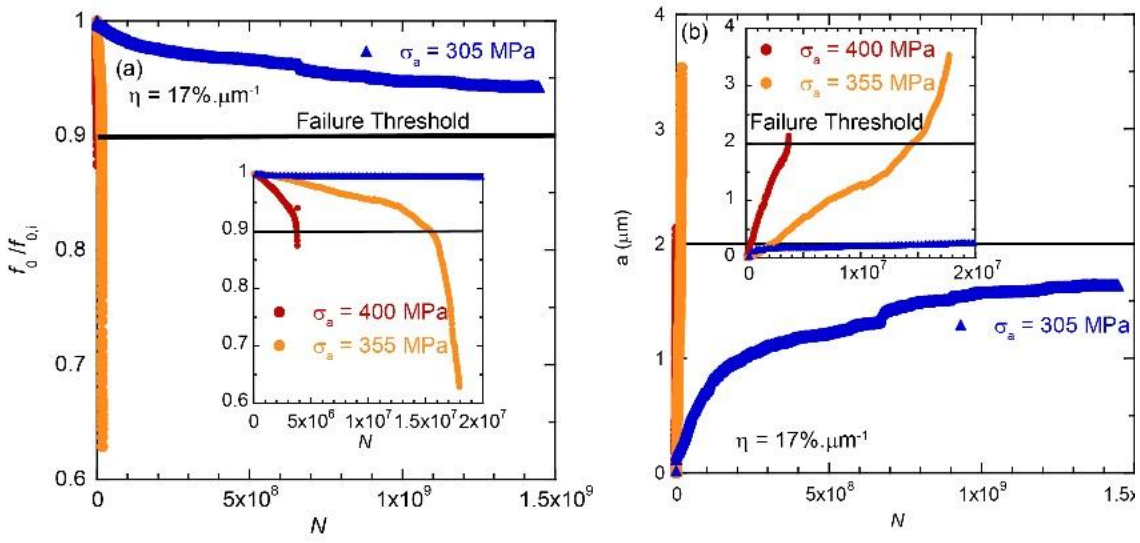

Figure 2.15: (a) Normalized f_0 evolution, $f_0/f_{0,i}$, as a function of cycles for 3 representative specimens (η = 17%.μm^{-1}) tested at 30 °C, 50% RH ($f_{0,i}$ ~ 8600 Hz); (b) corresponding crack size a vs N plots obtained from 2D FEM.

Initially, the crack propagation rates were calculated by using the secant method, whereby the slope between two adjacent points on the calculated "a vs N" curve constitutes the growth rate. The typical interval between two measured f_0 (and therefore 2 calculated "a" values) is 40,000 cycles. Figure 2.16 (a) shows the crack propagation rate curves as a function of calculated a for 3 specimens presented in Figure 2.16 using secant method. For a given curve, the rates are scattered within an order of magnitude, which is likely the result of the secant method amplifying the effect of noise in the measurements (typical precision in f_0 is < 1 Hz). To address this concern, as a second approach, using polynomial fits of successive segments of a vs N curves (from a = 0 to 0.5 μm, 0.5 to 1 μm, etc.), these plots are then transformed into crack growth rates,

d*a*/d*N*, as a function of *a* (see Figure 2.16 (b)) to compute the rates. Figure 2.16 (b) shows that the crack growth tendencies are a strong function of σ_a at notch root.

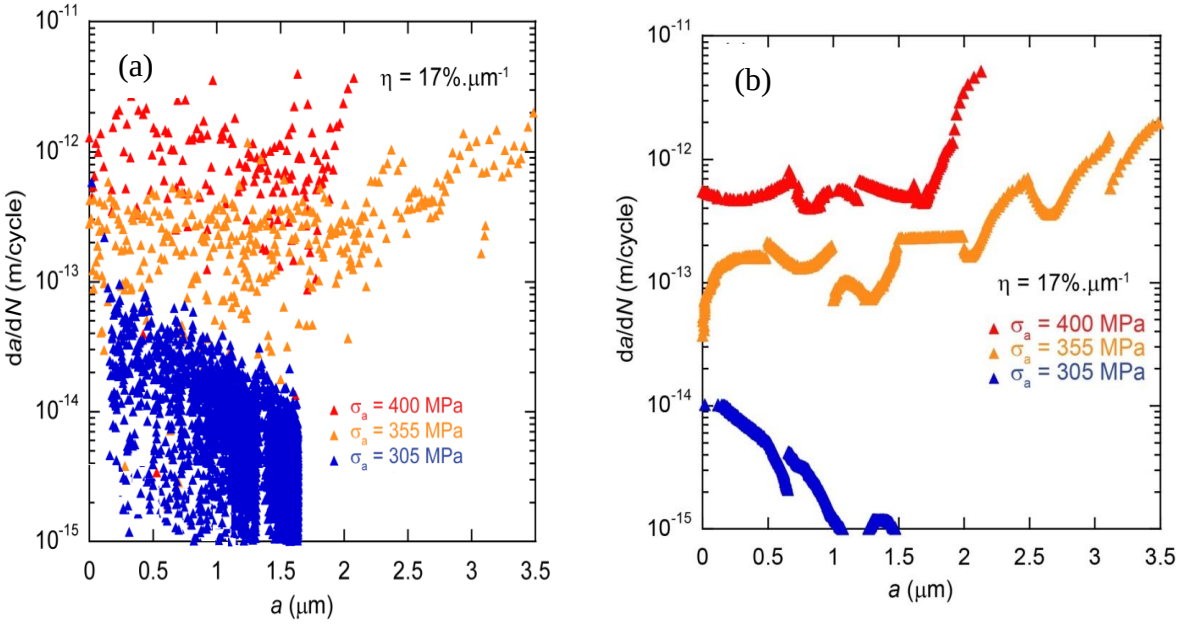

Figure 2.16: Crack propagation rate curves as a function of calculated *a* for 3 specimens (corresponding to the 3 specimens shown in Figure 2.15): (a) Using secant Method; (b) Using polynomial fits of successive segments of *a* vs *N* curves (from *a* = 0 to 0.5 μm, 0.5 to 1 μm, etc.)

CHAPTER 3: MICRORESONATOR CHARACTERIZATION

In this chapter, the dynamic behavior and electrical response of the microresonators was characterized, from which two designs were selected for fatigue testing. The thermal behavior of the two selected microresonators was also characterized.

3.1 Dynamic Behavior Characterization

3.1.1 Resonance Frequency

In this section, the dynamic behavior of the microresonators is characterized. *Table 4* lists the dynamic behavior parameters of the designed microresonators.

Table 4: Predicted resonance frequencies from designed microresonators.

Design #	W_{max} [μm]	W_{min} [μm]	k_θ [N.m/rad]	η [μm^{-1}] ≈	In-plane Bending [Hz]	Out of Plane bending [Hz]	Torsion [Hz]
1	-	-	1.730E-05	0.36	7,820	15,321	14,210
2	10.6	8.3	3.59E-06	0.24	6,242	14,388	13,757
3	16	12.5	1.14E-05	0.16	6,252	9,142	11,498
4	32	25	7.78E-05	0.08	7,279	4,889	7,618

All these data have been extracted by implementing a fully parameterized APDL code; more details regarding the design criteria and the implementation of the Ansys code are presented in chapter 2. The microresonator with 0.36 μm^{-1} stress gradient has been investigated and its resonance frequencies are in excellent agreement with

corresponding FE model (within 5%), which validates the accuracy of the one-degree-of-freedom modal analysis. Subsequently the modeled resonance frequencies of the next series of microresonators (Design # 2, 3, 4) are compared with the corresponding experimentally measured values in this section. Due to the patterning of the photoresist used for the electroplated Ni layer, the actual dimensions differ from the as-drawn ones, and are observed to be slightly larger (for example, the sensing and actuation comb fingers are 1μm wider) in the MetalMUMPs fabrication. Using corresponding SEM images, Figure 3.1 (a, b, and c) illustrates the measured dimensions of the microbeam (W_{max}, W_{min}, and length) for designs, #2, 3, and 4 respectively.

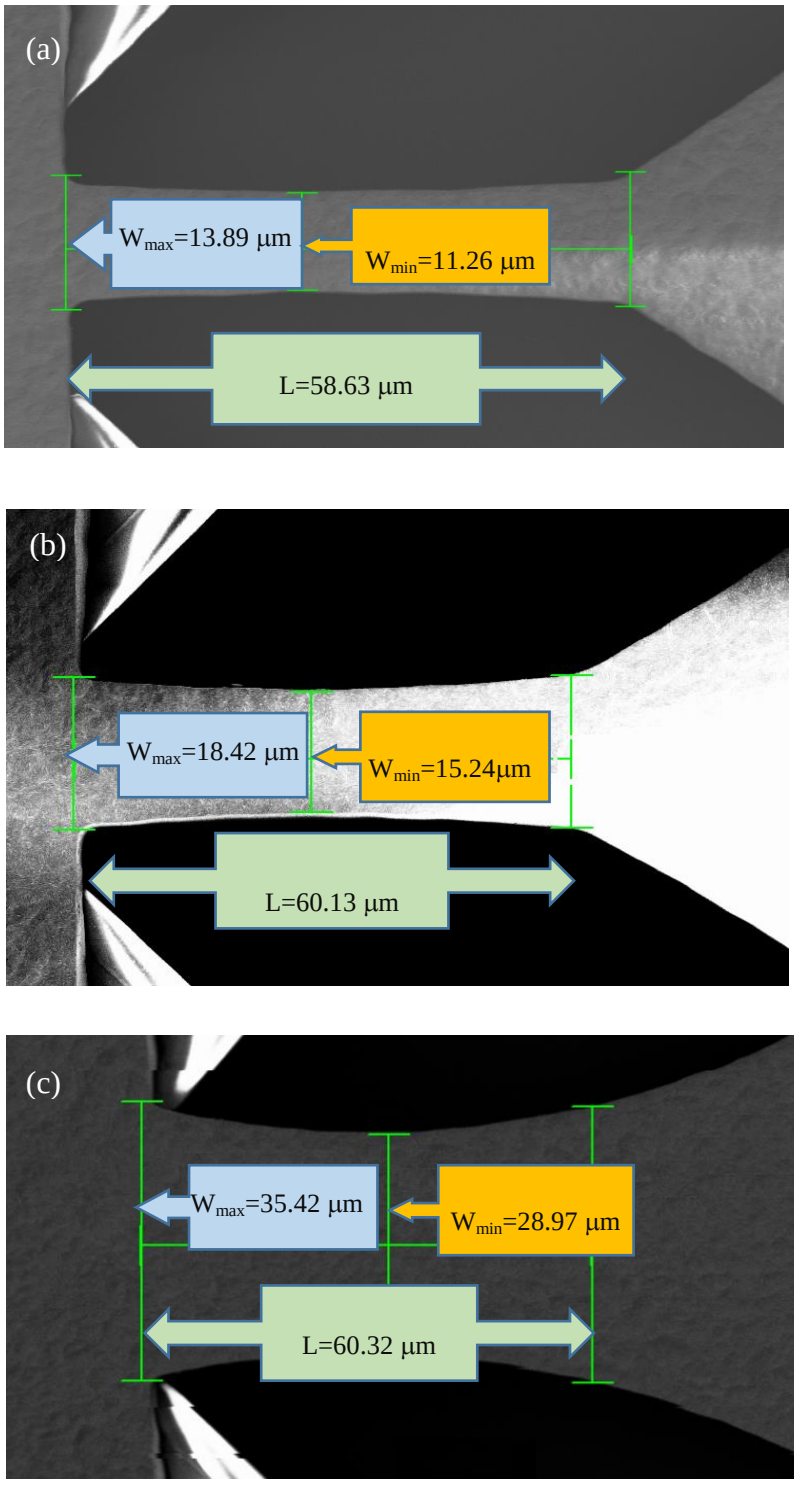

Figure 3.1: Measured dimensions of microresonators by implementing corresponding SEM images. (a) $\eta = 0.17\ \mu m^{-1}$, design#2. (b) $\eta = 0.13\ \mu m^{-1}$, design#3. (c) $\eta = 0.065\ \mu m^{-1}$, design#4.

As shown in this figure, the measured dimensions of the beam do not exactly match with the designed parameters. When the W_{max} and W_{min} values from Figure 3.1 are compared with their corresponding values in the second and third columns of *Table 4*, a difference of about 3 μm is found between designed and fabricated microresonators. As a result, all the dynamic behaviors of the designed microresonators could differ significantly from those of their fabricated versions. To address this concern, the beam dimensions from Figure 3.1 have been extracted and implemented into the Ansys model to compute the corresponding dynamic behavior. The new parameters are listed in *Table 5*. For design #1, there is no W_{max} or W_{min}, and the fabricated microresonator is about 3.5 μm (0.5 %) shorter in length and about 1.5 μm (12%) shorter in beam ligament than the designed version. To compute the resonance frequency, the effect of the top 0.5 μm thick Au layer and the bottom 0.5 μm thick Cu layer has been considered by implementing a 2% reduction in resonance frequency [64].

Table 5: Predicted resonance frequencies of the microresonators by considering the actual dimensions

Design #	W_{max} [μm]	W_{min} [μm]	k_θ [N.m/rad]	η [μm^{-1}] ≈	In-plane Bending f_0 [Hz]	Out of Plane Bending f_0 [Hz]	Torsion [Hz]
1	-	-	1.73E-05	0.36	7820	15015	14160
2	13.89	11.26	9.44E-06	0.17	9125	15478	18957
3	18.42	15.24	2.03E-05	0.13	8083	11424	12587
4	35.42	28.97	1.27E-04	0.06	6843	4898	7985

The parameters of dynamic behavior shown in *Table 5* are used in combination with the experimentally measured resonance frequency of the microresonator in order to investigate the fatigue behavior of a Nickel microbeam under extreme stress gradient. To do this, only the resonance frequency of the first in-plane bending mode was used. It is worth to mention that the modeled resonance frequency listed in *Table 5* is the natural resonance frequency of microresonators. But the developed experimental setup provides the resonance frequency measurement for the forced vibration (resulted from electrical actuation) of the microresonators. Figure 3.2 shows that the measured resonance frequency for different microresonators is a function of actuation voltage, due to the effect of damping. To exclude this effect on the experimentally measured resonance frequency, a second order polynomial is fitted to each series of experimentally measured values to predict the resonance frequency of microresonator for zero actuation voltage (see Figure 3.2).

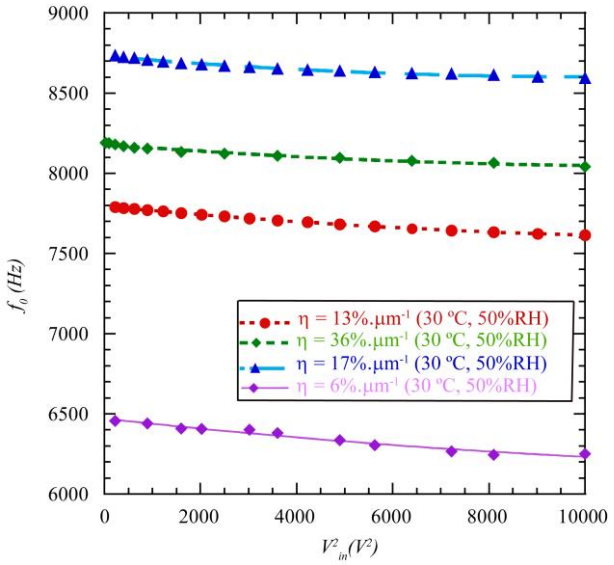

Figure 3.2: Resonance frequency variation for different microresonators as a function of actuation voltage.

The estimated resonance frequency corresponding to zero actuation voltage is considered as the experimentally measured natural resonance frequency for each individual design. As illustrated in Table 6, the modeled resonance frequency (copied from *Table 5*) is different from the corresponding experimentally measured resonance (extracted from Figure 3.2). The percentage of this difference is listed in Table 6 for different designs. These values illustrate a reasonable agreement between the averaged measured resonance frequency and the corresponding modeled resonance frequency; especially by considering the difference between the maximum and minimum values of the experimentally measured resonance frequency for each series of microresonators with same stress gradient (i.e. about 5% discrepancy for design #2).

Table 6: *Modeled* and experimentally measured first in-plane bending frequency mode of microresonators.

Design Number	**k_θ [N.m/rad]**	**η [μm^{-1}] ≈**	**Modeled f_0 [Hz]**	**Measured f_0 [Hz]**	**Difference Between Measured and Modeled Resonance Frequency [%] ≈**
1	1.73E-05	0.36	7820	8181	+4.6
2	9.443E-06	0.17	9125	8730	-4.3
3	2.030E-05	0.13	8083	7795	-3.6
4	1.274E-04	0.06	6843	6470	-5.4

3.1.2 Quality Factor

In this section, the electrical response of the microresonators is characterized to evaluate their potential for studying the fatigue behavior of microbeams under extreme stress gradients. Figure 3.3 represents a typical frequency response of all the designed microresonators for a constant actuation voltage amplitude (V_{in} = 200 V) at room temperature. The first three designs show similar results for response amplitude and response sharpness, which suggests a similar quality factor for these three devices. Nevertheless, for design #4, the corresponding frequency response is very wide, which leads to a low quality factor. Based on optical microscope observation, the motion of the last fingers for this design (blur area) is not large in comparison to the other three designs. But the larger number of fingers for this particular design (40) results in the detection of a significantly higher voltage in the lock-in amplifier. The wide frequency response of design #4 makes it impossible to precisely fit a polynomial to the frequency response in order to keep track of the frequency decrease during a fatigue test. In addition, this wide range of frequency response covers all three vibration modes (in-plane, out-of-plane, and torsion modes, see *Table 5*), and makes it quite challenging first to use the optical microscope to distinguish the in-plane bending from other modes, and second to measure the resonator's angle of rotation during the fatigue test in order to estimate corresponding stress level at notch root. As a result, this series of microresonators was not selected to perform the fatigue tests and will not be characterized further in this chapter.

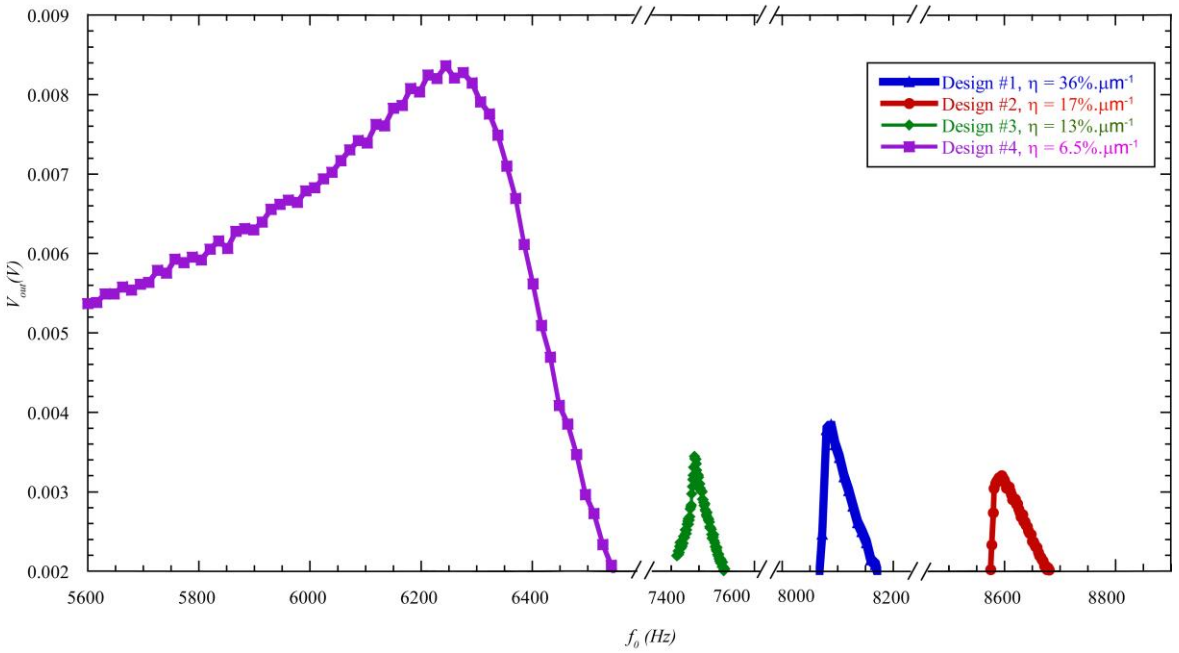

Figure 3.3: A typical frequency response of all the designed microresonators. The amplitude of actuation voltage is 200 Volt.

Figure 3.4 (a) shows the quality factor of the first three designs (just one specimen has been tested for each design) as a function of the square of the actuation voltage's amplitude in air (30 °C, 50% RH). $Q = f_0/\Delta f$, where Δf is the full width at half power, i.e. the width of the range of frequencies for which the energy is at least half its peak value. In a good agreement with Figure 3.3 observation, Figure 3.4 (a) also suggests a similar quality values factor for these designs during the fatigue test. The significant decrease in Q by increasing the actuation voltage is interpreted as resulting from larger plastic deformations at the notch root. As a consequence, the effect of air shear damping is negligible compared to dislocation-based damping [64]. For this reason, the effect of air temperature (different test environment temperature) on quality factor and consequently on the calculation of corresponding stress level at notch root of microresonator has been ignored.

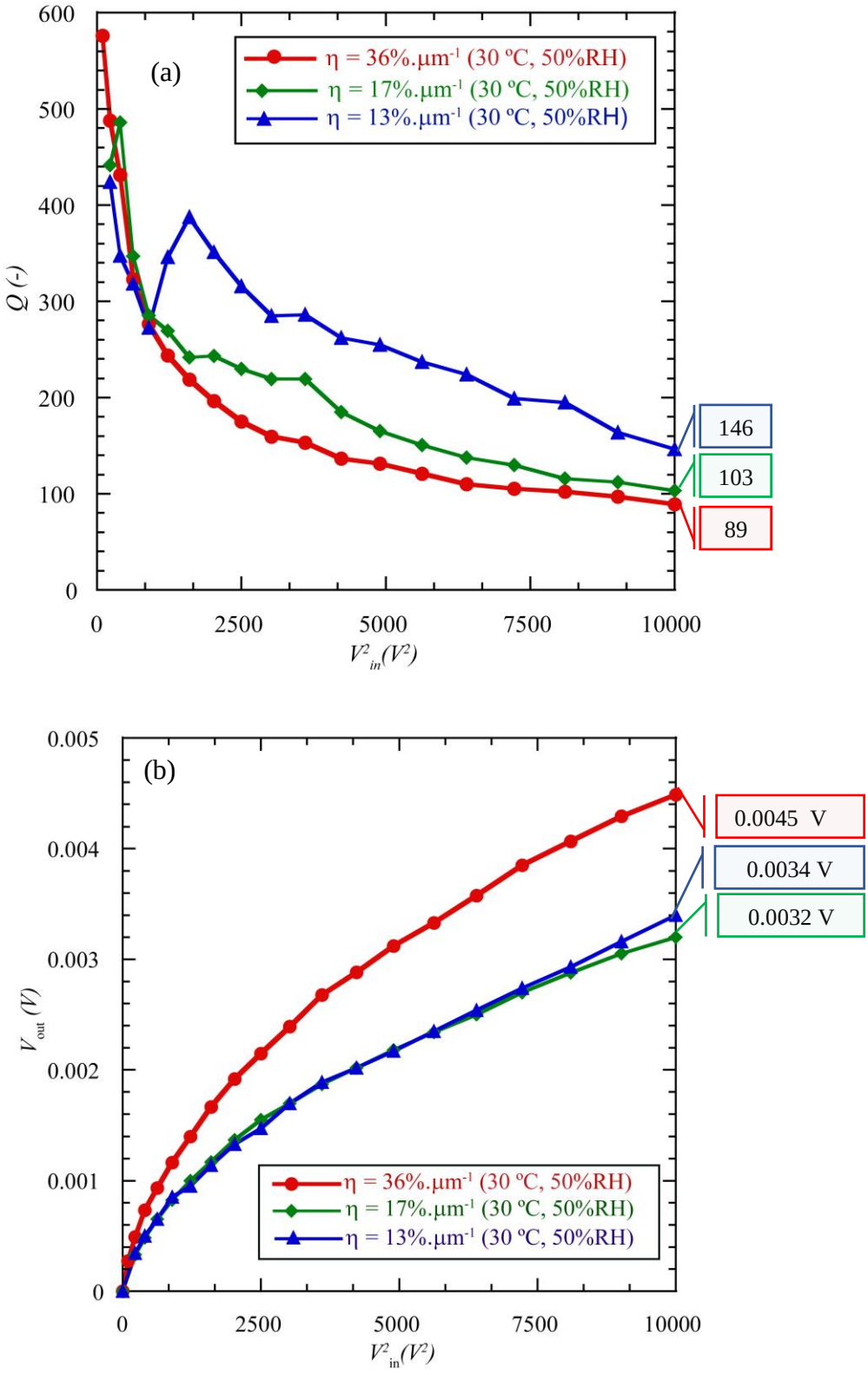

Figure 3.4: (a) Quality factor as a function of V_{in}^2. (b) V_{out} as a function of $V_{in}^{2.}$

Figure 3.4 (b) presents the nonlinear behavior of V_{out} (corresponds to the three specimens presented in Figure 3.4(a)), which is interpreted as a manifestation of plastic deformation at the notch root during the fatigue test; this is reasonable [69] considering the corresponding behavior of the quality factor (see Figure 3.4(a)).

The corresponding ratio V_{out}/Q for the above mentioned microresonators is presented in Figure 3.5 as a function of V_{in}^2. The linear trend confirms that Q is the only parameter responsible for the observed nonlinearities in Figure 3.4 (b), and it confirms that the change in stiffness, k_θ, is negligible for the fatigue tests performed on microresonators. Considering the characterized dynamic behavior in the three recent figures, and since designs # 2 and # 3 provide similar values for the stress gradient (0.17 and 0.13 μm^{-1}), designs #1 and # 2 have been selected for performing the tests to study the stress gradient effect on the fatigue behavior of nickel microbeams. In the next sections, the dynamic behavior of designs #1 and 2 is characterized and discussed in more detail.

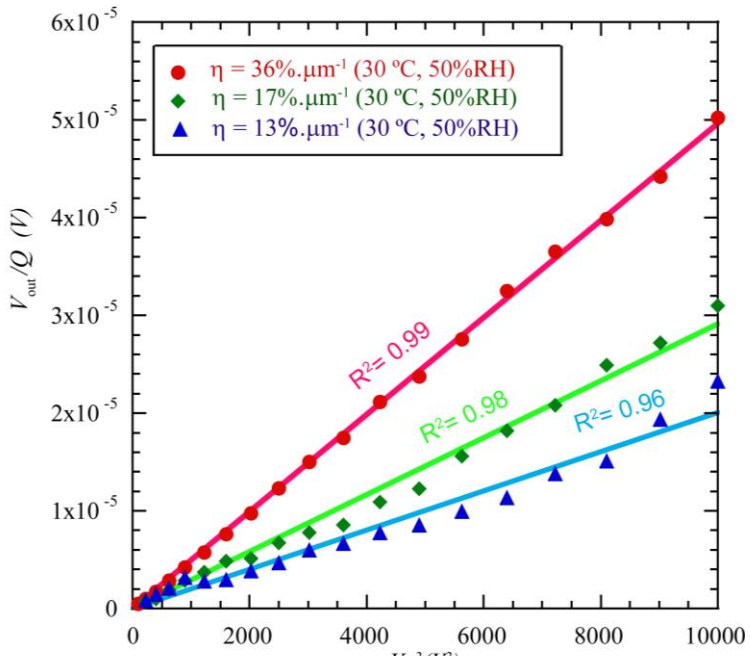

Figure 3.5: The V_{out}/Q ratio as a function of V_{in}^2.

Figure 3.6 shows Quality factor, V_{out}, and their corresponding ratio as a function of actuation voltage (ranging from 0 to 200 V) for a microresonator with 0.17 μm^{-1} stress gradients. This figure highlights that the V_{out}/Q ratio is still linear without the significant change in beam stiffness. This observation is reasonable because these data are based on sweep test for defining the resonance frequency and there is no significant fatigue damage or crack propagation which could potentially changes the beam stiffness.

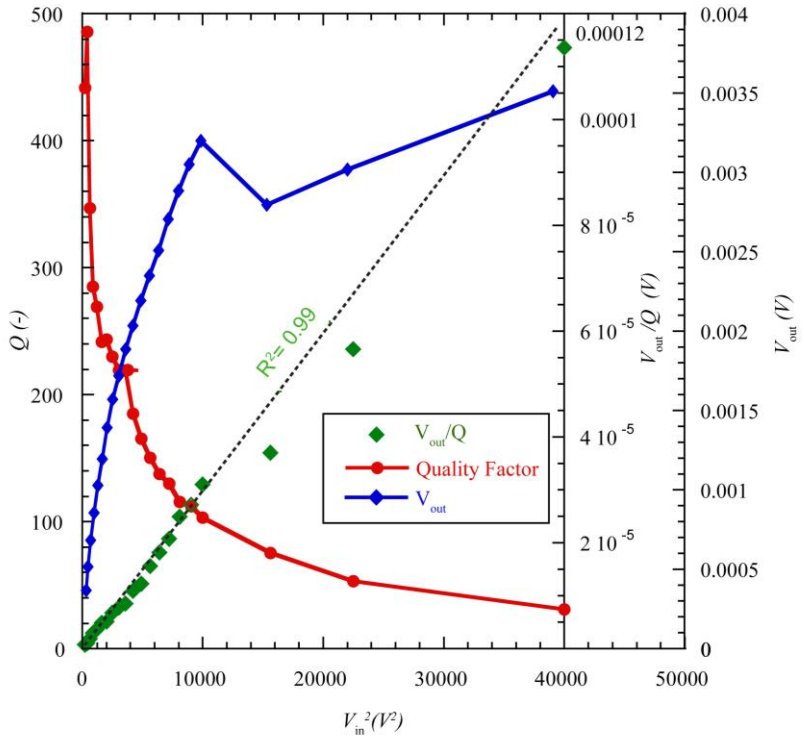

Figure 3.6: Quality factor, V_{out}, V_{out}/Q as a function of actuation voltage (0-200 *V*) for microresonator with 0.17 μm^{-1} stress gradient.

3.1.3 Amplitude Response and Resonance Frequency Evolutions During Fatigue Testing

Figure 3.7 shows the amplitude response development during two fatigue tests of microresonators with 0.36 and 0.17 μm^{-1} stress gradient in a mild environment (30 °C, 50% RH). These microresonators experienced a different number of cycles before failure, mainly because of the effect of stress gradients (see Chapter 5). For microresonator with 0.36 μm^{-1} stress gradient, the fatigue life (N_f) is about 10 times larger than that of the microresonator with 0.17 μm^{-1} stress gradient, despite the fact that the stress amplitude is about 20% higher. The amplitude response development trend is similar for both microresonators: about a 20 % increase in amplitude response during the fatigue test.

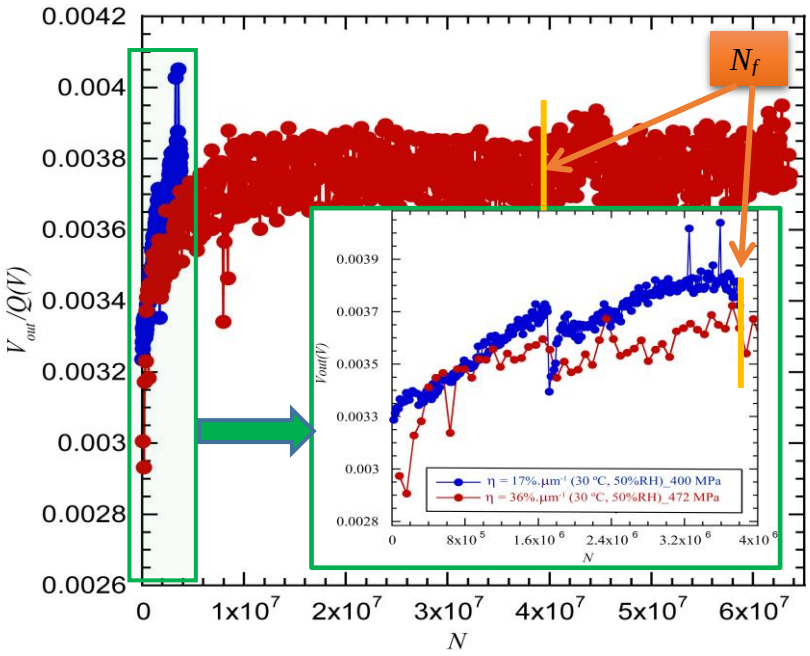

Figure 3.7: Development of amplitude response for microresonators with 0.36 and 0.17 μm^{-1} stress gradient during the fatigue test.

Figure 3.8 presents the normalized frequency response versus the number of cycles, corresponding to the fatigue tests presented in Figure 3.7. Considering the failure threshold (10% decrease in resonance frequency; see rationale below) the microresonators with 0.36 μm^{-1} stress gradient and 470 MPa stress amplitude at notch root failed after $N_f = 4 \times 10^7$ and the test stopped after ($N = 6.5 \times 10^7$) with more than 13% decrease in resonance frequency (about 1029 Hz). Instead, the microresonator with 0.17 μm^{-1} stress gradient and 15% lower stress at the notch root failed after about $N_f = 4 \times 10^6$ cycles and shortly after that (5×10^4 cycles) it stopped with 12% decrease in resonance frequency (about 1083 Hz).

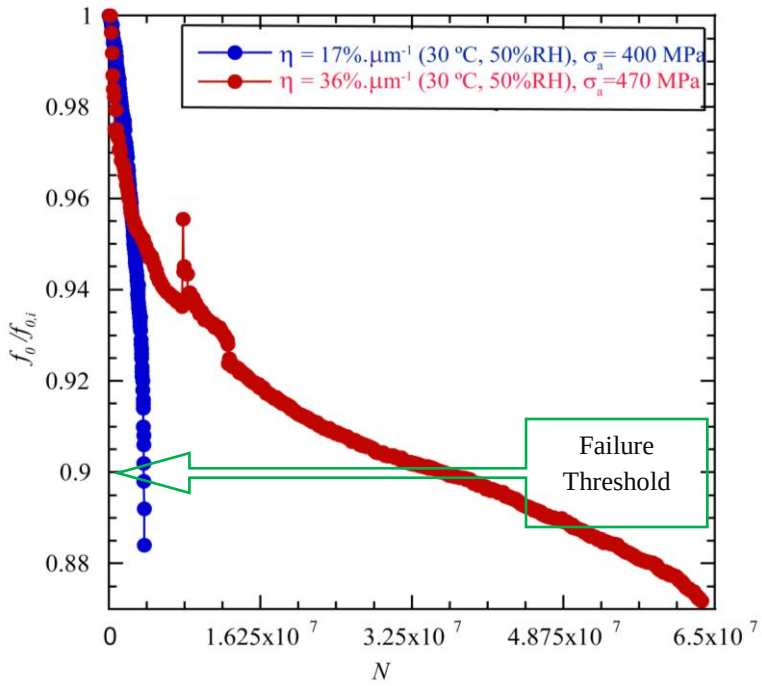

Figure 3.8: Frequency development for microresonators with 0.36 and 0.17 μm^{-1} stress gradient during fatigue test.

For these microresonators, a 10% decrease in resonance frequency (failure criterion) corresponds to a 2 μm-long crack at the notch side (for 0.36 μm^{-1} microresonators) and 2.2 μm-long cracks at both sides of the microbeam (for 0.17 μm^{-1} microresonator). This 10% decrease in f_0 corresponds to a 20% decrease in stiffness, k_θ, which subsequently leads to a 20% increase in measured angle of rotation and corresponding V_{out} (see equation (8)). This predicted trend is in excellent agreement with the results shown in Figure 3.7 (about a 20 % increase in amplitude response during the fatigue test).

The increase ratios in V_{out} have been calculated for the tests performed in both harsh and mild environments for microresonators with 0.36 and 0.17 μm^{-1} stress gradient. These rates are listed in Table 7 and are similar for these two environments

(with an average of 20 % increase). This average has been calculated for failed specimens in different environments which are distinguished from runout specimens by a segregation line in Table 7. These results highlight the fact that the fatigue tests performed with these microresonators are not force-controlled nor displacement-controlled. Instead, the constant driving force M_0 (see eq.(4)) applied throughout the fatigue test results in a gradual increase in stress amplitude (at the microbeam edges) of 20% over the fatigue life. Hereafter, the stress amplitudes associated with each fatigue test correspond to the initial stress amplitude at the beginning of the test (during the optical calibration).

Table 7: Response amplitude increase rate during fatigue tests for the microresonators with 0.36 and 0.17 μm^{-1} stress gradient in both harsh and mild environments. In this table, Inc. Rate is the ratio of V_{out} at N_f cycles over its value at beginning of the fatigue test.

$\eta = 0.36\ \mu m^{-1}$						$\eta = 0.17\ \mu m^{-1}$					
30 °C, 50% RH			*80 °C, 90% RH*			*30 °C, 50% RH*			*80 °C, 90% RH*		
V_{in}	N_f	*Inc. Rate*	V_{in}	N_f	*Inc. Rate*	V_{in}	N_f	*Inc. Rate*	V_{in}	N_f	*Inc. Rate*
400	1.91E+06	1.25	430	6.27E+05	1.15	560	3.77E+05	1.08	560	2.08E+05	1.06
380	4.46E+06	1.94	400	5.95E+05	1.2	500	3.74E+06	1.25	500	9.24E+04	1
360	5.61E+06	1.2	350	7.35E+06	1.19	450	1.98E+06	1.09	450	7.24E+06	1.12
340	8.21E+06	1.23	330	5.98E+07	1.13	400	1.44E+07	1.08	400	1.21E+07	1.2
320	3.58E+07	1.23	320	1.84E+07	1	350	1.54E+07	1.03	350	1.23E+08	1.55
300	6.33E+07	1.11	300	5.47E+07	1.17	330	1.77E+08	1.15	292	1.05E+09	1.45
290	4.33E+08	1.17	290	8.32E+07	1.18	300	2.38E+08	1.45	250	1.66E+08	1.17
280	2.08E+08	1.07	265	1.08E+09	1.19	292	1.45E+09	1.43	225	9.91E+08	1.25
260	6.26E+08	0.88	250	1.11E+08	1.11	280	9.04E+08	1.43	200	1.71E+09	1.07
250	1.49E+09	1.01	225	1.14E+09	1.22	250	3.29E+09	1.3	175	1.23E+09	1.35
225	1.00E+09	1.14	Average		1.15	200	2.72E+09	1.13	Average		1.23
Average		1.14				Average		1.2			

Failed

Runout

3.2 Optical Calibration Results

In the previous chapter the procedure to calculate the angle of rotation (using the optical calibration) and corresponding stress level at notch root was described. Figure 3.9 (a) shows θ_0 vs V_{in} for a series of fatigue tests, comparing both techniques, along with the calibration results from our previous investigations. The accuracy of the old and the new methods have been compared in Figure 3.9 (b), where the corresponding distance between the last fixed finger and the blur area boundary is

measured using both methods. The blue arrow represents measurements used by the new method and the red arrow corresponds to measurements obtained using the old method. This figure shows that new measurement method for such a large displacement (blur area) is more accurate than the previously developed technique (old method). The stress values previously reported [52, 64, 70] should therefore be decreased by ~15-20% to be consistent with the stress values reported here.

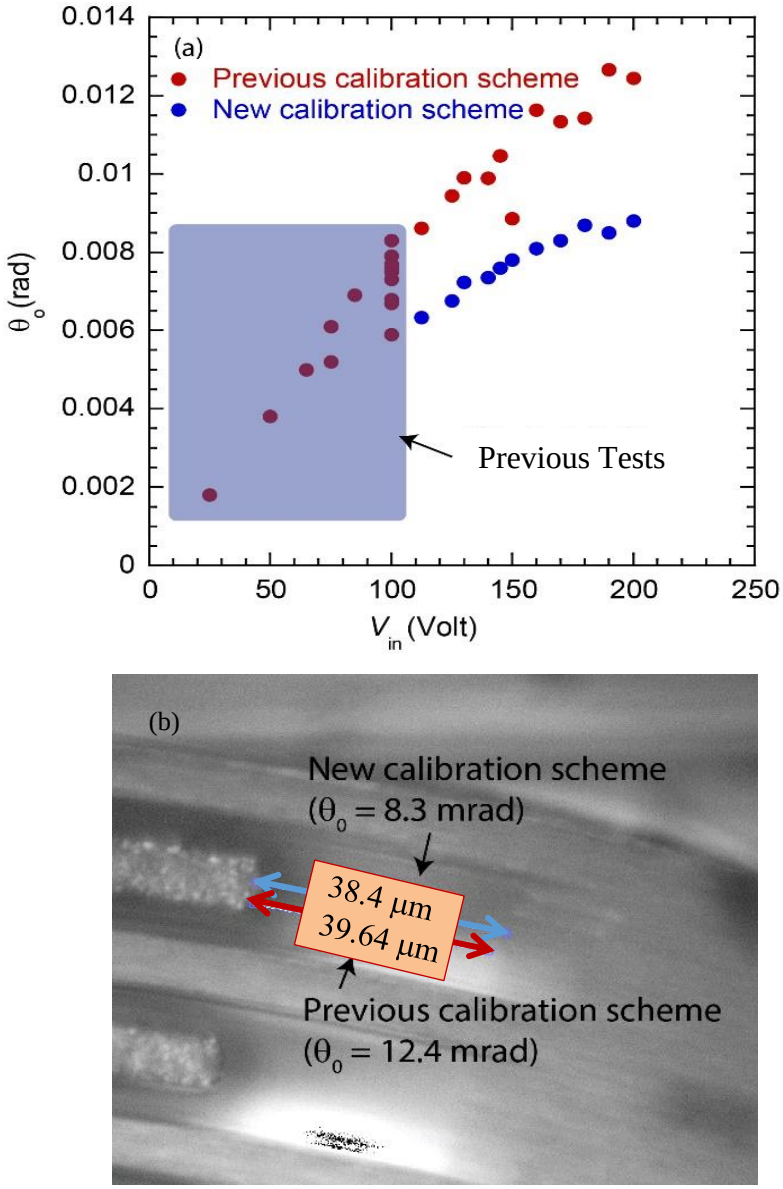

Figure 3.9: (a) Measured angle of rotation at resonance, θ_0, as a function of input voltage amplitude, V_{in}. (b) Optical image used for measurements, comparing results from two calibration schemes.

Figure 3.10 shows the experimentally measured angle of rotation as a function of V_{in} for fatigue tests performed for microresonators with 0.36 and 0.17 μm^{-1} stress gradient (20 and 16 tests of each respectively).

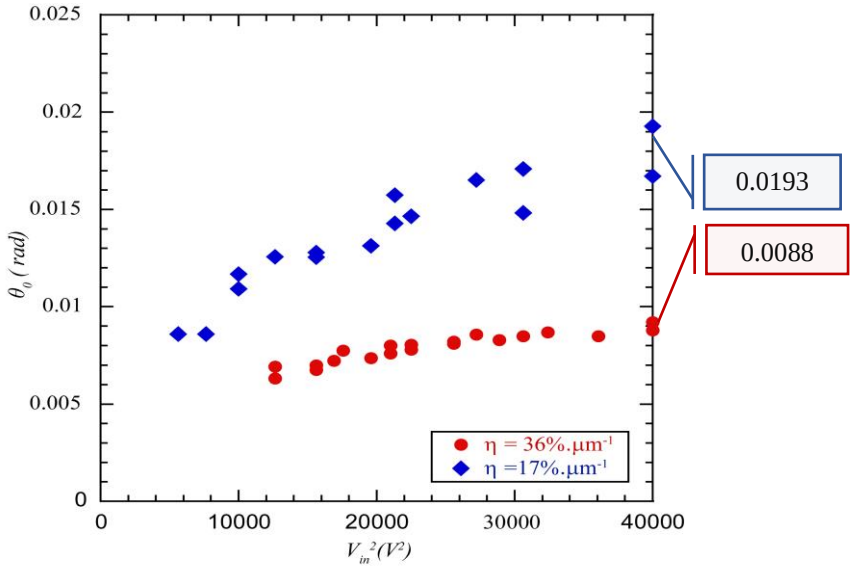

Figure 3.10: Measured angle of rotation, θ_0, as a function of V_{in}^2.

The experimentally measured values for angle of rotation from Figure 3.10 and the predicted values (using equation (6)) have been compared for both microresonators. In Figure 3.11 (a), the angle of rotation has been experimentally obtained for 12 specimens fatigued in air (30C, 50% RH). For the specimen with highest actuation voltage (200 *V*), the corresponding angles of rotation, θ_0, is measured to be 9 mrad. The experimentally measured quality factor is used in combination of equation (6) to compute the predicted angle of rotation and to compare them with the experimentally measured values in Figure 3.11 (a). To do this, the quality factor of one specimen has been measured for 18 sequential increasing voltages (from 20 to 100 *V*) and following that for higher voltages, 7 different specimens have been used to extract the corresponding quality factor and to measure the modeled angle of rotation. Figure 3.11 (a) shows excellent agreement between measured and calculated angle of rotation for the microresonator with 0.36 μm^{-1} stress gradient. For the microresonator

with 0.17 μm^{-1} stress gradient, Figure 3.11 (b) also shows an agreement between 22 experimentally measured angle of rotation (corresponds to the tests performed on one microresonator under sequentially increasing actuation voltages) and , 20 corresponding modeled angle of rotations.

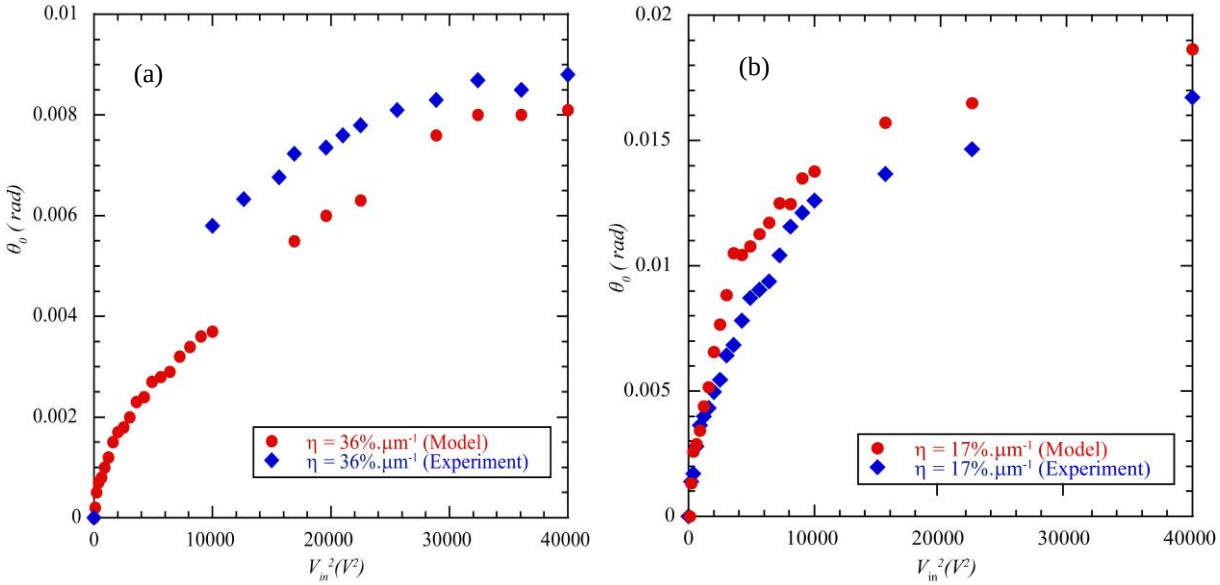

Figure 3.11: Experimentally measured and corresponding modeled values of angle of rotation for microresonators with (a) $\eta = 0.36\ \mu m^{-1}$ and (b) $\eta = 0.17\ \mu m^{-1}$.

3.3 Temperature Increase During Fatigue Testing

3.3.1 IR Camera Measurements

As shown in Chapter 2, an IR camera was used to evaluate the temperature increase at the notch root during a fatigue test. In this section, the temperature increase amplitude and its corresponding increase rate are characterized for microresonators with 0.36 and 0.17 μm^{-1} stress gradient. The results of this section in combination with FEM results from next section will be used to evaluate and discus the strong dependency of temperature increase to the corresponding stress level at notch root for both series of

microresonators (0.36 and 0.17 μm^{-1} stress gradients). These results confirm that the temperature increase effect due to dislocation-damping effect can be ignored for the lower range of stress (σ_a < 380 MPa) which was assumed at previous investigations by Baumert *et al.* [64].

Figure 3.12 shows the temperature increase, and its corresponding increase rate is significantly higher for the microresonator with 0.36 μm^{-1} stress gradient at σ_a = 470 MPa in comparison to that of the microresonator with 0.17 μm^{-1} stress gradient test at σ_a = 370 MPa. Figure 3.12 shows the IR camera images of beam section for both microresonators at beginning and end of fatigue test attached to corresponding data point at ΔT versus time plot.

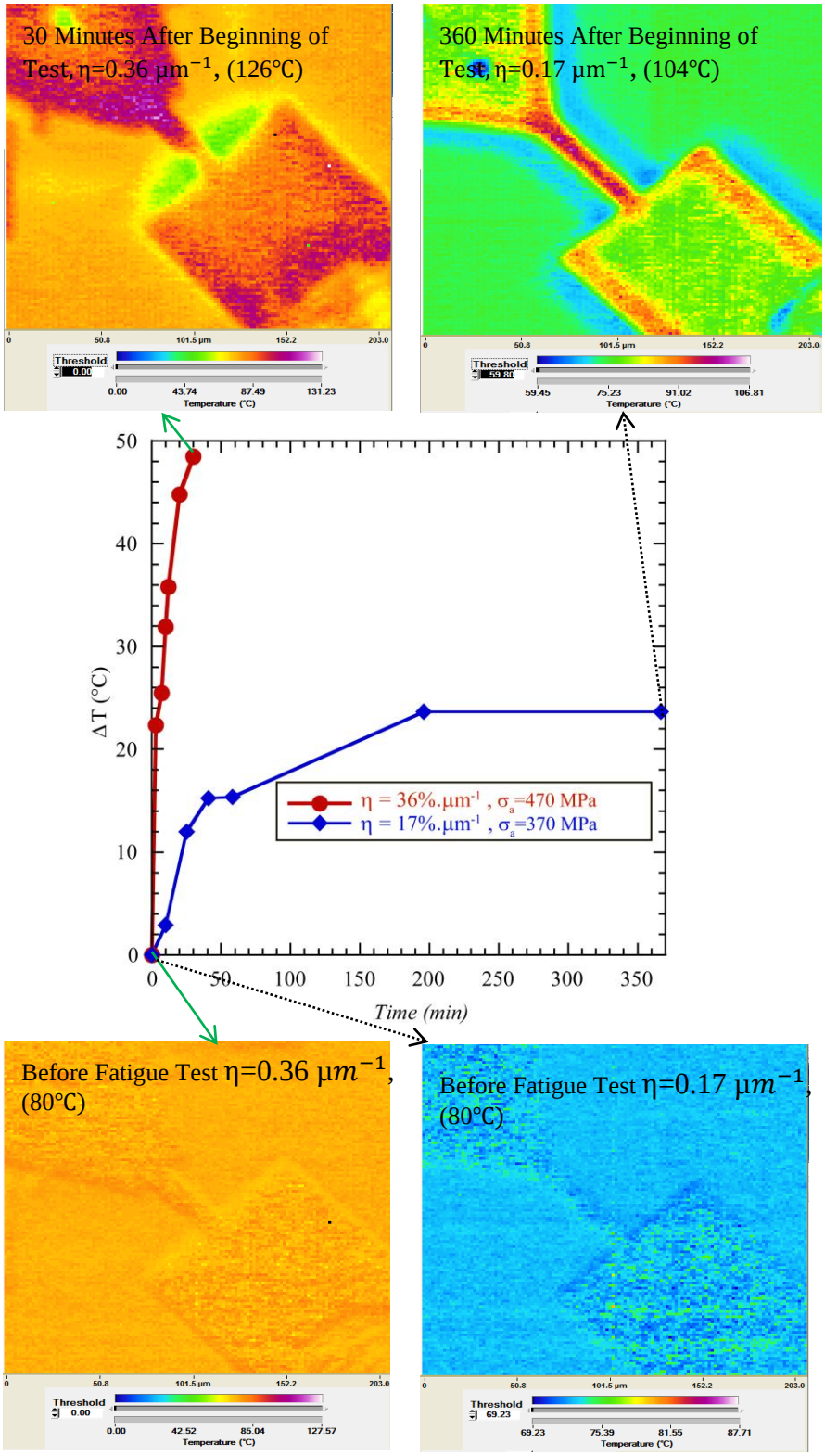

Figure 3.12: Temperature increase during the fatigue tests of two microresonators performed in laboratory air on a hot plate at 80°C.

3.3.2 Finite Element Analysis Results

In this section, the result of steady state thermal model is presented to show the temperature distribution along the beam ligament assuming a local heat zone. Based on IR camera observations presented in previous section, we know that local temperature at the notch root of the micro-resonator will not exceed 200℃ during a fatigue test. To simulate the temperature increase due to dislocation damping, the temperature at the local heat zone has been set to 200℃. Figure 3.13 illustrates the modeled micro-resonator temperature map ranging from 200℃ at the notch root (red contour) to 104℃ (green contour) at the other side of the ligament. The temperature gradient map shows that more than 90% of beam ligament around the notch root (highlighted in a red box in figure below) experiences the same temperature (123± 10°C).This result is consistent with the IR images (see Figure 3.12) showing a fairly uniform temperature distribution across the microbeam during fatigue testing. From these results, we can assume a uniform temperature distribution to predict the reversible decreases in f_0 due to heating (see next section).

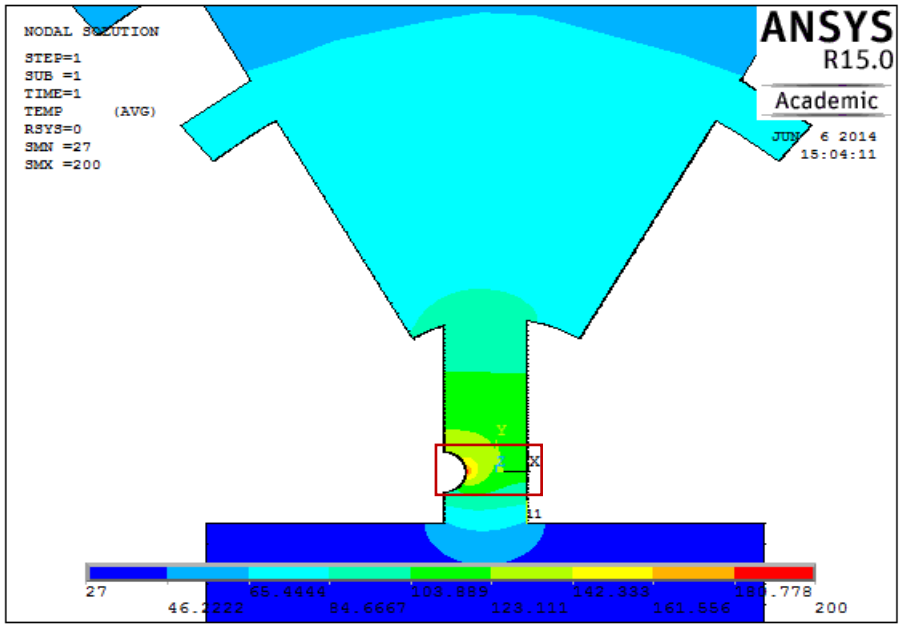

Figure 3.13: Temperature map results form a steady-state thermal analysis by simulating the dislocation damping effect.

3.3.3 Prediction of Local Temperature Increase and Associated Resonant Frequency Decrease

The reversible portion of the decrease in f_0 during a fatigue test is small compared to the irreversible portion (see Figure 3.14). But since it is strongly depends and varies with corresponding stress level at notch root, we need to exclude the temperature-increase effect from frequency evolution to have a consistent comparison of fatigue life of different microresonators and different levels of applied stress at notch root. This section shows how the decrease in resonance frequency due to temperature increase at the notch root during a fatigue test is evaluated. Figure 3.14 shows the f_0 evolution curve for a fatigue test of microresonator with 0.36 μm^{-1} stress gradient (σ_a = 440 MPa, $\varepsilon_{pa} = 4\times10^{-4}$) that was interrupted at 1.9×10^8 cycles for SEM inspection (end of Test 1) and resumed after ~48 hours (beginning of Test 2). Upon interruption of the

test, a sudden increase in f_0 is observed (~120 Hz in Figure 3.14), and upon resuming the fatigue test, f_0 returns quickly to the value seen prior to interruption of the test. This reversible portion of the decrease in f_0 is interpreted as heating of the microbeam, most likely due to dislocation damping (cyclic plastic deformation at high frequency), which is consistent with the temperature increase observed with the IR camera (see Figure 3.12). For microresonator with 0.17 μm^{-1} stress gradient, there is no significant increase in resonance frequency upon interrupting the fatigue test. This observation is also consistent with corresponding IR camera images in Figure 3.12. Low increase in notch temperature, ~20 ºC, of microresonator with 0.17 μm^{-1} suggests that temperature-induced decrease in resonance frequency is negligible for this series of microresonators. In the next section, more details will be provided to support the argument associated with this assumption.

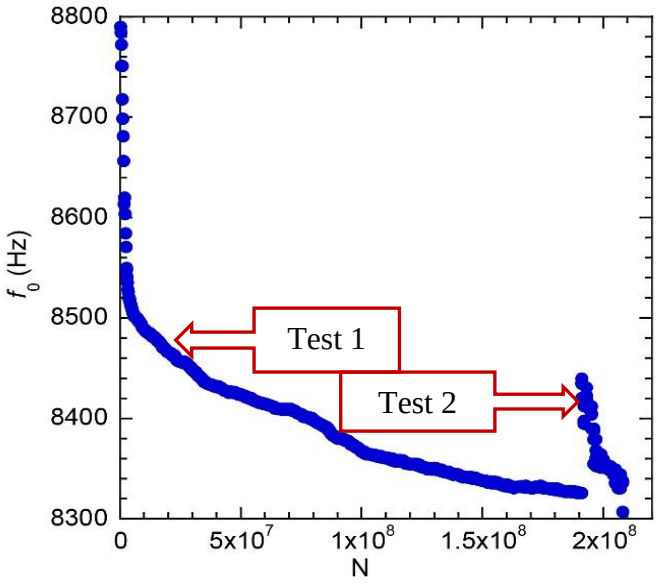

Figure 3.14: Measured f_0 evolution of microresonator with 0.36 μm^{-1} stress gradient for a test interrupted at 1.9×10^8 cycles and resumed after ~48 hours.

In order to quantify only the amount of fatigue degradation (associated with the irreversible portion) of microresonators with 0.36 μm^{-1} stress gradient, the temperature-induced-frequency-decrease needs to be excluded from the frequency evolution. To do this, the increase in resonance frequency after fatigue test interruption has been recorded for 12 specimens with a wide range of stress level at notch root (390 to 520 MPa). These experimentally measured Δf_0 has been used to estimate corresponding ΔT at notch root using $1/E \times (dE/dT)$ = -208 ppm/ ºC. This equation was reported by Baumert *et al.* [64] after characterizing the temperature effect on microresonators response which is consistent with reported T effect on young modulus based of bulk properties of Ni. The estimated ΔT corresponds to experimentally measured Δf_0 upon interruption of fatigue test has been plotted as a function of σ_a in Figure 3.15 which are ranging from 0 (negligible heating) at σ_a = 370 MPa to 120 ºC at σ_a = 500 MPa. The linear fit of estimated ΔT values in this figure has been used to predict the temperature increase due to dislocation damping for all fatigued microresonator with 0.36 μm^{-1} stress gradient. The predicted trend by this line is in a reasonable agreement with experimentally measured value by IR camera (see Figure 3.15).

Although Figure 3.15 is used to predict the temperature increase for microresonators with 0.36 μm^{-1} stress gradient, but considering the fact that the notch temperature directly depends on stress level at notch root, this figure could be used sufficiently to predict the local temperature increase for microresonators 0.17μm^{-1} too. For example, this figure predicts ΔT=15 ℃ for a specimen with 0.17 μm^{-1} stress

gradient at 370 MPa which is consistent with corresponding IR camera measurement, ~ 20 ℃ (see Figure 3.12).

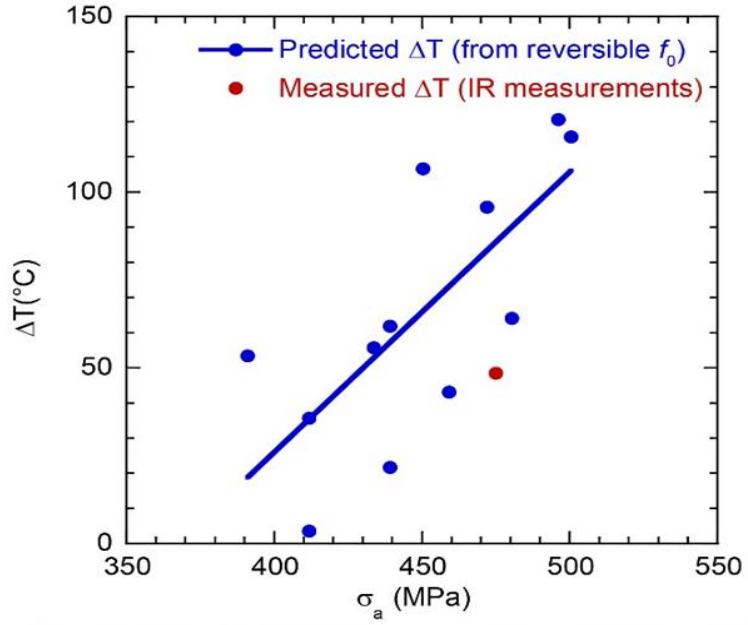

Figure 3.15: Localized temperature increase, ΔT, as a function of σ_a.

The predicted ΔT as a function of σ_a trend in Figure 3.15 , has been transferred into the predicted Δf_0 as a function of σ_a and presented as the predicted temperature trend in Figure 3.16 (the green line). This trend has been used to distinguish between the temperature-induced (reversible) and fatigue-damage-induced (irreversible) decrease in resonance frequency. Figure 3.16 shows the normalized maximum decrease in f_0 as a function of stress for the performed tests in both mild and harsh environments. In this figure Δf_0 is a fatigue-damage-induced decrease in f_0; it excludes the values of Δf_0 that are estimated to be due to temperature effects at the notch root. Indeed, the experimentally measured decrease in resonance frequency corresponds to the summation of the fatigue-induced damage ($\Delta f_{0,1}$) and $\Delta f_{0,2}$ because of the temperature

increase at the notch root. Circular and triangular data points are representative of experimental data for fatigue tests in mild and harsh environments, respectively.

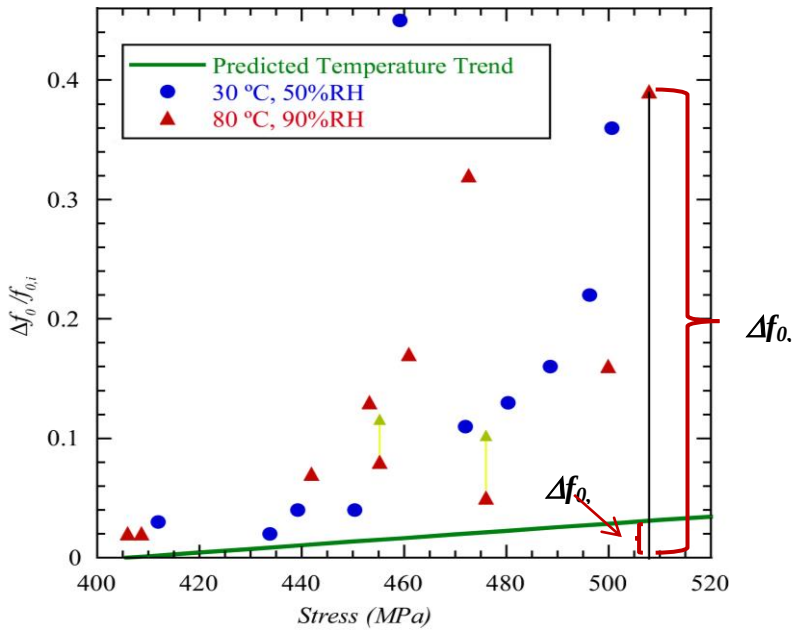

Figure 3.16: Normalized maximum decrease in f_0, $\Delta f_0 / f_0$, as a function of stress in mild (30ºC, 50% RH) and harsh (80ºC, 90% RH) environments. The green line is the predicted- temperature-effect and the yellow square markers represent early interrupted tests.

This figure suggests that for a stress level below 400 MPa there is no decrease in resonance frequency because of the temperature increase at the notch root. Considering the maximum stress level at notch root (about 400 MPa) for microresonator with 0.17 μm^{-1} stress gradient, the temperature–induced frequency decrease should be negligible. This prediction is in a good agreement with frequency development of microresonators with 0.17 μm^{-1} stress gradient in which there is no significant increase in resonance frequency upon instructing the test.

CHAPTER 4: FATIGUE BEHAVIOR OF NI MICROBEAMS WITH η = 36%. μm^{-1}

4.1 Resonance Frequency Evolution

In this section, the results of fatigue tests performed for the microresonators with η=0.36 μm^{-1} at 30ºC, 50% RH and 80ºC, 90% RH environments are presented. Figure 4.1 (a, b) show representative f_0 evolution curves for 4 specimens tested at 30ºC, 50% RH and 80ºC, 90% RH, respectively, in the form of the normalized decrease in f_0 as a function of cycles. Unlike previous investigations at low stress amplitudes (σ_a < 380 MPa, $\varepsilon_{pa} < 10^{-4}$), where the total decrease in f_0 was less than 1% after billions of cycles [41, 42, 71], much larger decreases in f_0 are observed (up to 40%), which are indicative of larger amounts of fatigue damage at the notch root (see section 4.2). The amounts and rates of decrease in f_0 are clearly correlated to σ_a: for example, a slow decrease totaling 2% over 10^9 cycles was observed for σ_a = 390 MPa, while it took only ~6×10^6 cycles to lose 40% of the initial f_0 at σ_a = 500 MPa (see Figure 4.1 (a)). At 80ºC, 90% RH, f_0 is observed to increase for most tests performed at σ_a between 400 and 450 MPa, after an initial decrease over the first ~2×10^8 cycles. The increase is much larger than those found in the previous study at lower σ_a, with as much as a 150 Hz increase (~2% of f_0) for σ_a = 440 MPa (see Figure 4.1 (b)). This increase was attributed to a larger amount of oxidation at the notch root at 80ºC, 90% RH compared to that found at 30ºC, 50% RH, suggesting that here as well there is a significant amount of oxidation at the notch root.

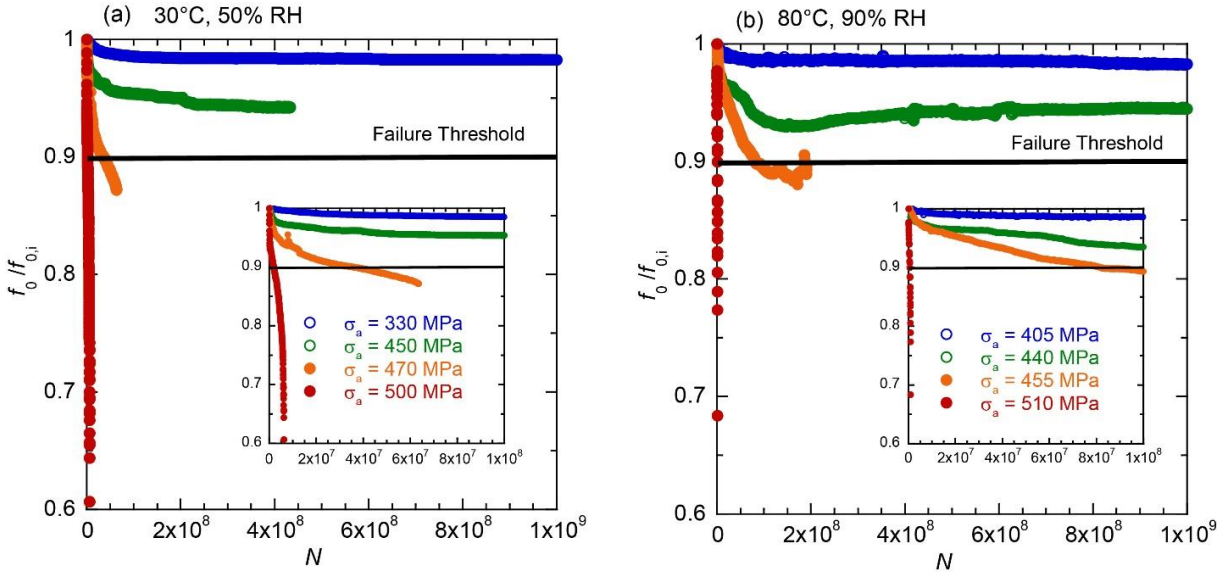

Figure 4.1: Normalized f_0 evolution, $f_0/f_{0,i}$, as a function of cycles for three representative specimens tested at (a) 30ºC, 50% RH and (b) 80ºC, 90% RH.

Figure 4.2 (a, b) shows the total irreversible normalized decrease in f_0 as afunction of σ_a and N_f, respectively, for all fatigue tests (11 at 30ºC, 50% RH and 10 at 80ºC, 90% RH). No significant difference can be observed between the two environments. It should be noted that none of the microbeams are fractured in 2 pieces at the end of the tests; therefore, the total decrease depends on when the test was interrupted. The fatigue life, N_f, was defined as the number of cycles to reach an irreversible decrease in f_0 of 10% of the initial value. This number was chosen because it corresponds to a 2D crack of 2 μm at the notch root (see section 2.6.1). Hence, all specimens shown in Figure 4.2 (a, b) with a total decrease less than 10% are considered as runouts.

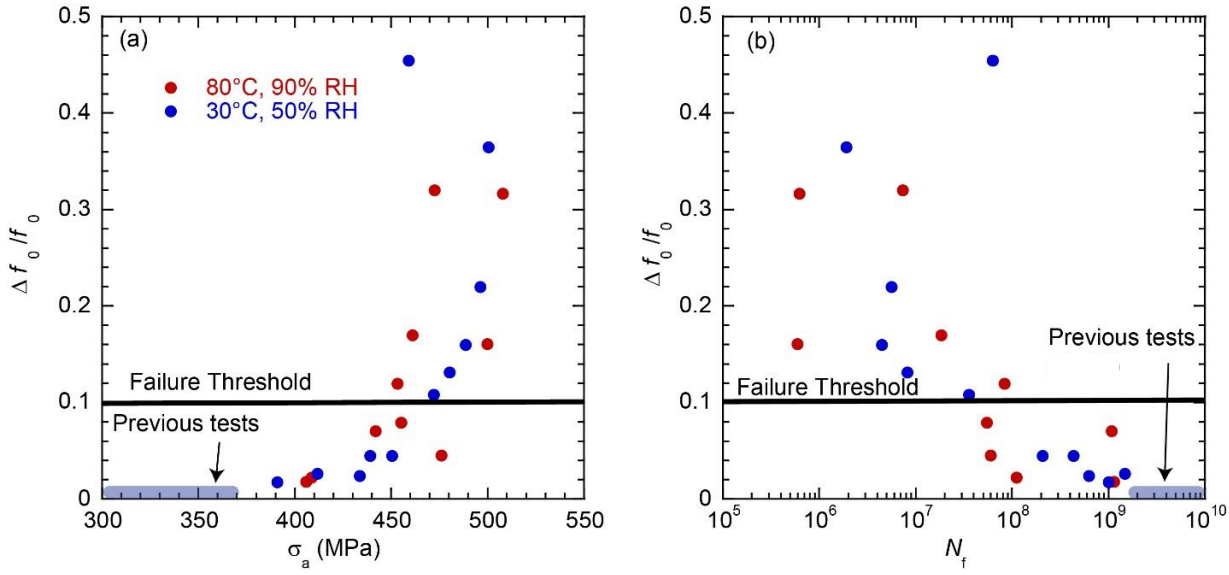

Figure 4.2: Normalized decrease in f_0, $\Delta f_0/f_0$, as a function of (a) σ_a and (b) N_f.

4.2 SEM Observations and EDS Results

Figure 4.3 and Figure 4.5 show representative SEM images of the fatigue damage at the notch root for various σ_a values (ranging from 435 to 500 MPa), numbers of applied cycles, and the corresponding normalized decreases in f_0, for fatigue tests performed at 30ºC, 50% RH and 80ºC, 90% RH, respectively.

In contrast to our previous investigation at lower σ_a values (< 380 MPa, using the new calibration technique discussed in section 2.5.2) where, in most cases, only a few extrusions formed after billions of cycles, with arrested microcracks along their edges [41, 42, 71], these SEM images show more widespread fatigue damage at the notch root as well as at the back side. Specifically, extrusions are present across the entire thickness of the Ni microbeams at the notch root, along with cracks meandering through these extrusions. The zig-zag pattern of the cracks along the microbeam's thickness suggests that these are 3D stage I cracks (crystallographic cracks) forming at

the edges of each extrusion (see high magnification SEM images in Figure 4.3 (b or j) for example), that eventually link up to form a "2D" crack. Figure 4.3 (f-g) and (h-i) show SEM images of the notch root sidewall and top surface (consisting of a 0.5-μm-thick Au layer on top of the 20-μm-thick Ni films) of a specimen tested at σ_a = 480 MPa, for two different numbers of cycles (and corresponding $\Delta f_0/f_0$), respectively. After $N = 5.4\times10^6$ cycles ($\Delta f_0/f_0$ = 6.5%), a "2D" crack is present along the notch root (Figure 4.3 (g)), and can be also observed at the top surface in the Au layer (Figure 4.3 (f)). No surface damage was observed on the back side of the beam, at the top surface (see Figure 4.3 (f)). Instead, after $N = 1.2\times10^7$ cycles ($\Delta f_0/f_0$ = 13%), a large crack is present on the back side, while only a small amount of crack extension was observed at the notch side (from the top surface SEM image, Figure 4.3 (i)). Hence, the large $\Delta f_0/f_0$ values (>10%) result from fatigue damage at both sides of the beams. Here, we only focus on the growth of the fatigue cracks on the notch side, which form first due to the larger stresses. We estimate that the first 10% decrease in $\Delta f_0/f_0$ is mainly associated with the growth of the notch fatigue cracks, based on the observation of fatigue damage at the back side. For example, very little damage is present on the back side in Figure 4.3 (e) ($\Delta f_0/f_0$ = 4%).

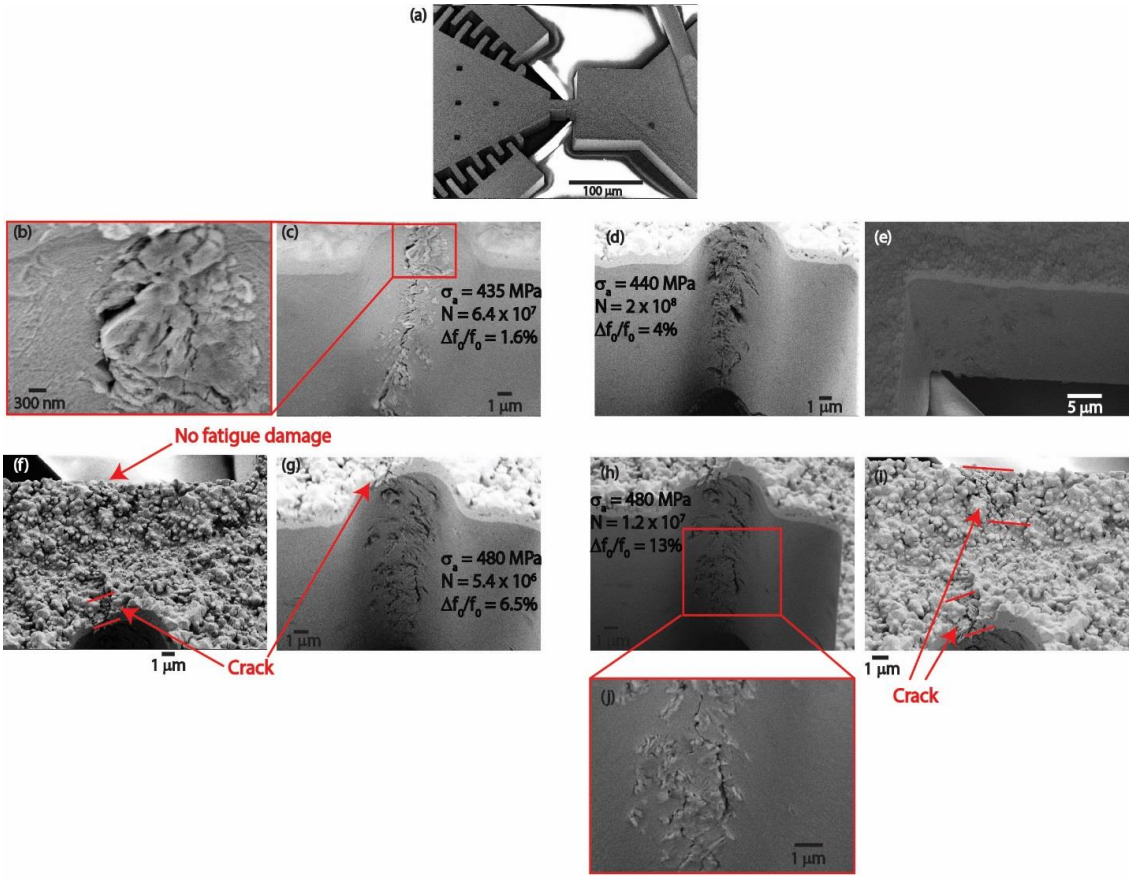

Figure 4.3: SEM images of the notched microbeams sidewalls and top surface after fatigue testing at 30ºC, 50% RH. (a) low-magnification image. (b) and (c) high magnification images of the sidewall after 6.4×10^7 cycles at σ_a = 435 MPa. (d) and (e) sidewall (notch side and back-side, respectively) after 2×10^8 cycles at σ_a = 440 MPa. (f) and (g) top surface and sidewall, respectively, after 5.4×10^6 cycles at σ_a = 435 MPa. (h) and (i) top surface and sidewall, respectively, after 1.2×10^7 cycles at σ_a = 435 MPa (same specimen as (f) and (g) images). (j) high-magnification image of crack along sidewall.

To confirm this, Figure 4.4 shows SEM images of the top surface (with blue line border) and notch root (with red line border) of four additional fatigue tests at 30ºC, 50% RH with stress level ranging from 435 to 500 MPa in the mild environment. These

tests were interrupted at different timing (from 3 $\times 10^5$ to 6.47 $\times 10^7$cycles) during the fatigue test (for SEM imaging) and resumed after about ~72 hours. This interruption is highlighted as Test 1 and 2 in Figure 4.4. Upon resuming the fatigue testing at the same V_{in}, the decrease in resonance frequency continues as a result of further fatigue damage accumulation at notch root. Depending on the applied stress level, the corresponding fatigue life ranges from 6.5×10^6 to 6.5 $\times 10^8$cycles. Comparing these four sets of sequential SEM images shows that the first fatigue crack initiated at the notch root and propagated until a certain length (about 2 μm, see Figure 4.4 (a, e, i, and m)). Then a secondary crack initiated and propagated at the backside of the beam, Figure 4.4 (g, k, and o).

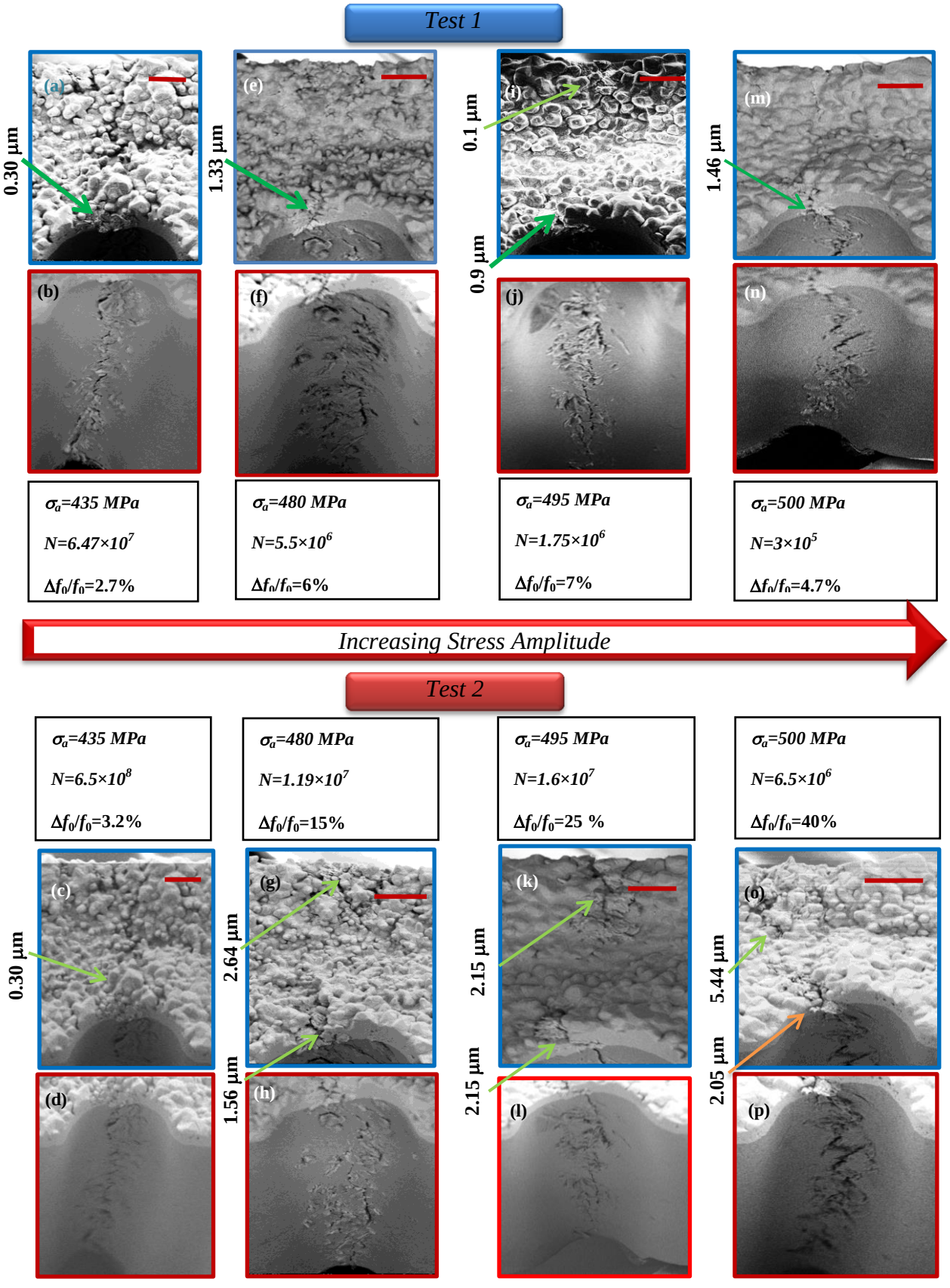

Figure 4.4: Sequential SEM images of fatigued microresonators. All scales are 1 µm.

The specimens fatigued in the harsh environment (80ºC, 90% RH) exhibit similar features (shown in Figure 4.5), although the height of the extrusions appears to be larger (~1 μm compared to <500 nm at 30ºC, 50% RH). In our previous study, local thick oxides were observed at the location of the extrusions thanks to TEM of thin samples extracted at the notch [41]. A larger, thicker oxide area was also present for a specimen fatigued in the harsh environment, which was consistent with the increase in f_0 observed only in that environment. This increase in extrusion height at 80ºC, 90% RH is therefore likely to be also the result of more oxide formation at the location of the extrusions.

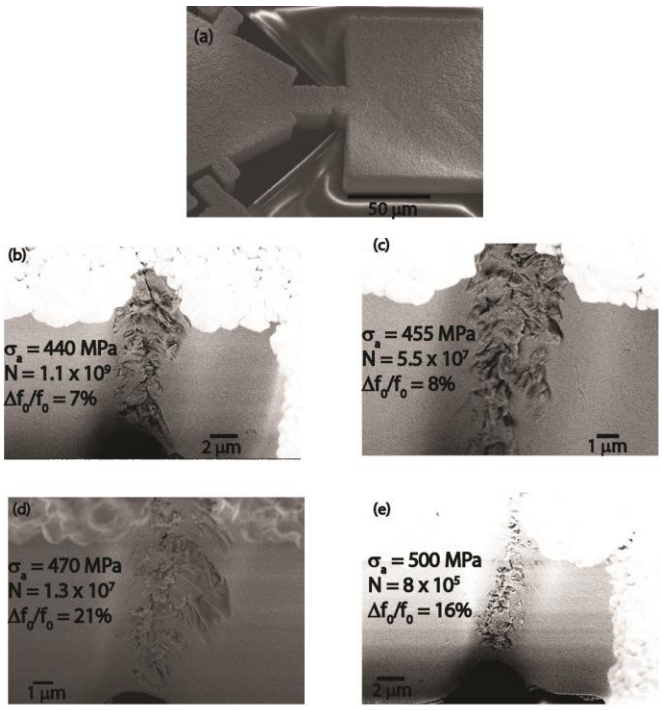

Figure 4.5: SEM images of the notched microbeams sidewalls after fatigue testing at 80ºC, 90% RH. (a) low-magnification image. High magnification SEM images at notch root after (b) 1.1×10^9 cycles at σ_a = 440 MPa; (c) 5.5×10^7 cycles at σ_a = 455 MPa; (d) 1.3×10^7 cycles at σ_a = 470 MPa; and (e) 8×10^5 cycles at σ_a = 500 MPa.

EDS measurements were performed on three specimens and confirmed the presence of higher oxygen concentration at the location of the extrusions (see elemental maps and concentration calculation in Figure 4.6). In a qualitative approach, an oxygen map of the beam has been presented, implying higher oxygen concentration on the notch root, (see the last elemental map, O K series in Figure 4.6). Following that, in a quantitative approach, this figure compares the elemental composition of two points on the area with higher extrusion concentration (spectrum 2 and 3) and a point free of extrusion (spectrum 1) and illustrates higher oxygen percentage on the area with highly localized extrusion.

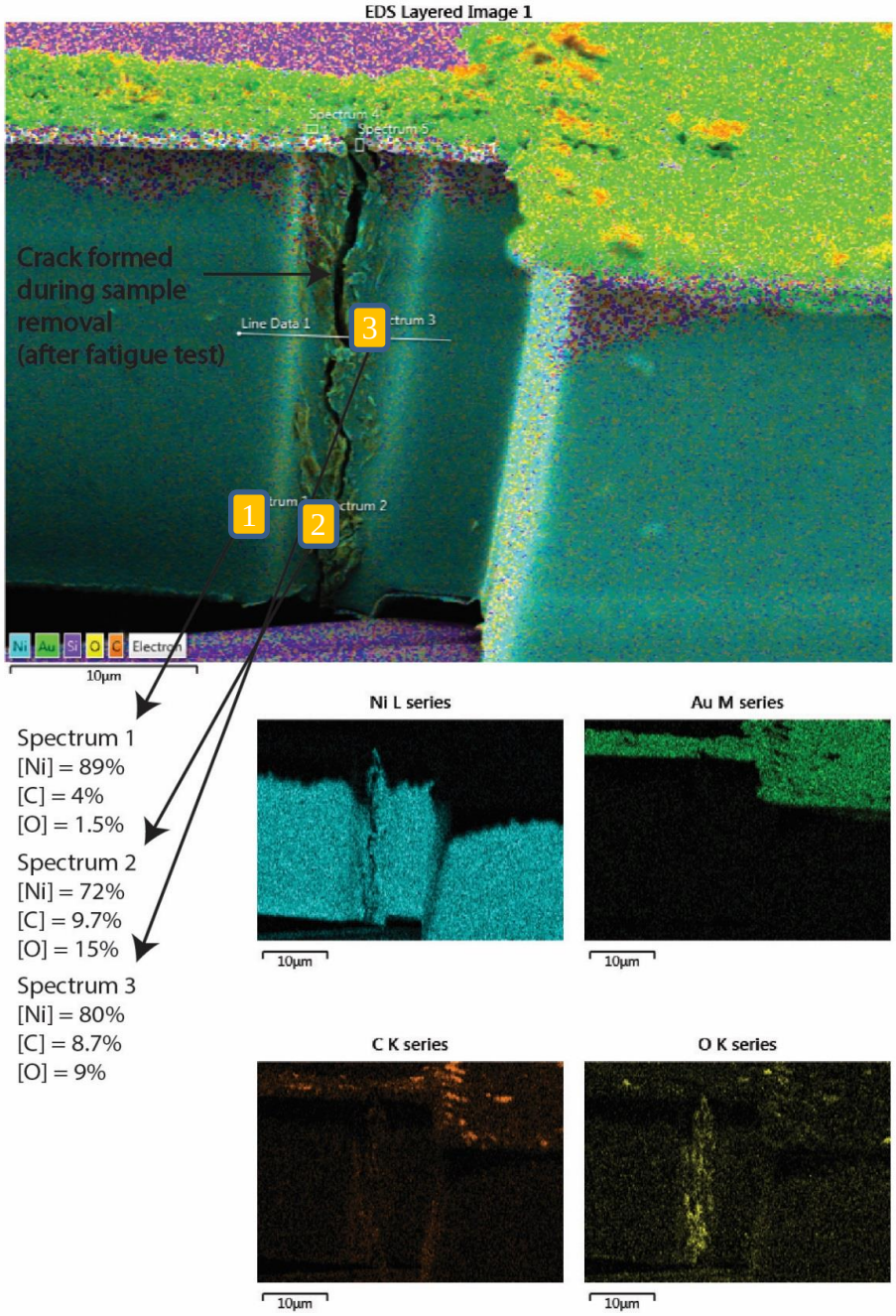

Figure 4.6: EDS layered elemental map of the notch sidewall of a fatigued microbeam at 80ºC, 90% RH (1.1×10^8 cycles at σ_a = 410 MPa, corresponding to a decrease in f_0 of 2%). The large crack observed throughout the thickness was introduced after the fatigue test, during sample removal.

In another qualitative approach Figure 4.7 shows the elemental composition distribution along an 11 μm length line (line map) which is crossing the notch root of microbeam presented in Figure 4.6. As shown in Figure 4.7, by moving along the line from left to right, initially the nickel is the highest detected element with about 9000 counts per second (CPS). The detected nickel amount starts to decrease near the notch root at the location of the extrusions. At the edge of the notch root, highlighted with a blue circle, the reflected X-ray emission is deviated and accumulated CPS for all materials decrease to 7000 (about 22 % reduction in detected X-ray emission). The sharp decrease in the detected nickel amount, highlighted with a red ellipse in Figure 4.7, is interpreted as a result of presence of the crack opening at this area. The interaction of the SEM primary electron beam with the edges of crack opening results in shell X-ray emission which gets trapped inside the crack opening and results in 80% reduction in the detected CPS. Along the line on notch root, starting from 4.5 to 7 μm, the detected oxygen percentage is increasing while the other detected elements percentages do not change a lot. This trend is a good indication of nickel oxide formation at the location of the extrusions. Comparing the line map (Figure 4.7) or elemental map (see Figure 4.6) with corresponding high resolution SEM images validates this pattern.

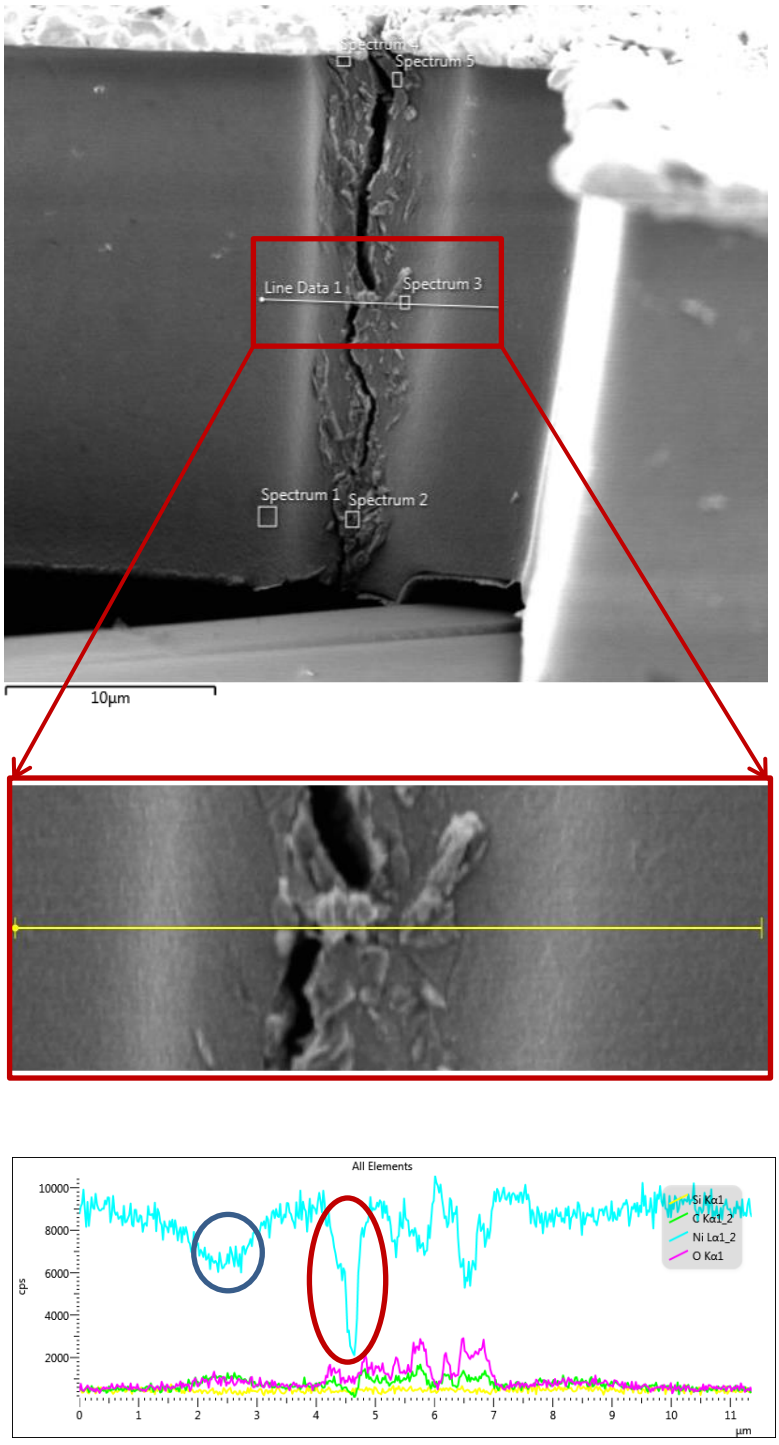

Figure 4.7: line map confirms the formation of localized oxides at extrusion and intrusion sites.

4.3 S-N Curve under Extreme Stress Gradient

Figure 4.8 (a) shows the stress-life (σ_a - N_f) fatigue curve for the notched microbeams tests in both environments, while Figure 4.8(b) shows the corresponding plastic strain-life (ε_{pa} – N_f) fatigue curve.

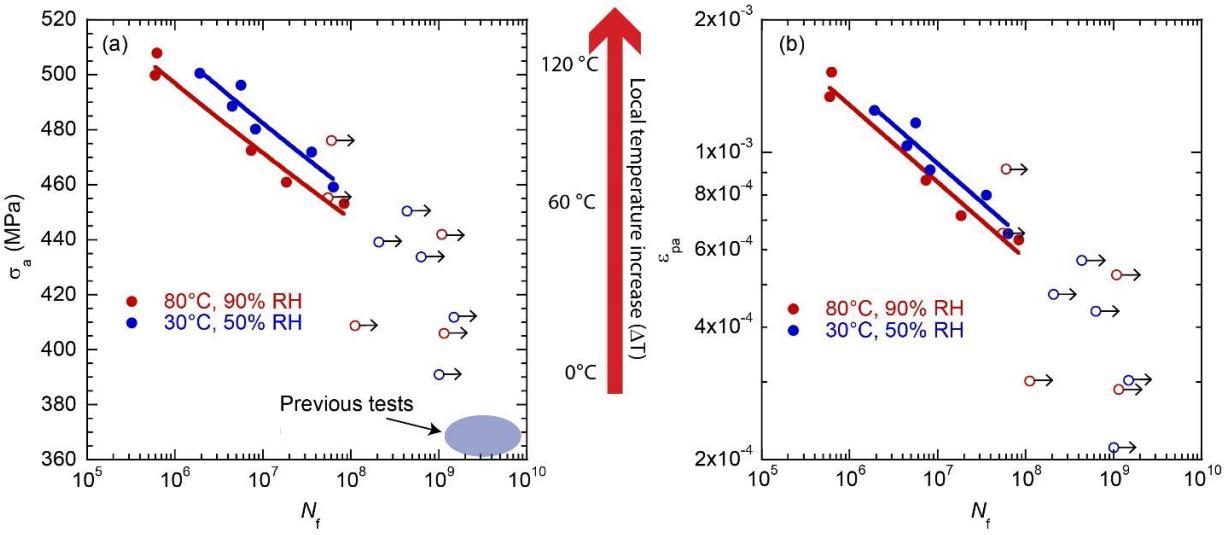

Figure 4.8: σ_a – N_f curves for tests performed in both environments. The red arrow indicates approximated local increase in temperature, ΔT (see Fig. 5(c)). (b) Corresponding ε_{pa} – N_f curves.

As a reminder, σ_a corresponds to the local stress value at the notch root, calculated at the beginning of a fatigue test. The plastic strain amplitudes were approximated using the Ramberg Osgood fit (see section 2.2 for more details). For each environment, the (σ_a - N_f) curve was fitted with the Basquin equation:

$$\sigma_a = \sigma'_f (2N_f)^b = 2^b \sigma'_f (N_f)^b = A N_f{}^b \quad (14)$$

and the (ε_{pa} – N_f) curve was fitted with the Coffin-Manson equation:

$$\varepsilon_{pa} = \varepsilon'_f (2N_f)^c = 2^c \varepsilon'_f (N_f)^c = B {N_f}^c \quad (15)$$

All the coefficients are summarized in *Table 8*. Figure 4.8 (a) also shows the approximated increase in temperature, ΔT, due to self-heating (see section 3.3), ranging from $\Delta T = 0$ at $\sigma_a = 400$ MPa to $\Delta T = 120$ ºC at $\sigma_a = 500$ MPa.

Table 8: Basquin and Coffin-Manson parameters.

Environment	σ'_f (MPa)	b (-)	ε'_f (-)	c (-)
30ºC, 50% RH	700	-0.023	0.016	-0.17
80ºC, 90% RH	680	-0.023	0.014	-0.17

The fatigue limit, σ_l, of these notched Ni microbeams is about 440-450 MPa for both environments, corresponding to ~50% of the ultimate tensile strength. This limit is significantly larger than the previously observed 30% for bulk Ni, or even previous electroplated Ni films studies (30 ± 10%) [4, 72-74]. In addition to a large fatigue limit, the σ_a - N_f and $\varepsilon_{pa} - N_f$ curves exhibit unusual Basquin and Coffin-Manson coefficients, respectively. The Basquin coefficient, *b*, is -0.023 at both 30ºC, 50% RH and 80ºC, 90% RH. Typical *b* values for bulk metals range from -0.05 for hardened metals to -0.12 for soft metals, with an average value of b = -0.085 [19]. Similarly, the Coffin-Manson coefficient, *c*, is -0.18 at both 30ºC, 50% RH and 80ºC, 90% RH, while typical *c* values for bulk metals are -0.6 (ranging from -0.5 to -0.8) [19]. The modest (~60ºC) increase in temperature for $N_f = 10^6$ compared to 10^8 cycles is unlikely to account for these low absolute values of *b* and *c*. Instead, the explanation is more likely associated with the extreme stress gradients ahead of the notch, leading to unusual fatigue crack propagation rates curves.

4.4 Finite Element Analysis Results

In this section, a FEM model is presented to correlate crack growth at the notch root to frequency decrease at the micro resonator. Figure 4.9 shows the main results of the FEM model and SEM image of FIB etched notch root to experimentally measure the crack length and to evaluate the accuracy of the 2D crack propagation assumption. To model the crack propagation for the micro resonator with 0.36 μm^{-1} stress gradient, it has been assumed that a 2D thickness crack throughout the beam initiates at the notch root and propagates towards the neutral axis of the beam (as seen in Figure 4.9 (a)). As shown in section 4.2, the fatigue damage along the thickness of these microbeams consist of 3D cracks that link up to form a 2D-like crack. Hence, the model predicts the size of an equivalent 2D crack, whose corresponding Δf_0 is the same as that of the actual crack. Similarly, the model predicts an average crack growth rate for that equivalent 2D crack, whereas the actual configuration most likely consists of nearby 3D crystallographic cracks that may not grow simultaneously. It has also been assumed that the above mentioned crack propagates to a certain length before it stops and a secondary crack starts to form and propagates from the back side of the beam. There the SEM images from the notch root (section 4.2) show that when Δf_0 exceeds 800 Hz (~10% of the initial f_0) or when the crack at the notch reaches a certain length (about 2 microns), a secondary crack forms and starts growing on the back side of the beam. This observation can be explained by the stress distribution along the beam ligament extracted by FEM model and shown in Figure 4.9 (b). It is seen in the figure that, as the crack at the notch reaches a certain length (shown by the arrow), the stress amplitude at the crack tip decreases to the corresponding level of stress at the back of the beam

(indicated by the dashed line in Figure 4.9 (b)). That could cause the initiation of the secondary crack at the back side of beam, followed by simultaneous propagation of these two cracks, on both sides of the beam, towards the neutral axis. For this reason, the crack growth rate calculation for the resonator with 0.36 μm^{-1} stress gradient is based on the corresponding FEM model, which is valid only for the propagation of the first crack along its first two microns of length. Also, for this resonator, 2-micron crack growth at the notch is considered to be the failure criterion, which corresponds to a 10% decrease in resonant frequency. Considering that the average grain size is about 2 microns, this FEM model enables us to investigate crack propagation on the order of a grain size.

Considering the SEM images of microbeam (see Figure 4.4, in section 4.2), the cracks were not easily observed at the top surface. Therefore, the crack size was measured in one instance by cutting a trench along the notch's sidewall using focused ion beam, from which the crack tip could be observed (see Figure 4.9 (c)). This figure shows the etched windows along the notch root, which enables us to track the tips of formed cracks. Zoomed window in this figure used to measure the crack size (a =1.9 μm) at the notch root for a fatigued specimen with Δf_0 = 850 Hz, which is in reasonable agreement with the predicted a = 2.0 μm (see Figure 4.9(d)).

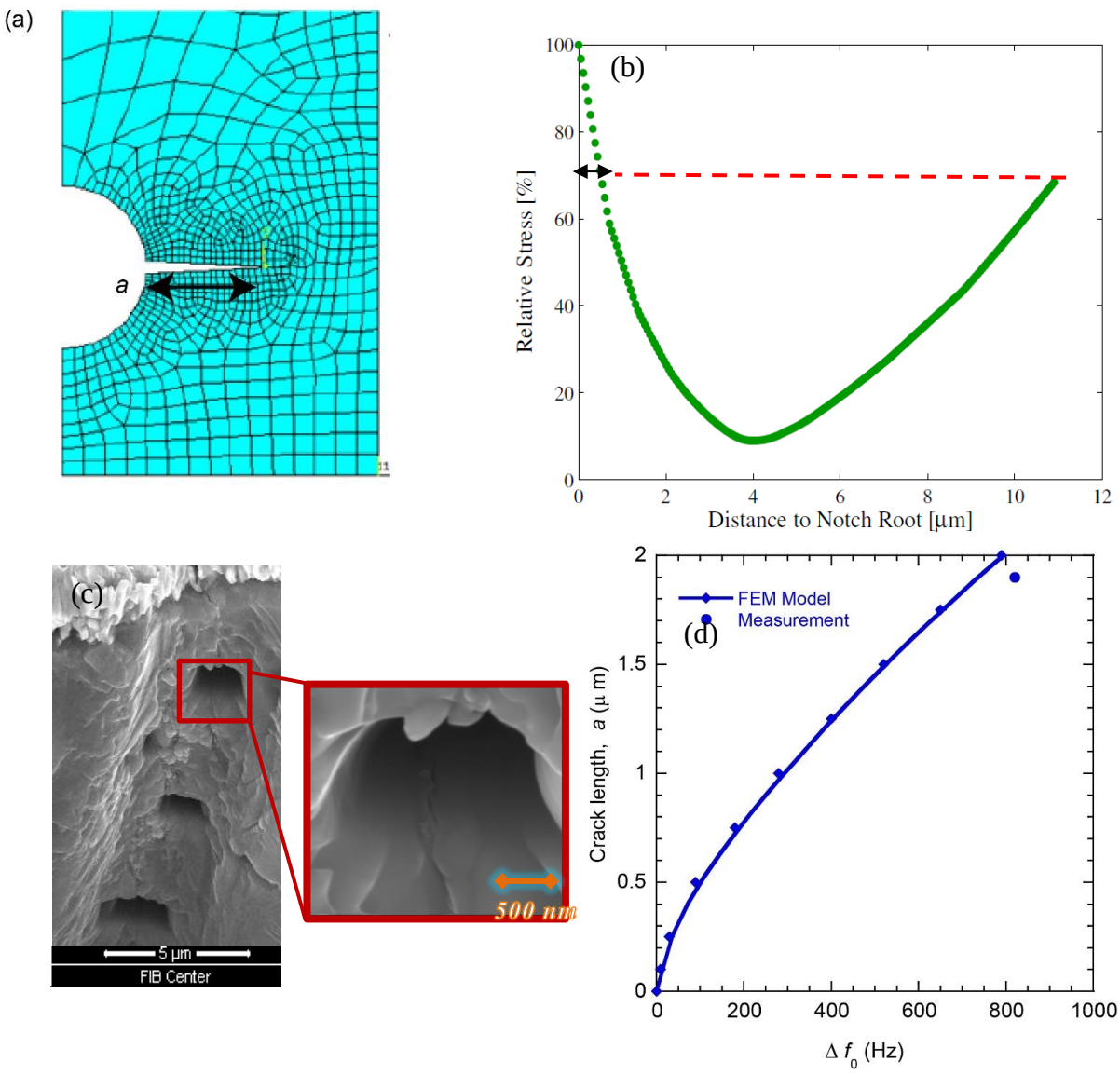

Figure 4.9: (a) Finite-Element model for a crack propagation at notch root. (b) Stress distribution along the ligament. (c) SEM image of notch root has been used to measure the propagated crack length. (d) Comparing the modeled crack length, *a*, as a function of decrease in f_0, Δf_0 with experimentally measured value.

4.5 Crack Growth Rate Calculation and Results

The crack growth rates are evaluated based on the f_0 evolution plots, which are transformed into "*a* vs *N*" plots (with *a* crack size at the notch root) through a 2D FEM (presented in section 2.6.1) predicting *a* as a function of the measured decrease in f_0, Δf_0. As mentioned earlier, cracks also nucleate and propagate from the back side of the microbeam when Δf_0 exceeds 800 Hz (~10% of the initial f_0). Hence, the crack size at the notch root, *a*, can only be approximated over the first 2 microns (corresponding to Δf_0 = 800 Hz), as it is not possible to decouple the contributions of the cracks from the notch side and backside on Δf_0. As shown in section 4.2, the fatigue damage along the thickness of these microbeams consists of 3D cracks that link up to form a 2D-like crack. Hence, the model predicts the size of an equivalent 2D crack, whose corresponding Δf_0 is the same as that of the actual crack. Similarly, the model predicts an average crack growth rate for that equivalent 2D crack, whereas the actual configuration most likely consists of nearby 3D crystallographic cracks that may not grow simultaneously. Figure 4.10 (a) shows the calculated "*a* vs *N*" curves for 3 specimens tested at 30ºC, 50% RH, while Figure 4.10 (b) shows the corresponding "d*a*/d*N* vs *a*" curves. The crack growth rates d*a*/d*N* were obtained from polynomial fits of segments of the "*a* vs *N*" curves, reducing considerably the noise with respect to the secant method used previously [75]. Unlike typical crack growth rates curves measured for long cracks in bulk materials (showing increasing rates with increasing cracks), these curves exhibit decreasing rates with increasing crack size from 0 to 2 μm. This trend can be explained in part by the fact that these are microstructurally small cracks (on the same order of grain size), which are known to decelerate due to the presence of

microstructural obstacles (such as grain boundaries) [20]. However, microstructurally small cracks usually exhibit larger growth rates (although decelerating) than long cracks'. Here, we observe extremely small crack growth rates, with the maximum rates, $da/dN \sim 10^{-11}$ m/cycle, corresponding to the smallest range of rates measured for long cracks in air. It is therefore likely that the presence of extreme stress gradients ahead of the micronotch also plays a significant role in the fatigue crack kinetics, contributing to these slow, decelerating microstructurally small fatigue cracks.

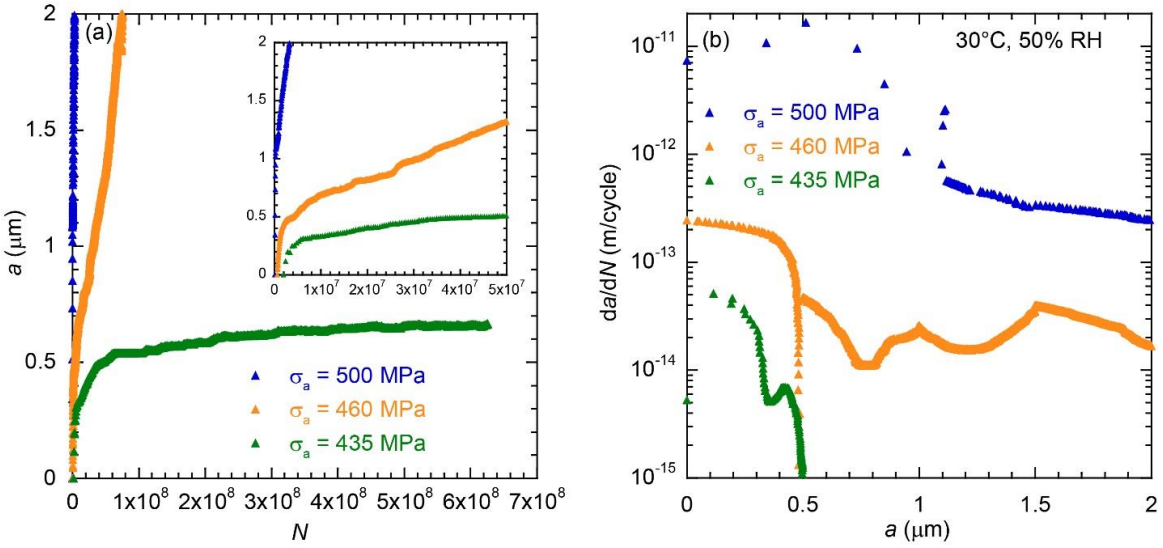

Figure 4.10: (a) Calculated crack size, *a*, as a function of cycles for three representative tests performed at 30ºC, 50% RH. (b) Corresponding crack propagation rate curves.

4.6 Discussion

The previous section highlighted the singular fatigue behavior of these Ni notched microbeams. Typically, the fatigue life N_f for bulk specimens, or even thin film specimens under uniaxial loading, can be decomposed as the sum of the initiation fatigue life, N_i, corresponding to the nucleation and growth of a crack to an arbitrary

crack size (typically a fraction of 1 mm) and propagation fatigue life (N_p) up to the critical crack size [76]. N_i encompasses the number of cycles to nucleate a crack (N_{nucl}) and to grow microstructurally small cracks (N_{MSC}), i.e. crack sizes up to 3 to 10 times the grain size, and physically small cracks (N_{PSC}), while N_p is mainly associated with the growth of long cracks (N_{LC}) for which linear elastic fracture mechanics (LEFM) framework is valid:

$$N_f = N_i + N_p = (N_{nucl} + N_{MSC} + N_{PSC}) + (N_{LC}) \quad (16)$$

In contrast, the fatigue degradation properties of these notched microbeams only relates to the nucleation and early growth of microstructural small cracks (up to ~1 to 2 times the grain size (1-2 μm)) under extreme stress gradients:

$$N_{f,notched\ microbeam} = (N_{nucl} + N_{MSC})_{extreme\ stress\ gradients} \quad (17)$$

Despite the smaller amount of crack propagation required to reach the fatigue life of the microbeams, the (σ_a - N_f) and (ε_{pa} – N_f) fatigue curves show the behavior of fatigue-resistant components, with high endurance limit (50% of σ_{uts}, corresponding $\varepsilon_{pa} \sim 5\times10^{-4}$) and unusually low (in absolute values) *b* and *c* coefficients for the Basquin and Coffin-Manson equations (see *Table 8*). For the large σ_a values investigated in this study, the extrusions form relatively quickly and are likely to constitute only a small portion of N_f. Hence the unusual fatigue curves are likely the direct consequence of having N_f governed by the propagation of microstructurally small cracks under extreme stress gradients present at the notch root (average stress gradient of -36% per μm over the first 2 μm, ahead of the notch). The prediction of N_f for these notched microbeams

would therefore require an accurate characterization of the crack growth rates under these loading conditions.

Fracture mechanics (whether linear elastic or elastic plastic) is not valid for describing the early growth of these stage I cracks characterized by lower thresholds, larger crack growth rates compared to long cracks, and decelerating crack growth when approaching microstructural barriers such as grain boundaries. Instead, Miller introduced a microstructural fracture mechanics equation, of the form [20]:

$$\frac{da}{dN} = A{\gamma_{pl,a}}^{\alpha}(d-a) \tag{18}$$

The "d*a*/d*N* vs *a*" curves shown in Figure 4.10 (b) exhibit decreasing crack growth rates with increasing *a*, in qualitative agreement with eq. (18). Figure 4.11 shows the initial crack growth rates, $(da/dN)_i$ (for $a = 0$) as a function of σ_a (Figure 4.11 (a)) and ε_{pa} (Figure 4.11 (b)), for all the specimens for which a 2D crack was observed at the end of the tests. The initial rates increase from ~10^{-13} to 10^{-11} m/cycle for ε_{pa} increasing from 4×10^{-4} to 2×10^{-3}, corresponding to $\alpha = 3$ (from eq. (18)).

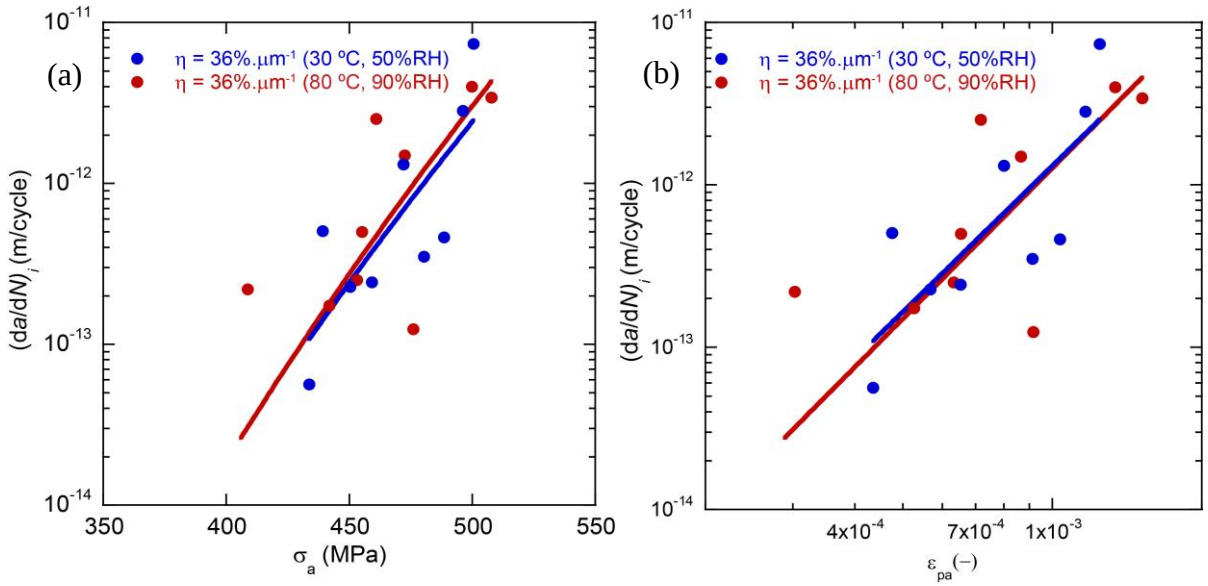

Figure 4.11: Initial crack propagation rates, $(da/dN)_i$ as a function of (a) σ_a, and (b) ε_{pa}

4.7 Conclusions

In conclusion, this study revealed the critical role of extreme stress gradients, often encountered in micro-components, on their fatigue behavior. The notched microbeams, characterized by a normalized stress gradient of -36%/μm, required from 10^6 to 10^8 cycles (under fully reversed loading) to grow a 2-μm-long microstructurally small crack through the entire beam thickness (20 μm), for stress amplitudes ranging from 500 to 440 MPa (60 to 50% of the ultimate tensile strength). The crack growth rate curves inferred from the f_0 evolution curves reveal ultraslow growth of these cracks (initial rates ranging from 10^{-13} to 10^{-11} m/s), with decreasing rates as the cracks grow. This ultraslow growth is unlike that of microstructurally small cracks in the absence of extreme stress gradients, and is responsible for the shallow stress and strain-life curves and high endurance limits. This study highlights the need to further characterize the

effects of different stress gradients values on crack growth rates and fatigue lives in order to accurately predict the small-scale fatigue damage in metallic microbeams.

CHAPTER 5: COMPARING THE FATIGUE BEHAVIOR OF NI MICROBEAMS UNDER DIFFERENT STRESS GRADIENTS: 17 VS 36 %.μm^{-1}

5.1 Resonance Frequency Evolution

In this section, the results of fatigue tests performed for the microresonator with $\eta = 0.17\ \mu m^{-1}$ in both mild and harsh environments (at 30ºC, 50% RH and 80ºC, 90% RH, respectively) are presented and compared with the results shown in the previous chapter ($\eta = 0.36\ \mu m^{-1}$). Figure 5.1 (a) shows the f_0 evolution during the fatigue tests of 3 representative specimens (η = 17%.μm^{-1}) tested at 30 °C, 50% RH, in the form of normalized f_0 with respect to the initial value ($f_{0,i}$ ~ 8600 Hz), $f_0/f_{0,i}$, as a function of cycles (out of a total of 22 fatigued specimens with η = 17%.μm^{-1}). The horizontal line at $f_0/f_{0,i}$ = 90% constitutes our failure criterion (corresponding to a crack size of ~2.2 μm on each side of the beams for (η = 17%.μm^{-1}), see finite element model at section 2.6.1). For σ_a = 305 MPa, f_0 slowly decreases and levels off at 95% of the initial value after 1.5×10^9 cycles. For σ_a = 355 MPa, f_0 decreases and reaches 90% of the value at $N = N_f = 1.5\times10^7$ cycles, after which f_0 decreases at a much faster rate until it reaches 60% of the initial value. For σ_a = 400 MPa, f_0 reaches 90% of the initial value at $N = N_f = 3.7\times10^6$ cycles, which also corresponds to the onset of faster decrease rates. The test was interrupted shortly after ($f_{0,final}/f_{0,i}$ = 87%). Figure 5.1 (b) show representative f_0 evolution curves for four specimens with η=0.36 μm^{-1} tested at 30ºC, 50% RH with σ_a = 330, 450,470, and 500 MPa. Here also a total decrease of 40% can be reached, in that case after 1.5×10^7 cycle for the specimen with σ_a = 500 MPa.

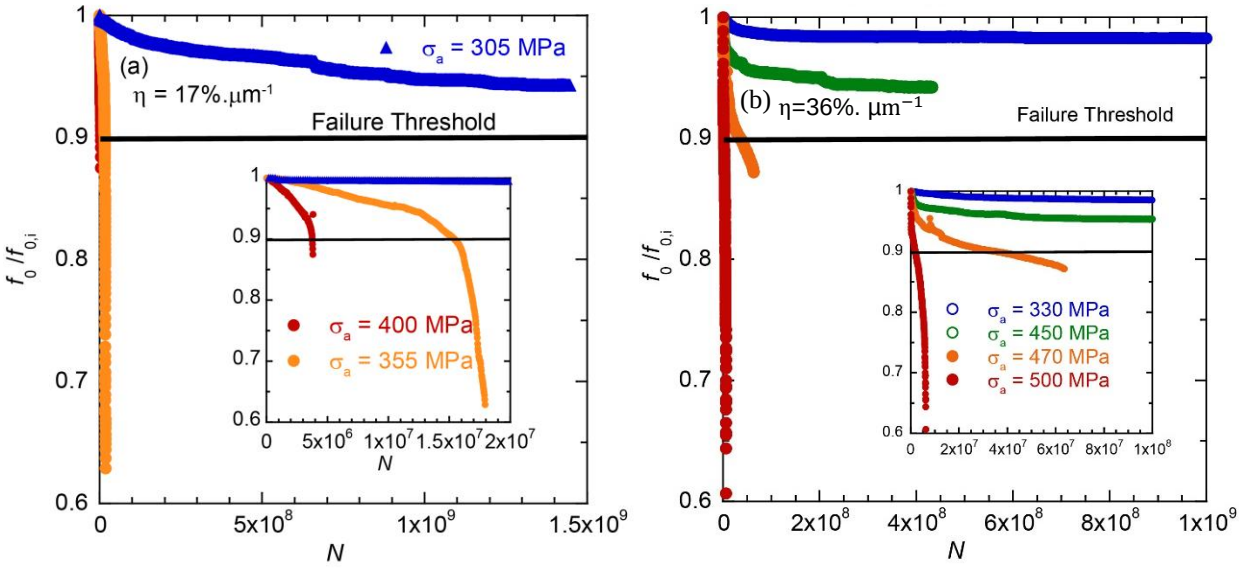

Figure 5.1: Normalized f_0 evolution, $f_0/f_{0,i}$, as a function of cycles for microresonators with (a) $\eta = 0.17\ \mu m^{-1}$ and (b) $\eta = 0.36\ \mu m^{-1}$.

The general trend of frequency development for both series of microresonators with $\eta = 0.17$ and $0.36\ \mu m^{-1}$ is similar in term of decreases in f_0 (up to 40%), which are indicative of accumulation of fatigue damage in the form of cracking for both of 0.36 and $0.17\ \mu m^{-1}$ (see sections 4.2 and 5.2). But the amounts and rates of decrease in f_0 are clearly different. For example, a slow decrease totaling 2% over 10^9 cycles was observed for $0.36\ \mu m^{-1}$ at σ_a = 330 MPa (see Figure 5.1 (b)), while for a microresonator with $0.17\ \mu m^{-1}$ (over same number of cycles, 10^9), it loses more than 5% of the initial f_0 at slightly lower stress, σ_a = 305 MPa (See Figure 5.1 (a)). Unlike the frequency development for microresonator with $\eta = 0.36\ \mu m^{-1}$, there is not any pronounced sudden increase in f_0 upon interruption of a test. The f_0 evolution curve for

microresonator with $\eta = 0.17\mu m^{-1}$ remains almost the same to the value seen prior to interruption of the test upon resuming the fatigue test. That means the temperature-dependent decrease in elastic modulus E and therefore in stiffness and corresponding f_0 due to dislocation damping (cyclic plastic deformation at high frequency) was not observed or negligible for microresonator with $\eta = 0.17\mu m^{-1}$. Considering the maximum calculated stress level for $\eta = 0.17\mu m^{-1}$ (415 MPa), this observation makes sense given the predicted temperature trend in Chapter 3 (see Figure 3.16) where the temperature-included frequency decrease has been considered negligible for the microresonators with stress levels below 400 MPa at notch root.

Figure 5.2 (a, b) shows the total irreversible normalized decrease in f_0 as a function of σ_a and N_f, respectively, for all fatigue tests (at 30ºC, 50% RH and 80ºC, 90% RH, both series of microresonators with 0.36 and $0.17\mu m^{-1}$stress gradient). For the similar stress levels, no significant difference can be observed between the two environments for both series of microresonators. Figure 5.2 (a) shows that for a certain level of decrease in resonance frequency (for example 10%), the corresponding stress level is lower for the microresonator with $0.17\mu m^{-1}$ stress gradient in comparison to $0.36\ \mu m^{-1}$(400 and 470 MPa respectively, see Figure 5.2 (a)). It should be mentioned that similar to microresonators with $0.36\ \mu m^{-1}$, none of the microbeams with $0.17\mu m^{-1}$stress gradient are fractured in two pieces at the end of the tests; as a result, the total decrease depends on when the test was interrupted. All specimens shown in Figure 5.2 (a, b) with a total decrease less than 10% (below the threshold line) are considered as runouts. The fatigue life, N_f was defined as the number of cycles to reach an irreversible decrease in f_0 of 10% of the initial value (which is indicated as failure

threshold in Figure 5.2). This number was chosen because it corresponds to a 2D crack of 2 μm at the notch root (see section 2.6.1 for more details).

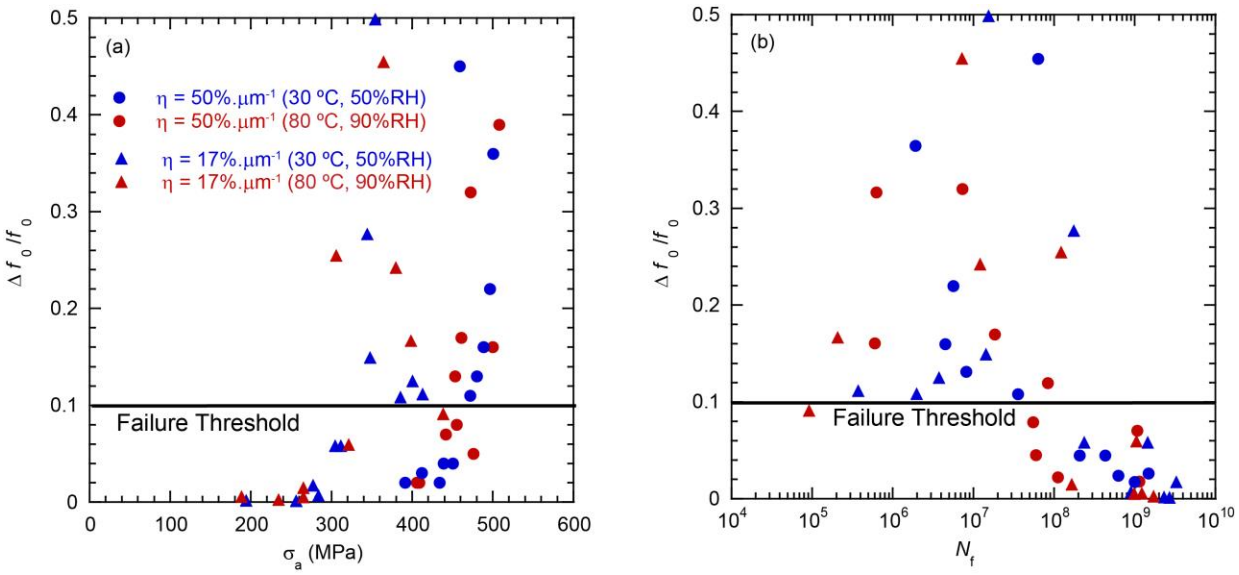

Figure 5.2: Normalized decrease in f_0, $\Delta f_0/f_0$, for all fatigue tests (at 30ºC, 50% RH and 80ºC, 90% RH, for both series of microresonators with 0.36 and 0.17 μm^{-1} stress gradient) as a function of (*a*) σ_a and (b) N_f, the legend is same for both figures.

5.2 SEM Observations and EDS Results

Figure 5.3 and Figure 5.4 show representative SEM images of the fatigue damage at the edges of the microbeams ($\eta = 0.17 \mu m^{-1}$) stress gradient for various σ_a values (ranging from 190 to 440 MPa), numbers of applied cycles, and the corresponding normalized decreases in f_0, for fatigue tests performed at 30ºC, 50% RH and 80ºC, 90% RH, respectively. In contrast to SEM images of notch root of microresonator with $\eta = 0.36\ \mu m^{-1}$ (presented in section 4.2), the fatigue damage are more widespread and distributed along the beam length on both sides of that which is reasonable considering the design criteria (see section 2.4), where 17 μm of beam

length is considered to experience the 95% and more of maximum stress. Similar to microresonators with $0.17\mu m^{-1}$stress gradient, here also extrusions are present across the entire thickness of the Ni microbeams at the notch root, along with cracks meandering through these extrusions.

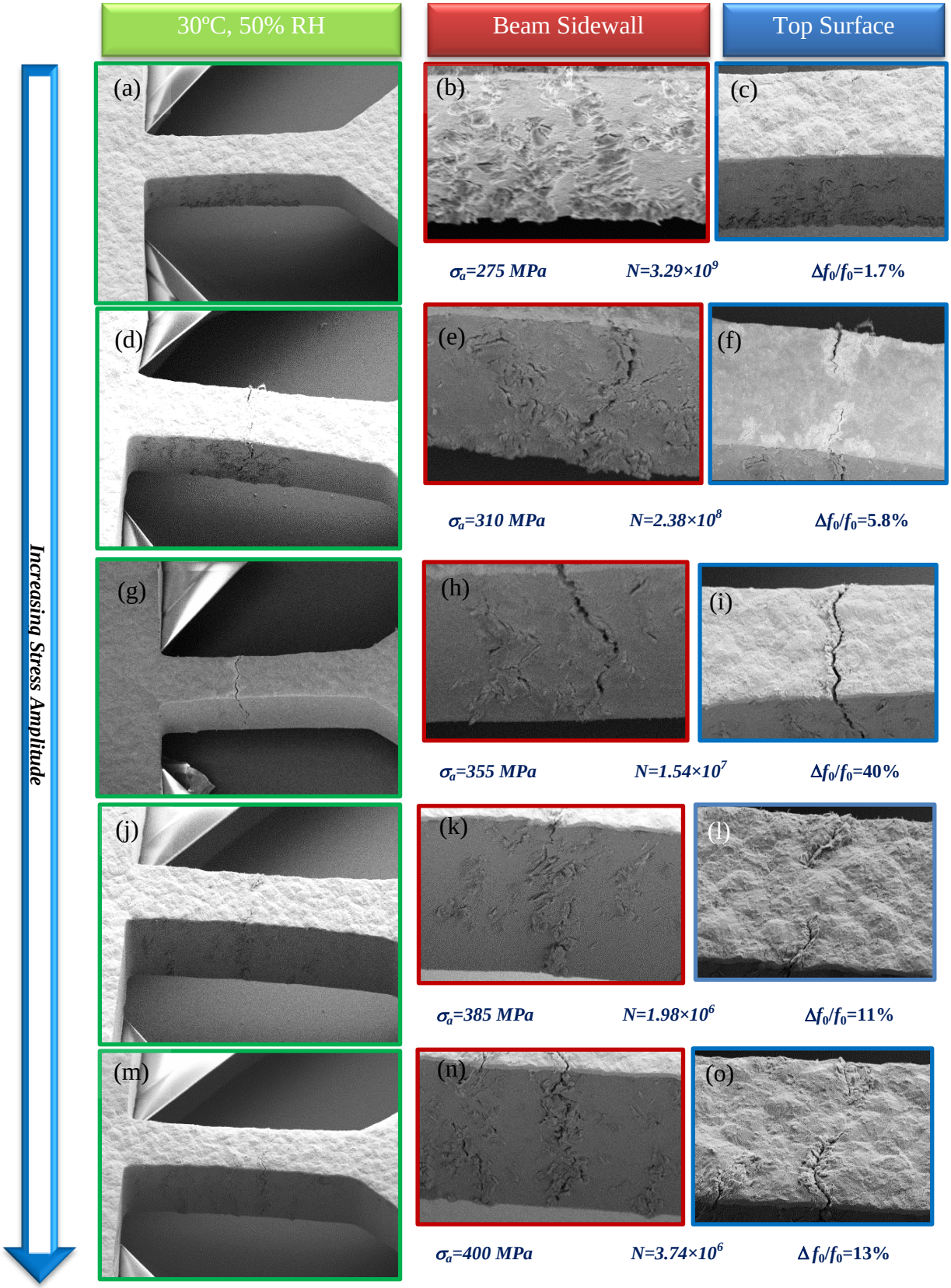
30°C, 50% RH
Beam Sidewall
Top Surface
Increasing Stress Amplitude
(a)
(b)
(c)
σ_a=275 MPa
N=3.29×10^9
$\Delta f_0/f_0$=1.7%
(d)
(e)
(f)
σ_a=310 MPa
N=2.38×10^8
$\Delta f_0/f_0$=5.8%
(g)
(h)
(i)
σ_a=355 MPa
N=1.54×10^7
$\Delta f_0/f_0$=40%
(j)
(k)
(l)
σ_a=385 MPa
N=1.98×10^6
$\Delta f_0/f_0$=11%
(m)
(n)
(o)
σ_a=400 MPa
N=3.74×10^6
$\Delta f_0/f_0$=13%

Figure 5.3: SEM images of the notched microbeams sidewalls and top surface after fatigue testing at 30ºC, 50% RH. (a, d ,g, j, and m) low-magnification image. (b) and (c) high magnification images of the sidewall and top surface of beam, respectively, after 3.29×10^9 cycles at σ_a = 277 MPa. (e) and (f) sidewall and top surface (respectively) after 2.38×10^8 cycles at σ_a = 312 MPa. (h) and (i) sidewall and top surface, respectively, after 1.54×10^7 cycles at σ_a = 355 MPa. (k) and (l) sidewall and top surface, respectively, after 1.98×10^6 cycles at σ_a = 386 MPa. And (n) and (o) high-magnification image of crack along sidewall and top surface of beam, respectively, after 3.74×10^6 cycles at σ_a = 400 MPa.

The initial zig-zag pattern of the cracks along the microbeam's thickness suggests that 3D stage I cracks which are forming at the edges of each extrusion (see high magnification SEM images in Figure 5.3 (h, k, and n) or Figure 5.4 (e, h, k, and n); eventually link up to form a "2D" crack.

Figure 5.3 (g-i) and (m-o) show SEM images of the notch root sidewall and top surface (consisting of a 0.5-μm-thick Au layer on top of the 20-μm-thick Ni films) of two specimen presented in Figure 5.1 (a) which are tested at 30 °C, 50% RH with corresponding stress of σ_a = 355 MPa and σ_a = 400 MPa, respectively. For σ_a = 400 MPa ($f_{0,final}/f_{0,i}$ = 87% which corresponds to $\Delta f_0/f_0$=13% in Figure 5.3(o)), fatigue damage can be observed along the entire length of the beam's sidewall, in the form of extrusions (Figure 5.3 (n)). Two main cracks, one on each side, have propagated towards the beam's neutral axis. The high magnification image of one of these cracks (in Figure 5.3 (o)) shows that it spans the entire beam's thickness (which is confirmed with the cross-section SEM images shown in Figure 5.11 (b)), although in a jagged manner, and that it propagates at a ~45° angle with respect to the stress loading axis

over the first 2 microns, after which it switches direction. The cracks are therefore likely to be crystallographic in nature. For σ_a = 355 MPa ($f_{0,final}/f_{0,i}$ = 60%), the two main cracks have joined at the top surface, but not at the bottom part (Figure 5.3 (h,i)). The larger cracks observed in this specimen (compared to the previous one) are consistent with the fact that this specimen was tested until f_0 decreased to 60% of $f_{0,init.}$ (as opposed to 87% in the previous specimen). All specimens tested at σ_a > 310-320 MPa, for which $f_{0,final}/f_{0,i}$ < 90% also had one main crack on each side. Conversely, specimens for which $f_{0,final}/f_{0,i}$ > 98% (corresponding to σ_a < 300 MPa) did not have any cracks propagating towards the beam's neutral axis as illustrated in Figure 5.3 (b, c) (σ_a = 275 MPa, $f_{0,final}/f_{0,i}$ = 98.3%).

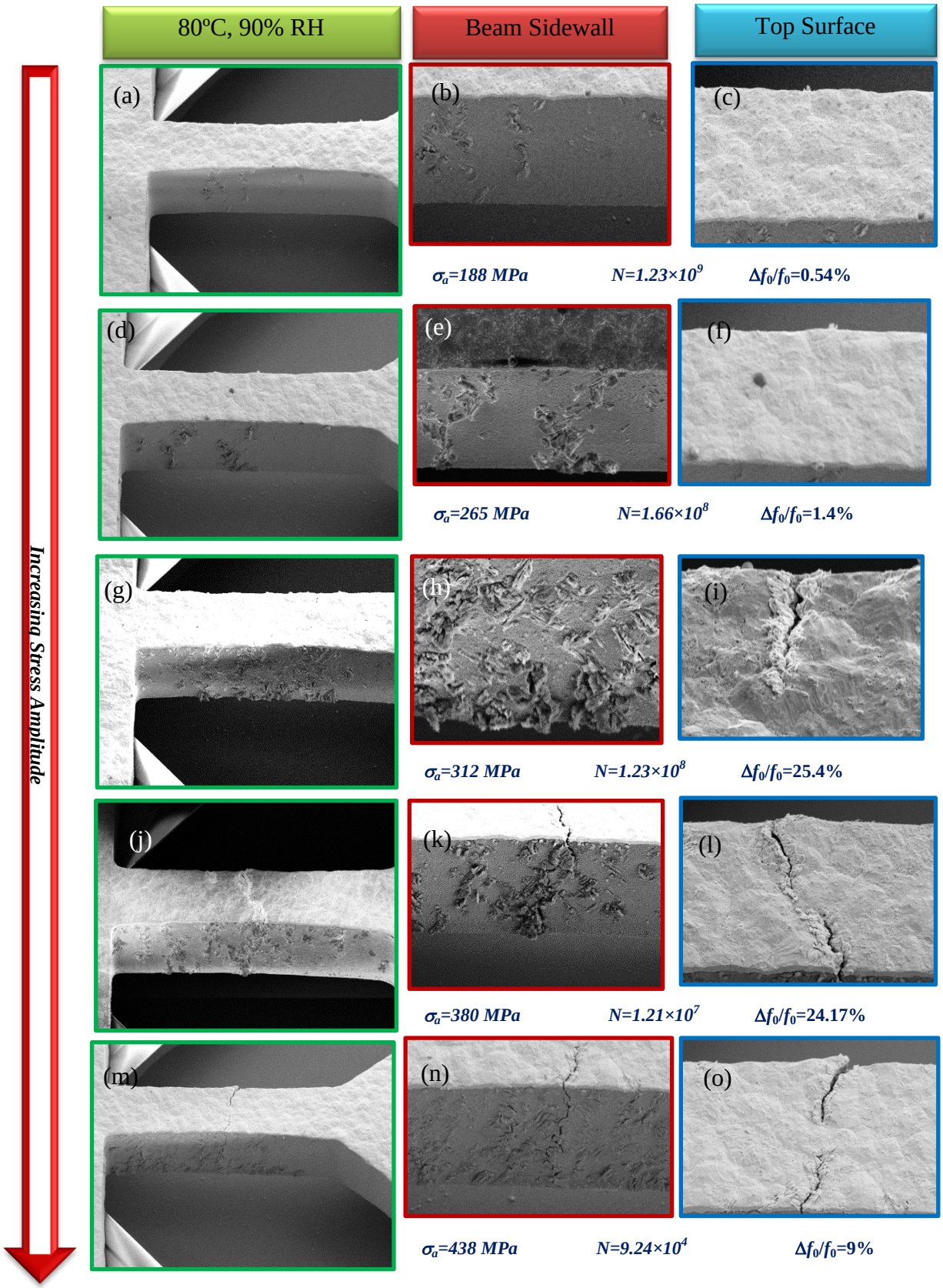
80ºC, 90% RH
Beam Sidewall
Top Surface
Increasing Stress Amplitude
(a)
(b)
(c)
σa=188 MPa
N=1.23×10^9
Δf0/f0=0.54%
(d)
(e)
(f)
σa=265 MPa
N=1.66×10^8
Δf0/f0=1.4%
(g)
(h)
(i)
σa=312 MPa
N=1.23×10^8
Δf0/f0=25.4%
(j)
(k)
(l)
σa=380 MPa
N=1.21×10^7
Δf0/f0=24.17%
(m)
(n)
(o)
σa=438 MPa
N=9.24×10^4
Δf0/f0=9%

Figure 5.4: SEM images of the notched microbeams sidewalls and top surface after fatigue testing at 80ºC, 90% RH. (a, d ,g, j, and m) low-magnification image. (b) and (c) high magnification images of the sidewall and top surface of beam, respectively, after 1.23×10^{9} cycles at σ_a = 188 MPa. (e) and (f) sidewall and top surface (respectively) after 1.66×10^{8} cycles at σ_a = 265 MPa. (h) and (i) sidewall and top surface, respectively, after 1.23×10^{8} cycles at σ_a = 312 MPa. (k) and (l) sidewall and top surface, respectively, after 1.21×10^{7} cycles at σ_a = 380 MPa. And (n) and (o) high-magnification image of crack along sidewall and top surface of beam, respectively, after 9.24×10^{4} cycles at σ_a = 438 MPa.

Figure 5.5 (a, b) show EDS results along the sidewall of two microbeams with η = 17%.μm^{-1} that were tested at 30°C, 50% RH (σ_a = 355 MPa, $N_f = 1.54 \times 10^7$ cycles, see Figure 5.1 for the corresponding f_0 evolution), and at 80°C, 90% RH (σ_a = 370 MPa, $N_f = 1.8 \times 10^7$ cycles, 50% decrease in f_0), respectively. The elemental maps of the beam sidewalls reveal that all the extrusions are associated with much larger oxygen contents than the adjacent areas subjected to the same σ_a where no extrusions were formed.

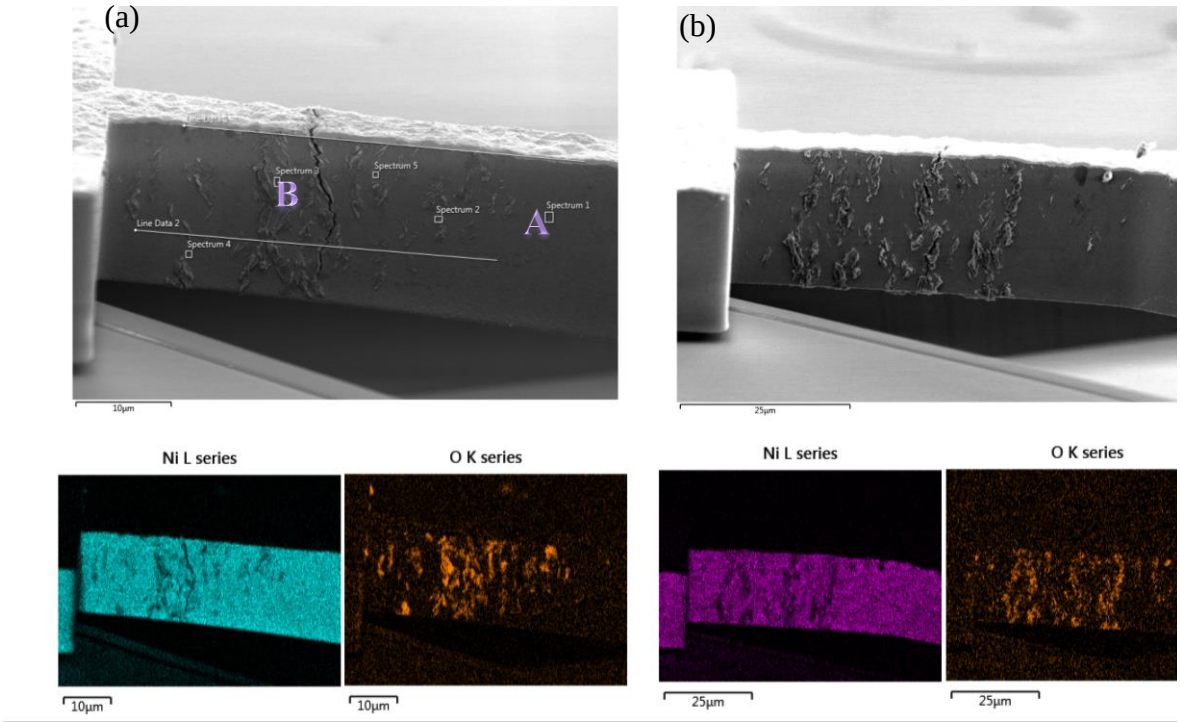

Figure 5.5: EDS results along the sidewall of specimens tested at: (a) 30°C, 50% RH (σ_a = 355 MPa, N_f = 1.54× 10^7 cycles, 40% decrease in f_0. (b) 80°C, 90% RH (σ_a = 370 MPa, N_f = 1.8 × 10^7 cycles, 50% decrease in f_0).

Local spectra show that the oxygen concentration is only ~1wt% in areas away from the extrusions (point A in Figure 5.5 (a)), but up to 20-25wt% at the location of extrusions (point B in Figure 5.5 (a)). The increased oxygen concentration must therefore be related to the cyclic slip activities occurring at the extrusions, perhaps due to a sweeping mechanism from which oxygen or water molecules get incorporated into the material during slip reversal of newly exposed and oxidized slip steps.

For η = 0.36μm^{-1}, the height of the extrusions appears to be larger in the harsh environment (80ºC, 90% RH) (~1 μm compared to <500 nm at 30ºC, 50% RH), see section 4.2 for more details. For these microbeams, a larger (thicker) oxide area was

observed for a specimen fatigued in the harsh environment, which was consistent with the increase in f_0 observed only in that environment (see Chapter 4). Here, for η = 0.17μm^{-1}, similar fatigue damage is observed in both mild and harsh environments (see Figure 5.3 and Figure 5.4). The presence of localized oxide area is also observed in both mild and harsh environments (see elemental composition in Figure 5.8.

In another qualitative approach, Figure 5.6 shows the oxygen and nickel elemental composition variation along a 38 μm length line (the yellow line in Figure 5.6 (a)) which is crossing the extrusions at sidewall of the beam. Figure 5.6 (b) compares the detected CPS (counts per second) for oxygen and nickel along the line and confirms the presence of higher oxygen concentration at the location of the extrusions.

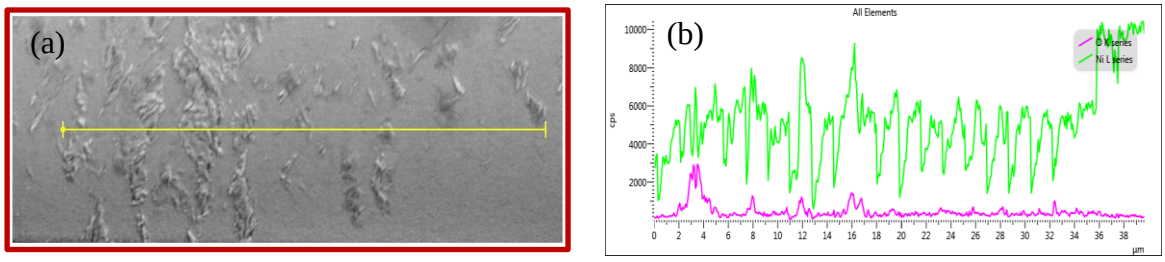

Figure 5.6: (a) SEM image of notch root of micro-resonator (η = 0.17 μm^{-1}) with σ_a = 413 MPa stress during the fatigue test; (b) Line profile shows the oxygen and nickel percentage variation along line passes over the local extrusions.

Figure 5.7 shows the SEM images of beam side wall, beam top surface, and the beam cross-section correspond to the specimen (η = 17%.μm^{-1}) tested at σ_a = 355 MPa (with a total decrease of 40% in f_0), after 1.54×10^7 cycles, for which the cracks joined at the top surface (a = 5.8 μm). This image corresponds to the microresonator presented in Figure 5.3(g-i) and the cross-sections were obtained by carefully rupturing the

remaining ligaments using a micromanipulator, which are highlighted in the SEM images (ductile fracture surface in Figure 5.7 (f)). Figure 5.7 (b, f) shows that two simultaneous cracks initiate and propagate toward the neutral axis. The bottom half of this specimen after the fatigue test was held by a 2-3 μm-wide ligament.

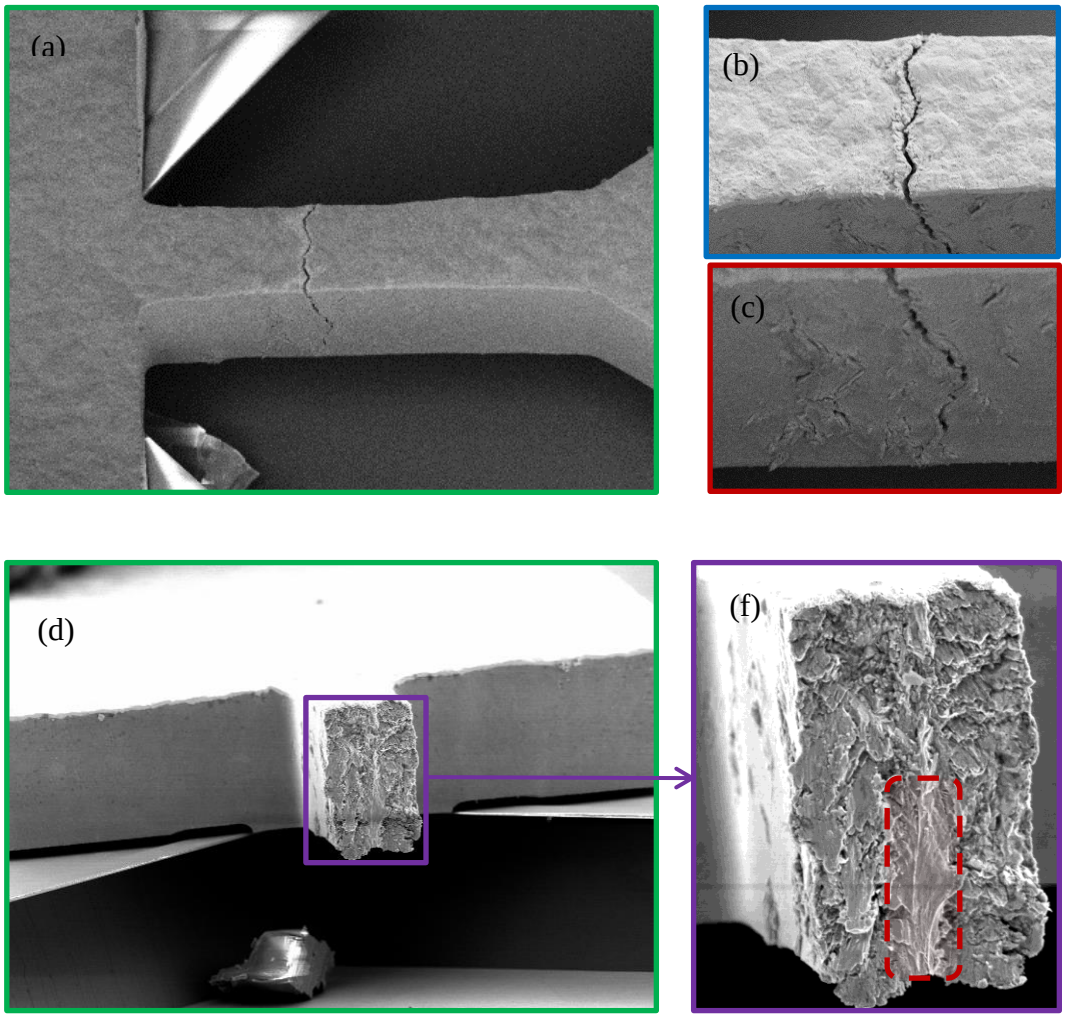

Figure 5.7: SEM images of the fracture surface's cross-section of fatigued specimens, tested at σ_a = 355 MPa.

Figure 5.8 and Figure 5.9 show EDS measurements were performed of the fracture surface's cross-section on three specimens (two were fatigued at 30°C, 50% RH and one at 80°C, 90% RH) and confirmed the presence of higher oxygen

concentration at the location of the extrusions (see oxygen maps in Figure 5.8 (d)). Figure 5.8 shows the elemental map, line map and point analyses for fatigue test performed at 30°C, 50% RH with σ_a = 310 MPa at notch, after 2.38×10^8 cycles which results in 6% decrease in resonance frequency. In a qualitative approach, Figure 5.8 (b, c) shows the elemental composition distribution along a 21 μm length line (line map) which is crossing the notch root of microbeam. As shown in Figure 5.8(c), nickel and oxygen elemental compositions on the location of extrusions suggest the nickel oxide formation. Following that, in a quantitative approach, Figure 5.8 (e-h) compare the elemental composition of two points on the area with higher extrusion concentration (spectrum 2, 4) and two points free of extrusion (spectrum 1,3) and illustrate higher oxygen percentage on the area with highly localized extrusion. This comparison evaluates the presence of highly localized oxygen on the location of propagated cracks. For example, Figure 5.8 (e) compares the detected CPS for oxygen and nickel elements at point 1 (far away from extrusion sites on microresonator base sidewall) and point 2 (at beam cross-section with highly localized extrusion). The corresponding wt% have been normalized by using predefined standards at EDS software and show that the oxygen/nickel ratio increase from 1% at point 1 to ~ 8% at point 2 which is interpreted as a result of oxide formation at crack tip and its extension with crack propagation during the fatigue test.

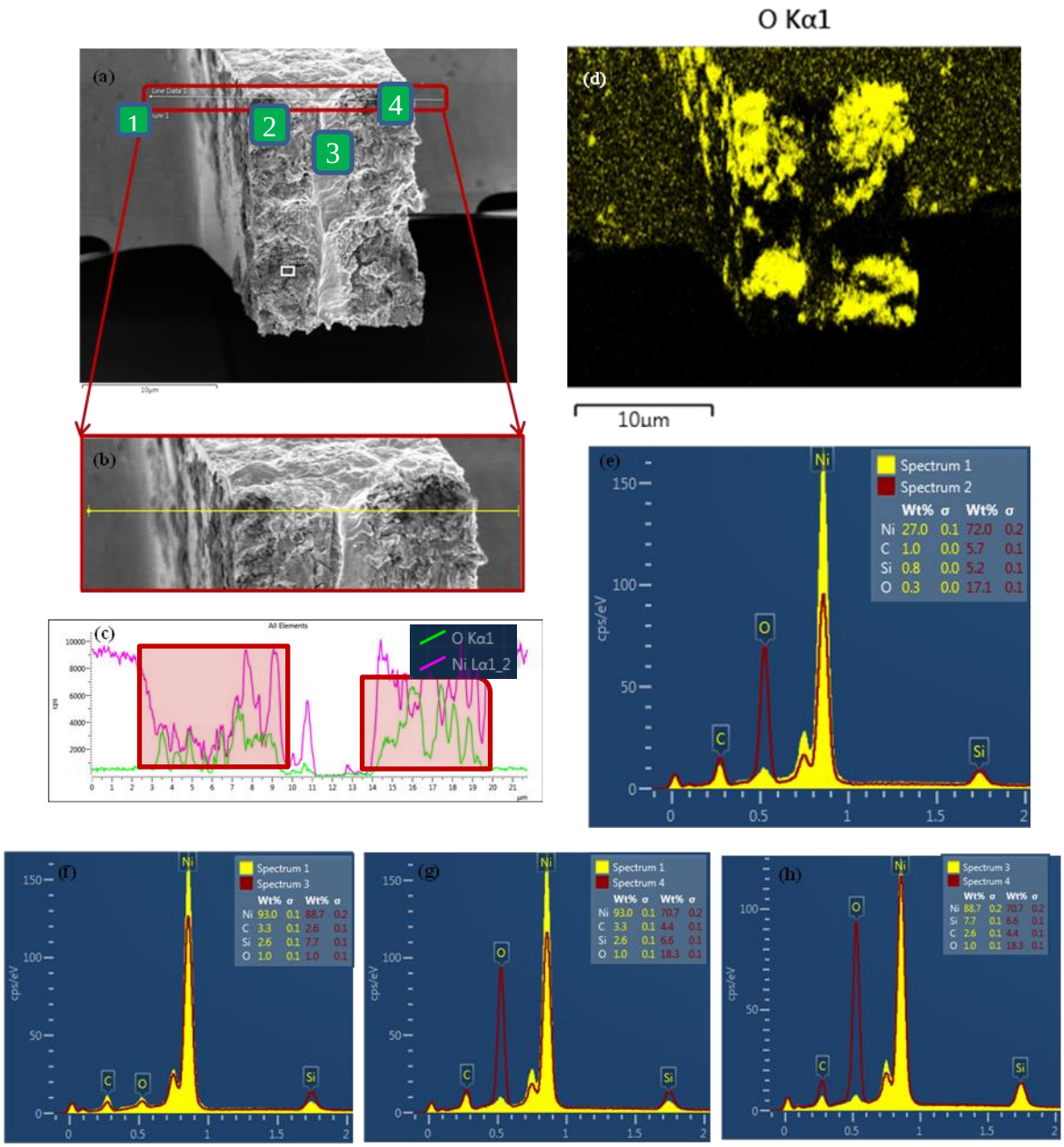

Figure 5.8: (a) SEM image of beam cross section fatigued at (30°C, 50% RH) environment with 312 MPa at notch, after 2.38×10^{8} cycles which results in 6% decrease in resonance frequency. (b, c) SEM image and corresponding line map, respectively; confirms the formation of localized oxides at extrusion and intrusion sites. (d) EDS oxygen map of the notch.(e-h) compare the elemental composition of two points on the area with high extrusion concentration (spectrum 2, 4) and two points free of extrusion (spectrum 1,3)

Figure 5.9 (a) shows EDS results of fracture surface, after breaking the remaining ligament at the end of the fatigue test, of the microbeam shown in Figure 5.7. The elemental maps of the beam cross section reveal much larger oxygen contents at the locations of crack flanks. Figure 5.9 (b) shows EDS results of fracture surface of fatigued specimen in harsh environment, revealing as well larger oxygen contents at the crack flank areas.

To summarize, the EDS results for the fracture surfaces hint to a strong environmental component for the fatigue crack growth process of the stage I, crystallographic cracks. The elemental maps also show large oxygen contents along the fatigue crack flanks (but not, importantly, along the surface of the remaining ligament in the center that was broken after the fatigue test), with local spectra within the fatigue fracture surface associated with up to 10-15wt% in oxygen. Stage I fatigue cracks are known to be associated with much slower growth rates in inert environments, due to mechanisms such as chemisorbed oxygen (or crack tip oxidation) that increases the slip irreversibility at the crack tip and prevents the rewelding of these small, crystallographic cracks [77]. As such, the ultraslow crack growth rates calculated for these microbeams in humid air environments (see section 5.5) should be even slower in vacuum environments.

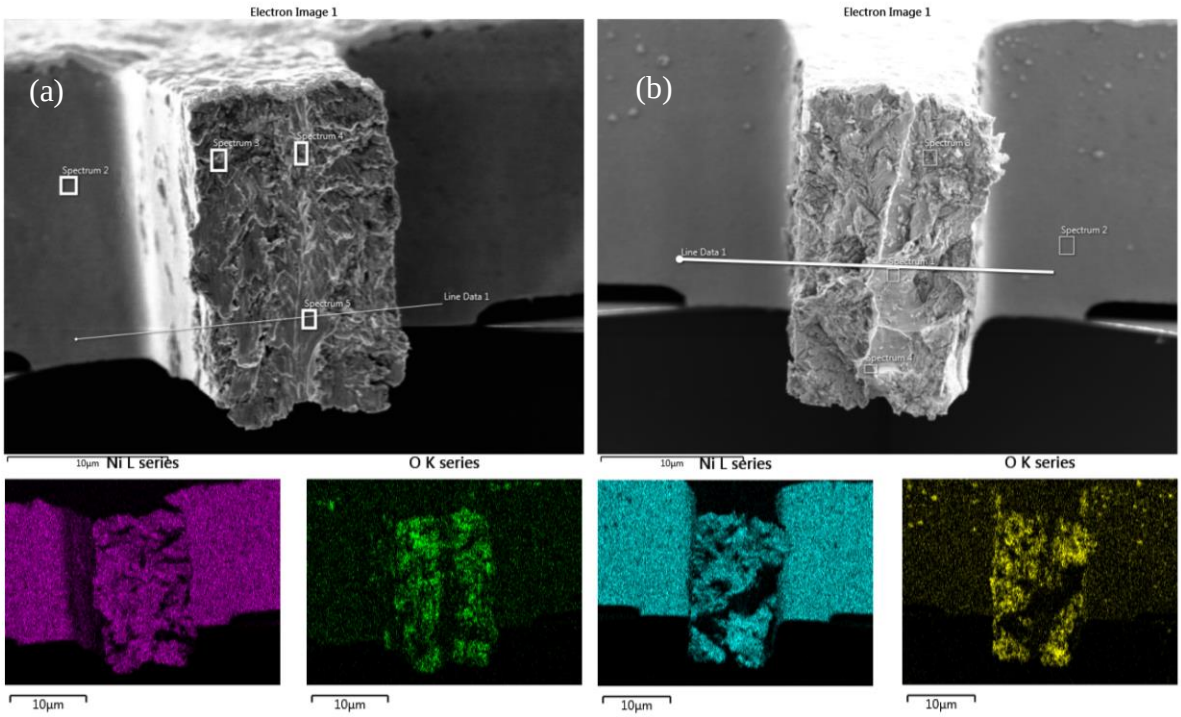

Figure 5.9: EDS results of fracture surface of specimen tested: (a) at 30°C, 50% RH (σ_a = 355 MPa, N_f = 1.54× 10^7 cycles, 40% decrease in f_0). (b) at 80°C, 90% RH (σ_a = 370 MPa, N_f = 1.8 × 10^7 cycles, 50% decrease in f_0).

5.3 S-N Curve under Extreme Stress Gradients: 17 vs 36%.µm^{-1}

Figure 5.10 (a) and (b) show the strong stress gradient effects that are observed in the σ_a - N_f and ε_{pa} - N_f curves, respectively. As a reminder, σ_a corresponds to the local stress value at the notch root, calculated at the beginning of a fatigue test. At σ_a ~ 450 MPa (ε_{pa} ~ 6×10^{-4}), the fatigue life N_f is 1000 times larger for η = 17%.µm^{-1} (N_f = 10^5 cycles) than for η = 36%.µm^{-1} (N_f = 10^8 cycles), highlighting significant differences. Figure 5.10 (a) also shows a stress-life fatigue curve under fully reversed loading

conditions and no stress gradients (unnotched specimens) that was predicted from the measured tension-tension uniaxial fatigue properties [78].

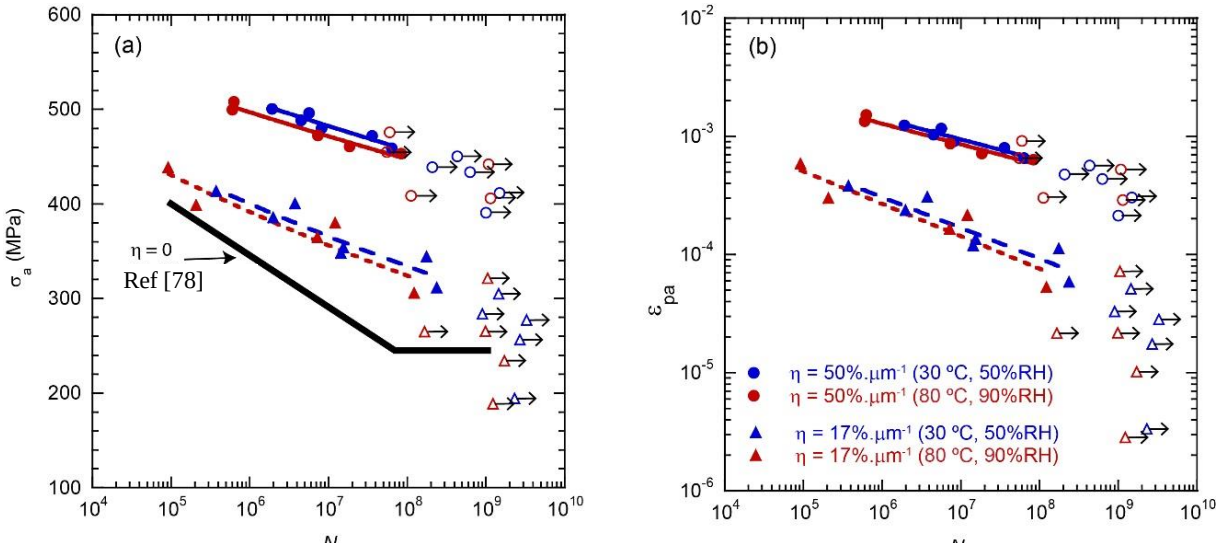

Figure 5.10: (a) $\sigma_a - N_f$ curves for all fatigue tests (at 30ºC, 50% RH and 80ºC, 90% RH, for both series of microresonators with 0.36 and 0.17 μm^{-1} stress gradient). (b) Corresponding $\varepsilon_{pa} - N_f$ curves.

The tensile properties for that electroplated Ni were similar to ours, with a 0.2% yield stress of 508 MPa and an ultimate tensile strength of 863 MPa, which warrants a proper comparison with our σ_a - N_f curves under extreme stress gradients. The fatigue limit is ~450 MPa (50% of tensile strength) for η = 36%.μm^{-1} and ~300 MPa (35% of tensile strength) for η = 17%.μm^{-1}, compared to a fatigue limit of 250 MPa (29% of tensile strength) for η = 0%.μm^{-1}. *Table 9* lists the Basquin and Coffin-Manson coefficients associated with the fatigue life curves shown in Figure 5.10. The Basquin coefficient, *b*, decreases from -0.023 (η = 36%.μm^{-1}) to -0.04 (η = 17%.μm^{-1}) and -0.07 (η = 0%.μm^{-1}). Typical *b* values for bulk metals range from -0.05 for hardened metals

to -0.12 for soft metals, with an average value of b = -0.085 [19]. Similarly, the Coffin-Manson coefficient, c, decreases from -0.18 (η = 36%.μm^{-1}) to -0.26 (η = 17%.μm^{-1}), while typical c values for bulk metals are -0.6 (ranging from -0.5 to -0.8) [19].

Table 9: Basquin and Coffin-Manson coefficients associated with the fatigue life curves shown in Figure 5.10.

η	σ'_f (MPa)		b (-)		ε'_f (-)		c (-)	
	30ºC, 50% RH	80ºC, 90% RH	30ºC, 50% RH	80ºC, 90% RH	30ºC, 50% RH	80ºC, 90% RH	30ºC, 50% RH	80ºC, 90% RH
17%.μm^{-1}	685	690	-0.039	-0.041	0.011	0.012	-0.259	-0.275
36%.μm^{-1}	705	680	-0.023	-0.023	0.016	0.014	-0.175	-0.175

5.4 Finite Element Analysis Results

A finite element model was employed to assess the effect of cracking on the resonance frequency of microresonator with η = 17%. μm^{-1}. For FEM model (see section 3.1.3), it has also been assumed that the two cracks on both sides of beam propagate toward the natural axis simultaneously. Also, for this resonator, 2.2-micron crack growth is considered to be the failure criterion, which corresponds to a 10% decrease in resonant frequency. Similar to what presented in section 4.4., the model predicts an average crack growth rate for that equivalent 2D crack, whereas the actual configuration most likely consist of nearby 3D crystallographic cracks that may not grow simultaneously. The previously developed 2D model with one crack (of length a) at the notch side for η = 36%. μm^{-1} (see section 4.4.) that accurately correlates the

decrease in resonance frequency to corresponding growth in crack length was modified by adding the second crack (of length a) on the other side of the beam for $\eta = 17\%.\mu m^{-1}$. The inset in Figure 5.11 (a) shows the geometry of the cracked beam for both $\eta = 17$ and $36\%.\mu m^{-1}$. A crack opening of 300 nm was chosen at the edge, mimicking the experimental observations. Figure 5.11 (a) shows the predicted crack size, a, as a function Δf_0 (total decrease in f_0), along with the experimental measurements. For $\eta = 17\%.\mu m^{-1}$, the crack size, a, was measured by averaging the length of the 2 measured cracks at the top surface. Overall, the experimental data match very well the predictions, with the majority of the measured a being at most ~1-2 μm larger than the predicted values. There are two possible explanations for the observed discrepancy. First, the model assumes a 2D crack, while the actual crack may not be perfectly uniform throughout the thickness. Figure 5.11 (b-d) show SEM images of the fracture surface's cross-section of 3 fatigued specimens, with the corresponding data point on Figure 5.11 (a). The cross-sections were obtained by carefully rupturing the remaining ligaments using a micromanipulator, which are highlighted in the SEM images (ductile fracture surface). Figure 5.11 (b) corresponds to the specimen showed on Figure 5.7, for which the cracks joined at the top surface (a = 5.8 μm). The bottom half of this specimen after the fatigue test was held by a 2-3 μm-wide ligament. Therefore, the average a value for that specimen should be ~4.3-4.8 μm instead of 5.8 μm, which is much closer to the predicted a ~ 4 μm. A similar argument can be made for the specimen shown in Figure 5.11 (c). On the other hand, Figure 5.11 (d) shows a very uniform crack along the specimen's thickness, while the measured crack size is still ~1μm larger than the predicted value. This small discrepancy may be accounted for by the bilinear stiffness

effect introduced with a crack that fully closes under compression. This effect was not taken into account in our model given that it is unclear whether or not the cracks fully closes under compression given the observed crack openings under no applied stress (see Figure 5.3 and Figure 5.4). Despite these approximations, we conclude that the model is capable of predicting crack size based on f_0 measurements, from which crack propagation rates can be obtained.

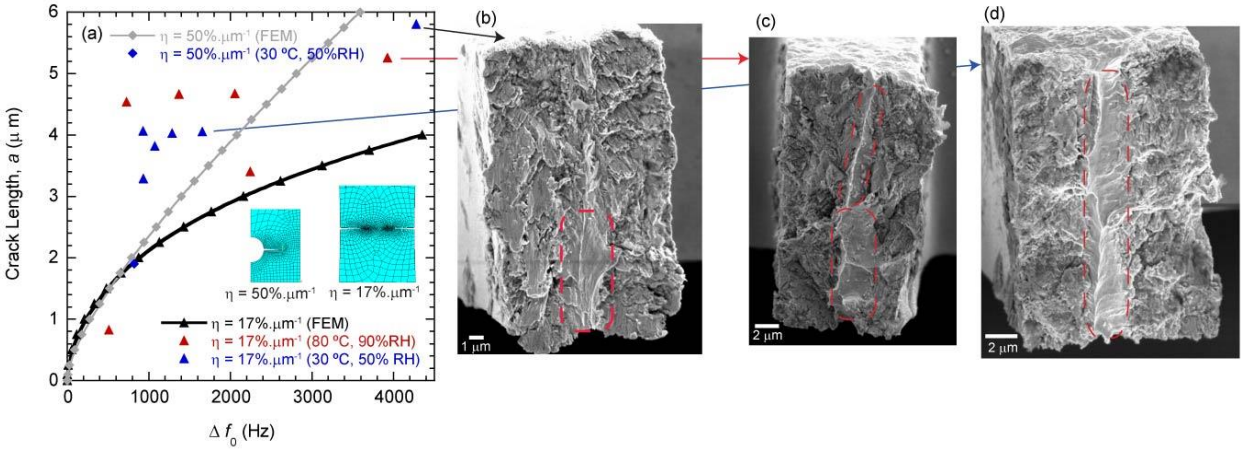

Figure 5.11: Predicted crack size, a, as a function Δf_0 (total decrease in f_0), along with the experimental measurements (inset shows geometry of the cracked beams for the FEM models); SEM images of the fracture surface's cross-section of 3 fatigued specimens, tested at (b) σ_a = 355 MPa, (c) σ_a = 370 MPa, and (d) σ_a = 310 MPa. For (b), see f_0 evolution in Figure 5.1 (a) and SEM image before fracturing the specimen in Figure 5.7 (a, b).

5.5 Crack Growth Rate Calculation and Results

The crack growth rates are evaluated based on the f_0 evolution plots , which are transformed into "a vs N" plots (with a crack size at the notch root) through a 2D FEM (presented in section 2.9) predicting a as a function of the measured decrease in f_0, Δf_0. The crack size a should be understood as an equivalent 2D crack size that leads to the

same decrease in f_0 as in the actual fatigued micro-beam in which several cracks across the thickness may nucleate separately in adjacent grains. Figure 5.12 (a) shows the plots of frequency development for three specimens, with η = 17%.μm^{-1}, presented in Figure 5.1 (a) transformed into "*a* vs *N*". Subsequently, these plots are transformed into crack growth rates, d*a*/d*N*, as a function of *a* (see Figure 5.12 (b)) using polynomial fits of successive segments of *a* vs *N* curves (from *a* = 0 to 0.5 μm, 0.5 to 1 μm, etc.) to compute the rates. Figure 5.12 (b) shows that the crack growth tendencies are a strong function of σ_a. For σ_a = 305 MPa (run out specimens), the rates are ultralow and decreasing with crack size. For σ_a = 355 and 400 MPa, the rates are larger (although still ultralow with respect to long cracks rates) and do not decrease with crack size. Instead, they are fairly constant over the first two micrometers, after which the rates increase with increasing *a*. This behavior is unlike that of long cracks and is interpreted as the consequence of having microstructurally small cracks under extreme stress gradients. For bulk metals, the microstructurally small crack growth rates are much larger (even larger than the long cracks' rates) [19], and tend to decrease with increasing crack size (see section 1.2). Here the ultralow rates are likely the consequence of the presence of extreme stress gradients.

The fact that these stress gradients play a significant role in the fatigue degradation of the microbeams is further illustrated by their strong effect on the crack growth rates. For η = 36%.μm^{-1}, we demonstrated that the crack growth rates tend to decrease with increasing *a*, for the entire range of σ_a (up to 500 MPa), see section 4.5, in contrast to the behavior observed for η = 17%.μm^{-1} (see comparison in Figure 5.12 (b)).

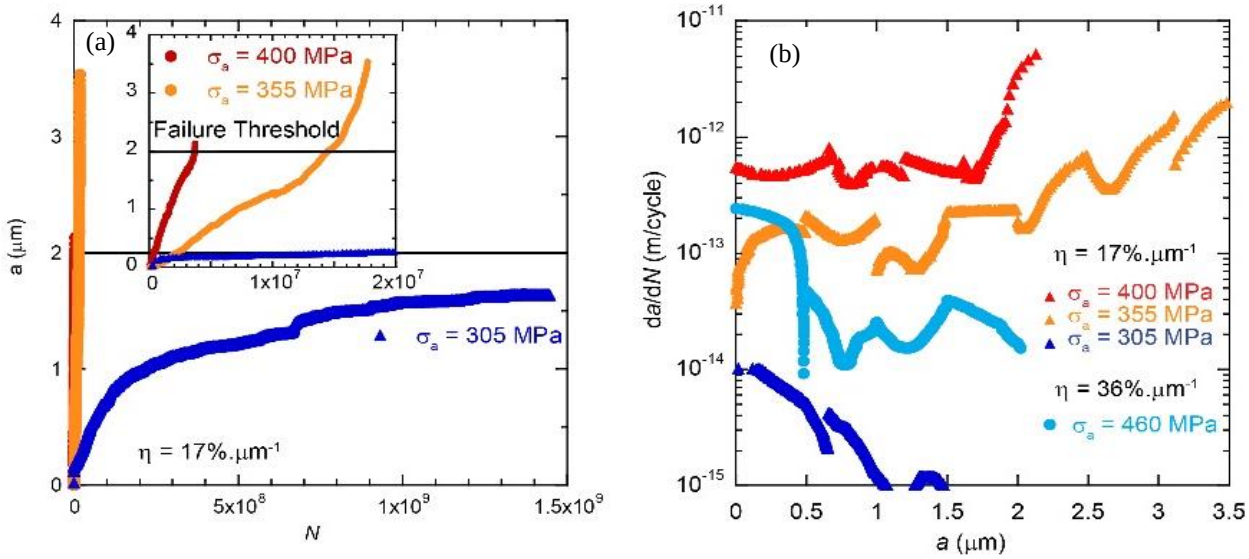

Figure 5.12: (a) Calculated crack size, *a*, as a function of cycles for three representative tests performed at 30ºC, 50% RH. (b) Corresponding crack propagation rate curves.

In addition, the initial rates, $(da/dN)_i$, calculated at $a = 0$ (from Figure 5.12 (b)), are also strongly influenced by the stress gradients, as illustrated in Figure 5.13 showing the rates for both $\eta = 17$ and $36\%.\mu m^{-1}$ (and both testing environments) as a function of σ_a (Figure 5.13 (a)) and ε_{pa} (Figure 5.13 (b)). For $\eta = 17\%.\mu m^{-1}$, the initial rates could be calculated down to $\sigma_a = 300$ MPa ($\varepsilon_{pa} = 5\times10^{-5}$) whereas no measurable rates could be obtained for $\sigma_a < 400$ MPa for $\eta = 36\%.\mu m^{-1}$. The trends in Figure 5.13 show that the initial rates are more than one order of magnitude larger for the lower η. Therefore, for $\sigma_a > 400$ MPa, the crack propagation rates of the notched microbeams ($\eta = 36\%.\mu m^{-1}$) are initially ultralow (from 10^{-13} to 10^{-11} $m.s^{-1}$) and decrease with increasing *a*, whereas for $\eta = 17\%.\mu m^{-1}$, the crack propagation rates are initially at least ten times faster and do not decrease with increasing *a*.

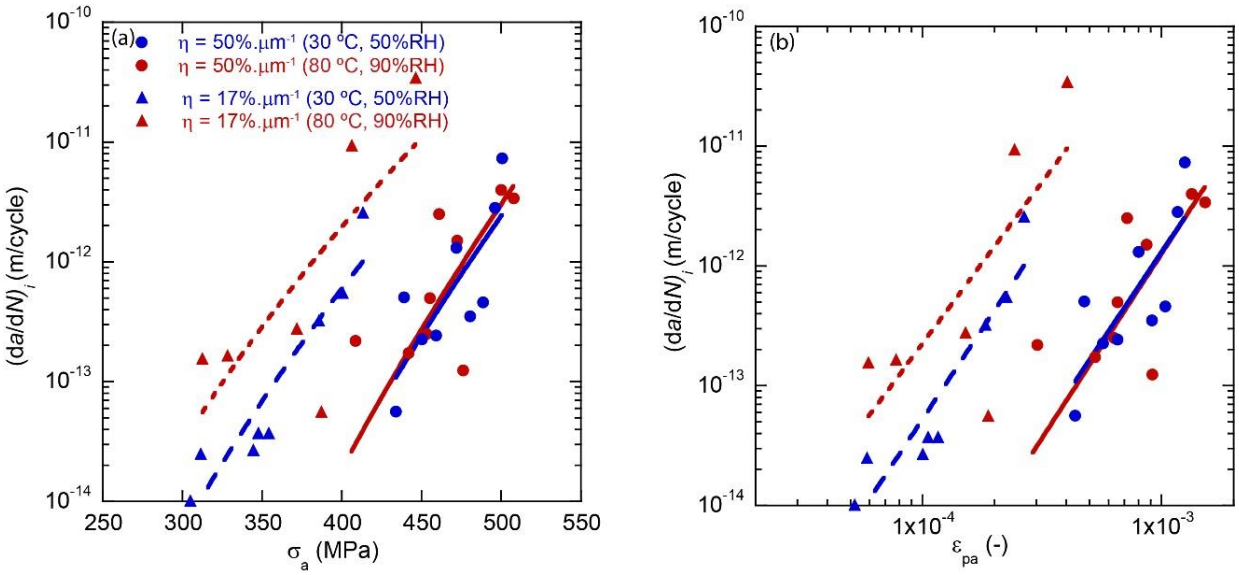

Figure 5.13: Initial crack propagation rates, $(da/dN)_i$ as a function of (a) σ_a, and (b) ε_{pa} . The legend is same for both figures.

5.6 Conclusions

This chapter unveiled the significant effects of extreme stress gradients on the fatigue response of metallic microbeams. Figure 5.10 (a) show that the endurance limit increases from 35 to 50% of the tensile strength for stress gradients increasing from 17 to 36%.μm^{-1}, compared to 30% in the absence of stress gradients. Similarly, the Basquin coefficient, *b*, varies from -0.039 to -0.023 for stress gradients increasing from 17 to 36%.μm^{-1}, compared to -0.07 in the absence of stress gradients. These strong effects, resulting in fatigue lives differing by orders of magnitude for a given σ_a, are mainly driven by the effects of stress gradients on the crack growth rates on microstructurally small cracks. Not only are the initial rates ten times faster for η = 17%.μm^{-1} compared to η = 36%.μm^{-1}, the discrepancy is even larger with increasing crack size from 0 to 2 μm. Accurate prediction of these microbeams' fatigue response will therefore require the development of physics-based models for microstructurally

small crack growth, which are still in their infancy even in the absence of stress gradients. In that regard, as future work, the fatigue microresonators are well suited to perform *in situ* SEM fatigue experiments in order to investigate the fatigue response in vacuum conditions and to further understand the effects of oxygen and water on fatigue crack formation and microstructurally small crack growth.

CHAPTER 6: SIGNIFICANCE OF THE WORK

In this study we developed a promising technique to quantify the extreme stress gradient effects on the fatigue behavior of LIGA Ni microbeams in different environments, specifically propagation of microstructurally small cracks. The presented research highlights the critical role of the stress gradient on the fatigue life of microbeams. It also highlights the need to account for these effects in order to accurately predict the fatigue degradation properties of advanced metallic micro-components under bending, such as in microelectromechanical systems or flexible electronics. Particularly, the results of this research call for the development of a microstructural fracture mechanics approach under such extreme stress gradients. This understanding provides useful guidelines for increasing the safety and reliability of MEMS devices, particularly those exposed to the environment during operation. The significant contributions are listed below:

1) This research provides a novel technique for MEMS-relevant small-scale fatigue testing conditions based on kHz-frequency microresonators. The technique relies on the measured evolution of the resonance frequency throughout the fatigue test and finite element models to calculate a fatigue life corresponding to the nucleation and growth of a ~2-micrometer-long crack. In addition, the growth rates of these microstructurally small cracks were estimated also based on the measured resonance frequency evolution. This methodology was used to investigate the effects of extreme stress gradients (normalized stress gradients of 17% and 36%μm over the first 2 μm at the notch

root) in small-scale, fully-reversed bending fatigue behavior of 20-μm-thick electroplated Ni notched microbeams actuated at resonance (~8 kHz).

2) Compared to our previous study, larger driving forces (stress amplitudes up to 510 MPa (60% of the ultimate tensile strength), corresponding to plastic strain amplitudes up to ~0.1%) were applied, leading to the propagation of microstructurally small cracks ahead of the notch. This study revealed the critical role of extreme stress gradients, often encountered in micro-components, on their fatigue behavior. The notched microbeams, characterized by a normalized stress gradient of -36%/μm, required from 10^6 to 10^8 cycles (under fully reversed loading) to grow a 2-μm-long microstructurally small crack through the entire beam thickness (20 μm), for stress amplitudes ranging from 440 to 500 MPa (50 to 60% of the ultimate tensile strength). For η = 17%.μm^{-1}, 10^5 to 5×10^8 cycles are required to grow two simultaneous 2.2-μm microstructurally small cracks (one on each side of the microbeam) with stress amplitudes ranging from ~300 to 450 MPa (35 to 50% of the ultimate tensile strength). Therefore, the stress gradient plays a significant role on fatigue behavior of nickel microbeams and the endurance limit increased from 35 to 50% of the tensile strength for stress gradients increasing from 17% to 36%.μm^{-1}, compared to 30% in the absence of stress gradients. For both microresonators, little differences in the fatigue response between the two investigated environments (30°C, 50% RH vs 80°C, 90% RH) have been observed with slightly shorter fatigue lives in the harsher environment. Similarly the corresponding Basquin and Coffin-Manson fits for the stress and

strain-life curves, respectively, exhibit much lower (in absolute value) fatigue exponents than typical values for bulk metals. The Basquin coefficient, *b*, varies from -0.039 to -0.023 for stress gradients increasing from 0.17 to 0.36.μm^{-1}, compared to -0.07 in the absence of stress gradients.

3) This singular behavior is explained by the ultraslow and decelerating crack growth rates, calculated based on the measured resonance frequency evolution during the fatigue tests, which appear to characterize the growth of microstructurally small cracks under extreme stress gradients. This ultraslow growth is unlike that of microstructurally small cracks in the absence of extreme stress gradients, and is responsible for the shallow stress and strain-life curves and high endurance limits. For η = 17%.μm^{-1}, $(da/dN)_i$, ranges from ~10^{-14} m/cycle to almost ~10^{-11} m/cycle for σ_a increasing from 300 to 450 MPa. The initial rates are more than one order of magnitude lower for η = 36%.μm^{-1} compared to η = 17%.μm^{-1}. Therefore, the extreme stress gradients probed in this study have a major effect on the initial crack propagation rates, that are for example ~10 times larger for η = 17%.μm^{-1} compared to η = 36%.μm^{-1} for σ_a between 400 and 450 MPa. Not only are the initial rates ten times faster for η = 17%.μm^{-1} compared to η = 36%.μm^{-1}, the discrepancy is even larger with increasing crack size from 0 to 2 μm. For η = 36%.μm^{-1}, the initial rates decrease with increasing *a*, whereas for η = 17%.μm^{-1}, the crack propagation rates do not decrease with increasing *a*.

4) SEM images of microresonator with 17%.μm^{-1} presented in chapter 5 suggest little differences in the fatigue response between the two investigated

environments (30°C, 50% RH vs 80°C, 90% RH), with slightly shorter fatigue lives in the harsher environment. EDS results from sidewalls and fracture surface of fatigued microbeams show similar footprints of the two environments. The elemental maps of the beam sidewalls highlights much larger oxygen contents associated with extrusions rather than the adjacent areas subjected to the same σ_a where no extrusions were formed. The elemental maps of fracture surface also show large oxygen contents along the fatigue crack flanks (but not, importantly, along the surface of the remaining ligament in the center that was broken after the fatigue test), with local spectra within the fatigue fracture surface associated with up to 10-15wt% in oxygen. This highlights the strong environmental component for the fatigue crack growth process of the stage I, crystallographic cracks. Stage I fatigue cracks are known to be associated with much slower growth rates in inert environments, due to mechanisms such as chemisorbed oxygen (or crack tip oxidation) that increases the slip irreversibility at the crack tip and prevents the rewelding of these small, crystallographic cracks. As such, the ultraslow crack growth rates calculated for these microbeams in humid air environments (see section 5.5) should be even slower in vacuum environments (which is recommended as a future direction of investigation).

CHAPTER 7: FUTURE WORK

The following recommendations for future work are made:

Our previous research indicated that the extrusions are associated with highly localized thick oxides (~1μm) after several billions of cycles. In addition, the growth of stage I fatigue cracks is known to be affected by the environment [41]. In that regard, the fatigue microresonators are well suited to perform *in situ* SEM fatigue experiments in order to investigate the fatigue response in vacuum conditions and to further understand the effects of oxygen and water on fatigue crack formation and microstructurally small crack growth.

A more sophisticated 3D crack propagation model (instead of currently developed 2D model) needs to be developed to help us to accurately correlate the frequency decrease during the fatigue test to its corresponding crack propagation, and consequently to more precisely calculate the crack growth rates for microstructurally small cracks. In that regard, SEM images of sequentially interrupted *in situ* SEM fatigue experiments could provide important geometric information of 3D cracks formation and their subsequent link up to form 2D cracks during the fatigue test. For example, based on SEM image observation, we could measure the crack opening at sidewall and associated crack length at top surface of the microbeam and implement them in the geometry of the propagating crack model.

Finally, it is worth mentioning that advanced crystal-plasticity-based models to predict microstructurally small cracks have been developed recently in the absence of extreme stress gradients [37]. Ultimately, such models could be adapted to the case of

microbeams with extreme stress gradients and integrated with the present technique to further investigate the microstructurally small crack growth regime in small scale fatigue.

REFERENCES

1. McEvily, A.J., *On the Frost-Dugdale plot for non-propagating cracks.* Fatigue & Fracture of Engineering Materials & Structures, 2011. **34**(12): p. 999-1002.
2. Frost, N.E. and D.S. Dugdale, *FATIGUE TESTS ON NOTCHED MILD STEEL PLATES WITH MEASUREMENTS OF FATIGUE CRACKS.* Journal of the Mechanics and Physics of Solids, 1957. **5**(3): p. 182-192.
3. Yang, Y., et al., *Nanoscale and submicron fatigue crack growth in nickel microbeams.* Acta Materialia, 2007. **55**(13): p. 4305-4315.
4. Boyce, B.L., J.R. Michael, and P.G. Kotula, *Fatigue of metallic microdevices and the role of fatigue-induced surface oxides.* Acta Materialia, 2004. **52**(6): p. 1609-1619.
5. Lukas, P. and M. Klesnil, *FATIGUE LIMIT OF NOTCHED BODIES.* Materials Science and Engineering, 1978. **34**(1): p. 61-66.
6. Hanlon, T., Y.N. Kwon, and S. Suresh, *Grain size effects on the fatigue response of nanocrystalline metals.* Scripta Materialia, 2003. **49**(7): p. 675-680.
7. Son, D., et al., *Evaluation of fatigue strength of LIGA nickel film by microtensile tests.* Scripta Materialia, 2004. **50**(10): p. 1265-1269.
8. Miller, K.J., *THE TWO THRESHOLDS OF FATIGUE BEHAVIOUR.* Fatigue & Fracture of Engineering Materials & Structures, 1993. **16**(9): p. 931-939.
9. Hanlon, T., E.D. Tabachnikova, and S. Suresh, *Fatigue behavior of nanocrystalline metals and alloys.* International Journal of Fatigue, 2005. **27**(10-12): p. 1147-1158.
10. Suresh, S., *Fatigue of materials*. 2nd ed. 1998, Cambridge ; New York: Cambridge University Press. xxi, 679 p.
11. Alsem, D.H., et al., *Fatigue failure in thin-film polycrystalline silicon is due to subcritical cracking within the oxide layer.* Applied Physics Letters, 2005. **86**(4).
12. Bao, C., L.X. Cai, and C. Dan, *Estimation of fatigue crack growth behavior for small-sized C-shaped inside edge-notched tension (CIET) specimen using compliance technique.* International Journal of Fatigue, 2015. **81**: p. 202-212.
13. Boukharouba, T., et al., *THE USE OF NOTCH STRESS INTENSITY FACTOR AS A FATIGUE-CRACK INITIATION PARAMETER.* Engineering Fracture Mechanics, 1995. **52**(3): p. 503-512.
14. Elhaddad, M.H., T.H. Topper, and K.N. Smith, *PREDICTION OF NON PROPAGATING CRACKS.* Engineering Fracture Mechanics, 1979. **11**(3): p. 573-584.
15. Pluvinage, G., *Fatigue and fracture emanating from notch; the use of the notch stress intensity factor.* Nuclear Engineering and Design, 1998. **185**(2-3): p. 173-184.
16. Tanaka, K. and Y. Nakai, *PROPAGATION AND NON-PROPAGATION OF SHORT FATIGUE CRACKS AT A SHARP NOTCH.* Fatigue of Engineering Materials and Structures, 1983. **6**(4): p. 315-327.
17. Troshchenko, V.T. and L.A. Khamaza, *FATIGUE LIMITS OF STEELS AND STRESS GRADIENT.* Strength of Materials, 2011. **43**(4): p. 417-425.
18. Hammouda, M.M., R.A. Smith, and K.J. Miller, *ELASTIC-PLASTIC FRACTURE-MECHANICS FOR INITIATION AND PROPAGATION OF NOTCH FATIGUE CRACKS.* Fatigue of Engineering Materials and Structures, 1979. **2**(2): p. 139-154.
19. Suresh, S., *Fatigue of materials*. 2001: Cambridge University Press.
20. Miller, K.J., *THE 2 THRESHOLDS OF FATIGUE BEHAVIOR.* Fatigue & Fracture of Engineering Materials & Structures, 1993. **16**(9): p. 931-939.
21. Ma, X.F. and H.J. Shi, *On the fatigue small crack behaviors of directionally solidified superalloy DZ4 by in situ SEM observations.* International Journal of Fatigue, 2012. **35**(1): p. 91-98.

22. King, A., et al., *Three-dimensional in situ observations of short fatigue crack growth in magnesium.* Acta Materialia, 2011. **59**(17): p. 6761-6771.
23. Marrow, T.J., et al., *A quantitative three-dimensional in situ study of a short fatigue crack in a magnesium alloy.* International Journal of Fatigue, 2014. **66**: p. 183-193.
24. Petit, J. and C. Sarrazin-Baudoux, *Some critical aspects of low rate fatigue crack propagation in metallic materials.* International Journal of Fatigue, 2010. **32**(6): p. 962-970.
25. Rios, E.R.D., Z. Tang, and K.J. Miller, *SHORT CRACK FATIGUE BEHAVIOR IN A MEDIUM CARBON-STEEL.* Fatigue of Engineering Materials and Structures, 1984. **7**(2): p. 97-108.
26. Rodopoulos, C.A. and E.R. de los Rios, *Theoretical analysis on the behaviour of short fatigue cracks.* International Journal of Fatigue, 2002. **24**(7): p. 719-724.
27. Geathers, J., et al., *Investigating environmental effects on small fatigue crack growth in Ti-6242S using combined ultrasonic fatigue and scanning electron microscopy.* International Journal of Fatigue, 2015. **70**: p. 154-162.
28. Yates, J.R. and M.W. Brown, *PREDICTION OF THE LENGTH OF NON-PROPAGATING FATIGUE CRACKS.* Fatigue & Fracture of Engineering Materials & Structures, 1987. **10**(3): p. 187-201.
29. Newman, J.C., *A REVIEW OF MODELING SMALL-CRACK BEHAVIOR AND FATIGUE-LIFE PREDICTIONS FOR ALUMINUM-ALLOYS.* Fatigue & Fracture of Engineering Materials & Structures, 1994. **17**(4): p. 429-439.
30. Tanaka, K. and Y. Nakai, *MECHANICS OF GROWTH THRESHOLD OF SMALL FATIGUE CRACKS.* Journal of Metals, 1983. **35**(8): p. A15-A15.
31. Tanaka, K., Y. Nakai, and M. Yamashita, *FATIGUE GROWTH THRESHOLD OF SMALL CRACKS.* International Journal of Fracture, 1981. **17**(5): p. 519-533.
32. Seitl, S. and P. Hutar, *Fatigue-crack propagation near a threshold region in the framework of two-parameter fracture mechanics.* Materiali in Tehnologije, 2007. **41**(3): p. 135-138.
33. Hussain, K., E.R. Delosrios, and A. Navarro, *A 2-STAGE MICROMECHANICS MODEL FOR SHORT FATIGUE CRACKS.* Engineering Fracture Mechanics, 1993. **44**(3): p. 425-436.
34. Newman, J.C., B.S. Annigeri, and Asme, *FATIGUE-LIFE PREDICTION METHOD BASED ON SMALL-CRACK THEORY IN AN ENGINE MATERIAL*. Proceedings of the Asme Turbo Expo 2011, Vol 6, Pts a and B. 2012, New York: Amer Soc Mechanical Engineers. 103-112.
35. Castelluccio, G.M. and D.L. McDowell, *A mesoscale approach for growth of 3D microstructurally small fatigue cracks in polycrystals.* International Journal of Damage Mechanics, 2014. **23**(6): p. 791-818.
36. Castelluccio, G.M. and D.L. McDowell, *Microstructure and mesh sensitivities of mesoscale surrogate driving force measures for transgranular fatigue cracks in polycrystals.* Materials Science and Engineering a-Structural Materials Properties Microstructure and Processing, 2015. **639**: p. 626-639.
37. Castelluccio, G.M., W.D. Musinski, and D.L. McDowell, *Recent developments in assessing microstructure-sensitive early stage fatigue of polycrystals.* Current Opinion in Solid State & Materials Science, 2014. **18**(4): p. 180-187.
38. Buchheit, T.E., et al., *Microstructural and mechanical properties investigation of electrode posited and annealed LIGA nickel structures.* Metallurgical and Materials Transactions a-Physical Metallurgy and Materials Science, 2002. **33**(3): p. 539-554.
39. Yang, Y., et al., *Fatigue of LIGA Ni micro-electro-mechanical system thin films.* Metallurgical and Materials Transactions a-Physical Metallurgy and Materials Science, 2007. **38A**(13): p. 2340-2348.
40. Dubey, S., A.B.O. Soboyejo, and W.O. Soboyejo, *An investigation of the effects of stress ratio and crack closure on the micromechanisms of fatigue crack growth in Ti-6Al-4V.* Acta Materialia, 1997. **45**(7): p. 2777-2787.

41. Baumert, E.K., et al., *Fatigue-induced thick oxide formation and its role on fatigue crack initiation in Ni thin films at low temperatures.* Acta Materialia, 2014. **67**: p. 156-167.
42. Baumert, E.k., *Influence of the Environment on the Fatigue Properties of Alumina Ultra-Thin Coatings and Silicon and Nickel Thin Films*, in *George w. Woodruff School of Mechanical Engineering*. 2013, Georgia Institute of technology.
43. Baumert, E.K. and O.N. Pierron, *Very high cycle fatigue crack initiation in electroplated Ni films under extreme stress gradients.* Scripta Materialia, 2012. **67**(1): p. 45-48.
44. Baumert, E.K. and O.N. Pierron, *Fatigue Degradation Properties of LIGA Ni Films Using Kilohertz Microresonators.* Microelectromechanical Systems, Journal of, 2013. **22**(1): p. 16-25.
45. Baumert, E.K., et al., *Fatigue-induced thick oxide formation and its role on fatigue crack initiation in Ni thin films at low temperatures.* Acta Materialia, 2014. **67**(0): p. 156-167.
46. Burger, S., et al., *A novel high-throughput fatigue testing method for metallic thin films.* Science and Technology of Advanced Materials, 2011. **12**(5): p. 7.
47. Kiener, D., et al., *Cyclic response of copper single crystal micro-beams.* Scripta Materialia, 2010. **63**(5): p. 500-503.
48. Kirchlechner, C., et al., *On the reversibility of dislocation slip during small scale low cycle fatigue.* Acta Materialia, 2015. **94**: p. 69-77.
49. Read, D.T., *Tension-tension fatigue of copper thin films.* International Journal of Fatigue, 1998. **20**(3): p. 203-209.
50. Schwaiger, R., G. Dehm, and O. Kraft, *Cyclic deformation of polycrystalline Cu film.* Philosophical Magazine, 2003. **83**(6): p. 693-710.
51. Schwaiger, R. and O. Kraft, *Size effects in the fatigue behavior of thin Ag films.* Acta Materialia, 2003. **51**(1): p. 195-206.
52. Straub, T., et al., *A method for probing the effects of conformal nanoscale coatings on fatigue crack initiation in electroplated Ni films.* Thin Solid Films, 2012. **526**: p. 176-182.
53. Straub, T., et al., *Small-Scale Multiaxial Setup for Damage Detection Into the Very High Cycle Fatigue Regime.* Experimental Mechanics, 2015. **55**(7): p. 1285-1299.
54. Trinks, C. and C.A. Volkert, *Transition from dislocation glide to creep controlled damage in fatigued thin Cu films.* Journal of Applied Physics, 2013. **114**(9): p. 8.
55. Wimmer, A., et al., *Cyclic bending experiments on free-standing Cu micron lines observed by electron backscatter diffraction.* Acta Materialia, 2015. **83**: p. 460-469.
56. Wimmer, A., et al., *Damage evolution during cyclic tension-tension loading of micron-sized Cu lines.* Acta Materialia, 2014. **67**: p. 297-307.
57. Zhang, G.P., et al., *Length-scale-controlled fatigue mechanisms in thin copper films.* Acta Materialia, 2006. **54**(11): p. 3127-3139.
58. Meirom, R.A., et al., *Fatigue-induced grain coarsening in nanocrystalline platinum films.* Acta Materialia, 2011. **59**(3): p. 1141-1149.
59. Hosseinian, E. and O.N. Pierron, *Quantitative in situ TEM tensile fatigue testing on nanocrystalline metallic ultrathin films.* Nanoscale, 2013. **5**(24): p. 12532.
60. Eberl, C., et al., *Damage analysis in Al thin films fatigued at ultrahigh frequencies.* Journal of Applied Physics, 2006. **99**(11): p. 113501.
61. Lin, M.T., C.J. Tong, and K.S. Shiu, *Novel Microtensile Method for Monotonic and Cyclic Testing of Freestanding Copper Thin Films.* Experimental Mechanics, 2010. **50**(1): p. 55-64.
62. Budnitzki, M. and O.N. Pierron, *The influence of nanoscale atomic-layer-deposited alumina coating on the fatigue behavior of polycrystalline silicon thin films.* Applied Physics Letters, 2009. **94**(14).
63. Cowen, A., et al., *MetalMUMPs Design Handbook*. 2002.

64. Baumert, E.K. and O.N. Pierron, *Fatigue Degradation Properties of LIGA Ni Films Using Kilohertz Microresonators.* Journal of Microelectromechanical Systems, 2013. **22**(1): p. 16-25.
65. He, S.Y., et al., *Characterization of Young's modulus and residual stress gradient of MetalMUMPs electroplated nickel film.* Sensors and Actuators a-Physical, 2009. **154**(1): p. 149-156.
66. Pierron, O.N., C.C. Abnet, and C.L. Muhlstein, *Methodology for low- and high-cycle fatigue characterization with kHz-frequency resonators.* Sensors and Actuators a-Physical, 2006. **128**(1): p. 140-150.
67. Burns, D.J. and H.F. Helbig, *A system for automatic electrical and optical characterization of microelectromechanical devices.* Journal of Microelectromechanical Systems 1999. **8**(4): p. 473-82.
68. Theillet, P.O. and O.N. Pierron, *Low-cycle Fatigue Testing of Silicon Resonators.* Reliability, Packaging, Testing, and Characterization of Mems/Moems and Nanodevices Viii, 2009. **7206**.
69. Ikehara, T. and T. Tsuchiya, *High-cycle fatigue of micromachined single-crystal silicon measured using high-resolution patterned specimens.* Journal of Micromechanics and Microengineering, 2008. **18**(7): p. 7.
70. Baumert, E.K. and O.N. Pierron, *Interfacial Cyclic Fatigue of Atomic-Layer-Deposited Alumina Coatings on Silicon Thin Films.* Acs Applied Materials & Interfaces, 2013. **5**(13): p. 6216-6224.
71. Baumert, E.K. and O.N. Pierron, *Fatigue properties of atomic-layer-deposited alumina ultra-barriers and their implications for the reliability of flexible organic electronics.* Applied Physics Letters, 2012. **101**(25).
72. Cho, H.S., et al., *Measured mechanical properties of LIGA Ni structures.* Sensors and Actuators a-Physical, 2003. **103**(1-2): p. 59-63.
73. Son, D., et al., *Tensile properties and fatigue crack growth in LIGA nickel MEMS structures.* Materials Science And Engineering A-Structural Materials Properties Microstructure And Processing, 2005. **406**(1-2): p. 274-278.
74. Yang, Y., et al., *Mechanisms of fatigue in LIGA ni MEMS thin films.* Materials Science and Engineering a-Structural Materials Properties Microstructure and Processing, 2007. **444**(1-2): p. 39-50.
75. Sadeghi-Tohidi, F. and O.N. Pierron, *Extreme stress gradient effects on microstructural fatigue crack propagation rates in Ni microbeams.* Applied Physics Letters, 2015. **106**(20).
76. Pineau, A., et al., *Failure of metals II: Fatigue.* Acta Materialia.
77. Wang, R., et al., *FATIGUE OF COPPER SINGLE-CRYSTALS IN VACUUM AND IN AIR .1. PERSISTENT SLIP BANDS AND DISLOCATION MICROSTRUCTURES.* Materials Science and Engineering, 1984. **65**(2): p. 219-233.
78. Aktaa, J., et al., *High cycle fatigue and fracture behavior of LIGA Nickel.* Scripta Materialia, 2005. **52**(12): p. 1217-1221.